

CHARACTERIZATION OF PORTLAND CEMENT COMPOUNDS WITH
HYPERSPETRAL IMAGING

A THESIS SUBMITTED TO
THE GRADUATE SCHOOL OF NATURAL AND APPLIED SCIENCES
OF
MIDDLE EAST TECHNICAL UNIVERSITY

BY

SAHRA SHAKOURI

IN PARTIAL FULFILLMENT OF THE REQUIREMENTS
FOR
THE DEGREE OF DOCTOR OF PHILOSOPHY
IN
CIVIL ENGINEERING

NOVEMBER 2023

Approval of the thesis:

**CHARACTERIZATION OF PORTLAND CEMENT COMPOUNDS WITH
HYPERSPETRAL IMAGING**

submitted by **SAHRA SHAKOURI** in partial fulfillment of the requirements for the degree of **Doctor of Philosophy in Civil Engineering, Middle East Technical University** by,

Prof. Dr. Halil Kalıpçılar
Dean, Graduate School of **Natural and Applied Sciences**

Prof. Dr. Erdem Canbay
Head of the Department, **Civil Engineering**

Prof. Dr. İsmail Özgür Yaman
Supervisor, **Civil Engineering, METU**

Dr. Burhan Aleessa Alam
Co-Supervisor, **Civil Engineering, Hacettepe University**

Examining Committee Members:

Prof. Dr. Mustafa Şahmaran
Civil Engineering, Hacettepe University

Prof. Dr. İsmail Özgür Yaman
Civil Engineering, METU

Assoc. Prof. Dr. Hande Işık Öztürk
Civil Engineering, METU

Assoc. Prof. Dr. Çağla Akgül
Civil Engineering, METU

Asst. Prof. Dr. Emin Şengün
Civil Engineering, Ankara Yıldırım Beyazıt University

Date: 22.11.2023

I hereby declare that all information in this document has been obtained and presented in accordance with academic rules and ethical conduct. I also declare that, as required by these rules and conduct, I have fully cited and referenced all material and results that are not original to this work.

Name, Last name: Sahra Shakouri

Signature :

ABSTRACT

CHARACTERIZATION OF PORTLAND CEMENT COMPOUNDS WITH HYPERSPECTRAL IMAGING

Shakouri, Sahra
Doctor of Philosophy, Civil Engineering
Supervisor : Prof. Dr. İsmail Özgür Yaman
Co-Supervisor: Dr. Burhan Aleessa Alam

November 2023, 157 pages

Developing new and reliable methods for materials characterization is a progressing field of science and engineering. Hyperspectral imaging system is noted as one of the modern and proceeding techniques that can be employed in numerous subjects from remote sensing of earth and medical diagnoses to analyzing nanomaterials. This method is based on generating a spectral map for each spatial pixel of an image taken in any scale. Advantages like accuracy, rapidity, cost efficiency are some of the features that put this method one step ahead of the other possible options. All those advantages make hyperspectral imaging very suitable for cement analysis.

As one of the most widely utilized building materials, Portland cement has a complex structure with distinct compounds. Each of its compounds has a unique set of reaction kinetics during the hydration process. Investigating each reaction requires a series of specialized and complicated tests, which makes finding more convenient ways of observing these details highly demanded.

This is one of the first studies on the use of hyperspectral imaging in detecting cement compounds. The research utilizes reflectance hyperspectral spectroscopy in

the visible and near-infrared spectral range (400 to 1000 nm) to evaluate the characteristics of cement compounds. Each compound is produced in the laboratory with high purity, and their physical, chemical, and mechanical properties are thoroughly examined alongside their hyperspectral signatures.

After synthesizing these compounds, hyperspectral data are collected, forming the foundation for classifying randomly chosen cement clinkers. The accuracy of this classification was evaluated using the Deep Learning Toolbox in Matlab, specifically employing a Kernel Logistic Regression model. Notably, this model achieves an accuracy of 98.25% in classifying different types of cement through hyperspectral imaging.

Keywords: Cement Synthesis, Hyperspectral Imaging Analysis, Hyperspectral Signature, Material Characterization

ÖZ

HİPERSPEKTRAL GÖRÜNTÜLEME İLE PORTLAND ÇİMENTO BİLEŞİKLERİNİN KARAKTERİZASYONU

Shakouri, Sahra
Doktora, İnşaat Mühendisliği
Tez Yöneticisi: Prof. Dr. İsmail Özgür Yaman
Ortak Tez Yöneticisi: Dr. Burhan Aleessa Alam

Kasım 2023, 157 sayfa

Malzeme karakterizasyonu için yeni ve güvenilir yöntemler geliştirmek, bilim ve mühendisliğin ilerleyen bir alanıdır. Hiperspektral görüntüleme sistemi, dünyanın uzaktan algılanmasından tıbbi teşhislere ve nanomalzemelerin analizine kadar birçok konuda kullanılabilen modern ve ilerici tekniklerden biri olarak dikkat çekmektedir. Bu yöntem, herhangi bir ölçekte alınan bir görüntünün her bir uzaysal pikseli için spektral bir harita oluşturmaya dayanmaktadır. Doğruluk, hızlilik, maliyet verimliliği gibi avantajlar bu yöntemi diğer olası seçeneklerden bir adım öne çıkaran özelliklerden bazılarıdır. Tüm bu avantajlar hiperspektral görüntülemeyi çimento analizi için çok uygun hale getirmektedir.

En yaygın kullanılan yapı malzemelerinden biri olan Portland çimentosu, farklı bileşiklere sahip karmaşık bir yapıya sahiptir. Bileşiklerinin her biri, hidrasyon işlemi sırasında benzersiz bir dizi reaksiyon kinetiğine sahiptir. Her bir reaksiyonun incelenmesi bir dizi özel ve karmaşık test gerektirdiğinden, bu ayrıntıları gözlemlemenin daha uygun yollarını bulmak oldukça talep görmektedir.

Bu alıřma, imento bileřiklerinin tespitinde hiperspektral grntlemenin kullanımına iliřkin ilk alıřmadır. Arařtırma, imento bileřiklerinin zelliklerini deęerlendirmek iin grnr ve yakın kızıltesi spektral aralıktta (400 ila 1000 nm) yansıma hiperspektral spektroskopisini kullanmaktadır. Her bir bileřik laboratuvarında yksek saflıktta retiliyor ve fiziksel, kimyasal ve mekanik zellikleri hiperspektral imzalarıyla birlikte kapsamlı bir řekilde inceleniyor.

Bu bileřikler sentezlendikten sonra, rastgele seilen imento klinkerlerinin sınıflandırılması iin temel oluřturan hiperspektral veriler toplanır. Bu sınıflandırmanın doęruluęu, Matlab'daki Derin ęrenme Ara Kutusu kullanılarak, zellikle bir Lojistik Regresyon ekirdek modeli kullanılarak deęerlendirilmiřtir. zellikle, bu model hiperspektral grntleme yoluyla farklı imento trlerini sınıflandırmada %98,25'lik bir doęruluk elde etmiřtir.

Anahtar Kelimeler: imento Sentezi, Hiperspektral Grntleme Analizi,
Hiperspektral İmza, Malzeme Karakterizasyonu

To my beloved family...

ACKNOWLEDGMENTS

The successful completion of this thesis owes much to the invaluable support and encouragement extended by special people in my life. First and foremost, I extend my sincere thanks to my supervisor, Prof. Dr. Ismail Özgür Yaman, for his invaluable guidance, unwavering support, and diligent supervision.

I am grateful to Dr. Burhan Alam, my co-advisor, but more than an advisor, my brother. His boundless support and motivation have transcended the boundaries of this thesis, encompassing my entire life. I appreciate his trust and the reassurance that he is always there for me.

I extend my deepest appreciation to my committee members, Prof. Dr. Mustafa Şahmaran, Assoc. Dr. Hande Işık Öztürk, Assoc. Prof. Dr. Çağla Akgül, and Asst. Prof. Dr. Emin Şengün, for their insightful recommendations that significantly contributed to enhancing the quality of this thesis.

Special thanks to Prof. Dr. Sinan Turhan Erdoğan, my master advisor, for introducing academic life to me and his guidance. I also express my gratitude to Prof. Dr. Mustafa Tokyay for imparting extensive knowledge about construction materials.

I would like to express my heartfelt gratitude to my parents. I am truly thankful for their unwavering trust and support and unconditional love at every step I have taken. I am incredibly fortunate and proud to be their daughter. I also express my endless gratitude to my sister Nesim and my brother Mehdi. Just like my second parents, they have been there whenever I needed support and your unwavering help means the world to me, I am so lucky to have you in my life.

I thank my dear friend Shima Ebrahimi from the bottom of my heart. For sharing every moment of this 6-year PhD adventure with me and always being by my side unconditionally, for making me laugh even in my worst days and for making my life

better with her positive energy. Even though we were miles apart she never left me alone for a moment.

I am immensely thankful to Dr. Meltem Tangüler Bayramtan. Her constant presence and swift assistance whenever I faced challenges during this thesis process have been invaluable. I couldn't have completed this thesis without your unwavering support.

My great appreciation to my friends Dr. Leili Nabdell and Dr. Saman Aminbakhsh, for their great friendship, moral support, and motivation and for all the fun and crazy memories they made in my life.

My heartfelt thanks, which words alone cannot express, go to Dr. Sepeh Seyediyan, Özgür Paşaoğlu, and Pinar Arikoğlu. Their support in my most difficult days was crucial, and without them, I might not be where I am today.

I am eternally indebted to all the members of the Materials of Construction Laboratory group, of which I am honored to be a part. Special thanks to Thanks to Cuma Yıldırım, Gülşah Bilici for their help. I would like to thank all my friends Dr. Kemal Ardoğa, Mahyar Azizi, Görkem Bayramtan, Aykut Bilginer, Dr. Muhammet Atasever, Berkay Akcoren, Özdeş çelik, Iraj Sharifi, Muhammed Sherzai, Hossein Mazaheri who color my life and made my stay in Ankara memorable.

Last but not least, I would like to thank my husband Salar Ahmadi for coming into my life during the most stressful times of this thesis and for making every stages of my life better and funner with his support and motivation.

The analysis of the industrially produced clinker was performed by TURKCIMENTO, their support is acknowledged.

This study is fully funded with a 1001 grant by Scientific and Technological Research Council of Türkiye (TÜBİTAK) under grant number TÜBİTAK 119M096. This support is gratefully acknowledged.

TABLE OF CONTENTS

ABSTRACT	v
ÖZ.....	vii
ACKNOWLEDGMENTS	x
TABLE OF CONTENTS	xii
LIST OF TABLES	xvi
LIST OF FIGURES	xviii
1 INTRODUCTION	1
1.1 General	1
1.2 Objective and Scope	2
2 LITERATURE REVIEW	5
2.1 History of Hyperspectral Imaging	5
2.2 What Is Electromagnetic Spectrum	7
2.3 What Is Spectroscopy	8
2.4 Principle of Hyperspectral Imaging.....	9
2.5 Scanning Techniques of Hyperspectral Imaging Systems	12
2.5.1 Point Scanning	13
2.5.2 Line Scanning	14
2.5.3 Area Scanning (Wavelength Scan).....	15
2.5.4 Snapshot Scanning.....	16
2.6 Image Acquisition Modes.....	17
2.6.1 Reflectance Mode	17
2.6.2 Transmission Mode.....	18

2.6.3	Interaction Mode	19
2.7	Hyperspectral Data.....	20
2.8	Pre-Processing Of Hyperspectral Data	21
2.8.1	Smoothing	22
2.8.2	Multiplicative Scatter Correction	23
2.8.3	Standard Normal Variate (SNV)	24
2.8.4	Derivatives	25
2.9	Cement Compounds.....	26
2.9.1	Manufacturing Process	26
2.9.2	Hydration of Portland Cement	28
2.9.3	Synthesis of Pure C ₃ S.....	31
2.9.4	Synthesis of Pure C ₂ S.....	36
2.9.5	Synthesis of Pure C ₃ A	39
2.10	Characterization of Materials by Hyperspectral Imaging	42
3	EXPERIMENTAL PROGRAM	47
3.1	The Hyperspectral Imaging System.....	47
3.1.1	The Hyperspectral Camera.....	48
3.1.2	The Microscope.....	49
3.1.3	The Hyperspectral Imaging Software	49
3.2	Raw Materials	51
3.2.1	Calcium Carbonate, CaCO ₃	52
3.2.2	Quartz, SiO ₂	52
3.2.3	Aluminum Oxide, Al ₂ O ₃	53
3.2.4	Minor Stabilizers	54

3.3	Synthesis Processes of Cement Compounds	54
3.3.1	C ₃ S Synthesis	55
3.3.2	C ₂ S Synthesis	57
3.3.3	C ₃ A Synthesis	58
3.4	Sample Preparation for Pastes	58
3.5	The Physical Properties of the Cement Compounds	59
3.6	Sample Preparation For HSI	60
3.6.1	Thin Sectioning	60
3.6.2	Polished Sectioning	61
3.7	Characterization Methods	61
3.7.1	X-ray Diffraction (XRD) Analysis	62
3.7.2	Fourier Transform Infrared Spectroscopy (FTIR) Analysis	62
3.7.3	Isothermal Calorimetry Testing	63
3.7.4	Compressive Strength Testing	64
3.7.5	Modulus of Elasticity	65
3.7.6	Scanning Electron Microscopy (SEM)	67
4	RESULTS AND DISUSSION	69
4.1	Use of Conventional Techniques for Characterization of Cement Compounds	69
4.1.1	X-Ray Diffraction Results	69
4.1.2	Fourier Transform Infrared Results	70
4.1.3	Microstructural Characterization of Clinker Compounds through Scanning Electron Microscopy	71
4.2	Characterization of the Hydration Behavior of the Cement compounds	76

4.2.1	Physical Properties of the Ground Cement Clinker	76
4.2.2	Heat Evolution (Isothermal Calorimetry)	78
4.2.3	X-Ray Diffraction Analysis of the Hydrated Compounds	81
4.2.4	FTIR Analysis of the Hydrated Compounds	87
4.2.5	Compressive Strength Testing	89
4.2.6	Modulus of Elasticity	93
4.2.7	Microstructural Characterization of Hydrated Clinker Compounds through Scanning Electron Microscopy	93
4.3	Hyperspectral Imaging Results	102
4.3.1	General	102
4.3.2	Ground Portland Cement Clinker Compounds	112
4.3.3	Analysis of an Industrial Clinker	115
4.3.4	Hyperspectral Imaging Results of Hydrated Cement Clinker Compounds 123	
CHAPTER 5		129
5	SUMMARY, CONCLUSIONS AND RECOMMENDATIONS.....	129
REFERENCES		133
CURRICULUM VITAE (Only For Doctoral Thesis)		157

LIST OF TABLES

TABLES

Table 2-1 Weight of raw materials are used for synthesizing C ₃ S (Quennoz, 2011)	31
Table 2-2 Mix composition for 100 g of final C ₃ S product (Wesselsky & Jensen, 2009).....	34
Table 3-1 Raw materials proportions for synthesizing C ₃ S	56
Table 3-2 Raw materials proportions for synthesizing C ₂ S	58
Table 3-3 Raw materials proportions for synthesizing C ₃ A.....	58
Table 3-4 Grinding duration and rotational speed for each cement compound with Retsch ball mill grinder	59
Table 3-5 Water to cementitious material ratio	65
Table 3-6 Properties of used strain gauges	66
Table 4-1 Peak lists of FTIR results for synthesized C ₃ S, C ₂ S, and C ₃ A.....	71
Table 4-2 Density results of synthesized C ₃ S, C ₂ S, and C ₃ A.....	76
Table 4-3 Passed ratio (%) of particles for each cement compound	77
Table 4-4 Peak list of FTIR results for pure C ₃ S, C ₂ S, 28 days and 90 days hydrated form	88
Table 4-5 Peak list of FTIR results for pure C ₃ A, 28 days and 90 days hydrated form	89
Table 4-6 Elemental analysis of produced C-S-H gel from hydration of C ₃ S	96
Table 4-7 Elemental analysis of produced C-S-H gel from hydration of C ₂ S	96
Table 4-8 Positions of local minima and maxima for pre-processed data of C ₃ S.	108
Table 4-9 Positions of local minima and maxima for pre-processed data of C ₂ S.	110
Table 4-10 Positions of local minima and maxima for pre-processed data of C ₃ A	112
Table 4-11 comparison of real mixed ratio and HSI classification results.....	113
Table 4-12 Summary results of Deep Learning process	114

Table 4-13 Rietveld results for the industrial clinker	117
Table 4-14 Chemical Analysis and the Compound Composition of the Clinker .	117
Table 4-15 Results of optical polarized light microscope phase detection.....	120
Table 4-16 Classification results of the generated model and the quantitative results taken from the HSI setup.	122
Table 4-17 Comparison of classification results for different methods of testing	122

LIST OF FIGURES

FIGURES

Figure 2-1 Energy and electromagnetic spectrum (Szantoi, 2013)	8
Figure 2-2 Mechanism of turning light to a digital file (Anghel, 2021).....	10
Figure 2-3 Decomposition of white light to red, green and blue colors (Bartczak, 2016).....	11
Figure 2-4 Different working principle of hyperspectral cameras, A) Point scanning, B) Line scanning, C) Area scanning, D) Snapshot (Y. W. Wang et al., 2017).....	16
Figure 2-5 Three diferent modes to generate a hyperspectral image. (a) The relectance mode. (b) The transmittance mode. (c) The interactance mode(X. Li, Li, et al., 2018).....	18
Figure 2-6 Hypercube data for different wavelenghtes (z) in vaarious spatial (x, y) domains (Manley, 2014b).....	21
Figure 2-7 Firing procedure of C ₃ S according to (Quennoz, 2011)	31
Figure 2-8 Results of (a) SEM, (b) XRD for C ₃ S (Quennoz, 2011)	32
Figure 2-9 XRD results of triclinic C ₃ S	34
Figure 2-10 The crystal transformation rate of β -C ₂ S to γ -C ₂ S with different cooling methods (Zhao, 2012).....	38
Figure 2-11 phase transition behavior of the CaO-Al ₂ O ₃ binary (Wesselsky & Jensen, 2009)	40
Figure 2-12 The source image (a) comprises clean aggregates, mortar-covered aggregates, and partially liberated aggregates, while the corresponding prediction image (b) results from the application of PLS-DA, illustrating the classification into aggregates (A) and mortar (M), along with the micro-XRF map (Bonifazi et al., 2018).....	43
Figure 2-13 Average reflectance spectra in the wavelength range of 1200 nm to 2400 nm for samples with a W/C ratio of: (a) 0.6, (b) 0.5, and (c) 0.4 (Fan et al., 2020).....	44

Figure 3-1 (a) Hinalia hyperspectral camera mounted on the microscope, (b) Truescope software interface	47
Figure 3-2 The Hinalia Model 4200 hyperspectral camera.....	48
Figure 3-3 The working principle of FPI filter used in HS camera (Fong et al., 2018)	50
Figure 3-4 scale of 1 mm in pixel measurements	51
Figure 3-5 XRD pattern of TEKKIM CaCO ₃	52
Figure 3-6 XRD pattern of SiO ₂	53
Figure 3-7 XRD pattern of Al ₂ O ₃	53
Figure 3-8 Protherm ELV MOS 160 furnace showing the elevated specimen holding platform on the right	55
Figure 3-9 Hot crucible while removed from the furnace	56
Figure 3-10 Heating regimes of the oven during the synthesis of cement compounds	57
Figure 3-11 Thin sections of cement compounds	60
Figure 3-12 Steps for molding cement compound for polish sectioning for HIS...	61
Figure 3-13 Cubic specimen molds for compressive strength test with side of 2.5 cm.....	64
Figure 3-14 (a) Attached strain gauge to the cylindrical specimen, (b) capped cylindrical specimens.....	66
Figure 4-1 XRD patterns of synthesized C ₃ S, C ₂ S, and C ₃ A, where the peaks are for the pure form of each compound.....	69
Figure 4-2 FTIR patterns of synthesized C ₃ S, C ₂ S, and C ₃ A	71
Figure 4-3 SEM images of synthesized C ₃ S (a) 1000 x (b) 500 x, (c) 1000 xx, (d) EDX of (b)	72
Figure 4-4 SEM images of synthesized C ₂ S (a) 1000 x, (b) 500 x, (c)5000 x, (d) 5000 x, (e) EDX of (b)	73
Figure 4-5 SEM images of synthesized C ₃ A (a) 1000 x, (b) 2500 x, (c)1000 x, (d) 5000 x, (e) EDX of (a)	75

Figure 4-6 Particle size distribution of synthesized C_3S , C_2S , and C_3A , CEM I, and average of synthesized C_3S , C_2S , and C_3A	77
Figure 4-7 heat evolution of cement compounds during the initial 100 hours.....	79
Figure 4-8 Cumulative heat profiles over a period of 28 days for cement compounds.....	80
Figure 4-9 Temperature increases of C_3A during first minutes of hydration according to thermal camera	81
Figure 4-10 XRD patterns of air cured C_3S pastes after 1, 3, 7, 28, 90, 180 days of hydration.....	82
Figure 4-11 XRD patterns of water cured C_3S pastes after 1, 3, 7, 28, 90, 180 days of hydration	83
Figure 4-12 XRD patterns of air cured C_2S pastes after 3, 7, 28, 90, 180 days of hydration.....	84
Figure 4-13 XRD patterns of air cured C_3A pastes after 1, 3, 7, 28, 90 days of hydration.....	85
Figure 4-14 XRD patterns of air cured $C_3A + G$ pastes after 1, 3, 7, 28, 90 days of hydration.....	87
Figure 4-15 Results of FTIR test for synthesized C_3S , C_2S , and C_3A and their hydrated form after 28 and 90 days	88
Figure 4-16 (a) Cubic molds for compressive strength test with side of 2.5 cm, (b) unmolded samples from the mold shown in (a)	90
Figure 4-17 Cracks generation after 4 days of hydration in C_3A sample.....	90
Figure 4-18 Compressive strength results of synthesized C_3S , C_2S , and $C_3A + G$, after 1, 3, 7, 28, 90 and 180 days of hydration	91
Figure 4-19 Comparison of air curing and water curing on results of Compressive strength for synthesized C_3S , C_2S , after 1, 3, 7, 28, 90 and 180 days of hydration	92
Figure 4-20 SEM images of 28- day hydrated C_3S , (a) 1000 x, (b) 5000 x, (c) 1000 x, (d) 5000 x, (e) EDX results of (a), (f) EDX of specified part at (d).....	95
Figure 4-21 SEM images of 28- day hydrated C_2S , (a) 1000 x, (b) 5000 x, (c) 5000 x, (d) 5000 , (e) EDX results of (a).....	97

Figure 4-22 SEM images of 28- day hydrated C_3A , (a) 1000 X, (b) 5000 X, (c) 5000 X, (d) 20000 , (e) EDX results of (a)	99
Figure 4-23 images of 28- day hydrated $C_3A + G$, (a) 1000 X, (b) 10000 X, (c) 10000 X, (d) 25000 X, (e) 40000 X, (f) EDX results of (a)	101
Figure 4-24 Transmittance mode hyperspectral image results for cement compounds	102
Figure 4-25 Locations of 10 random readings from polished sections.....	103
Figure 4-26 Microscopic HSI of C_2S with 10x magnification.....	104
Figure 4-27 Hyperspectral imaging results of cement clinker compounds	104
Figure 4-28 Results of applied preprocessing methods to the raw data (a) SNV, (b) MSC, (c) first order derivatives, (d) second order derivatives, (e) Savitzky-Golay	106
Figure 4-29 Pre-processed data and determination of local minimum and maximum for C_3S	107
Figure 4-30 Pre-processed data and determination of local minimum and maximum for C_2S	109
Figure 4-31 Pre-processed data and determination of local minimum and maximum for C_3A	111
Figure 4-32 Classified hyperspectral image of C_3S , C_2S and C_3A	113
Figure 4-33 The validation confusion matrix of Kernel Logistic Regression model (PPV: Positive Predictive Values, FDR: False Discovery Rates).....	115
Figure 4-34 Results of XRD analysis for industrial clinker sample	116
Figure 4-35 (a) and (b) Crystals of C_3S (brown) and C_2S (blue) under light microscope with 100x magnification, (c) Crystals of C_3A , gray crystals on a cream background under 500x magnification	119
Figure 4-36 Crystal size distribution for C_3S and C_2S	120
Figure 4-37 (a) Hyperspectral image of cement, (b) categorized cement clinker.	121
Figure 4-38 Average of hyperspectral data recordings from hydrated C_3S after 1, 3, 7, 28 days	123

Figure 4-39 Average of hyperspectral data recordings from hydrated C ₂ S after 1, 3, 7, 28 days.....	124
Figure 4-40 Average of hyperspectral data recordings from hydrated C ₃ A after 1, 3, 7, 28 days.....	125
Figure 4-41 Preprocessed hyperspectral data for (a) C ₃ S, (b) C ₂ S and (c) C ₃ A....	126

CHAPTER 1

INTRODUCTION

1.1 General

Cementitious materials have played a pivotal role throughout history as essential binders, and Portland cement is used as the primary binder in the highly consumed building material, concrete (Gagg, 2014). This complex material consisting of various compounds like tricalcium silicate (C_3S), dicalcium silicate (C_2S), tricalcium aluminate (C_3A), and tetra calcium alumina ferrite (C_4AF), reacts with water and gains strength through hydration. A comprehensive understanding of the chemical, physical, and mechanical properties of Portland cement is critical in the quest to produce superior quality cements that can yield concretes with increased strength and durability.

The production of Portland cement is a complex process that is influenced by a variety of parameters (D. Herfort & Macphee, 2019). While there is a wealth of testing methods to analyze the production process and methods, such as X-ray diffraction (XRD), Fourier transform infrared spectroscopy (FTIR), and optical and scanning electron microscopy (SEM), it is worth noting that these techniques often require complex sample preparation procedures, expensive testing equipment, and the expertise of specialized personnel to interpret the results.

As technology has advanced, new testing methods have emerged, notably hyperspectral imaging systems, which have found utility not only in materials analysis, but also in fields such as the food industry (Ma et al., 2019). Hyperspectral cameras are equipped to capture both spatial and spectral information from the surfaces of samples (Gowen et al., 2007). By quantifying the signals of different

wavelengths and their respective intensities, researchers can construct a spectral profile that captures the unique characteristics of the material under study. Hyperspectral cameras have the ability to span a continuous wavelength range from 400 to 2500 nanometers (Ewald et al., 2016). The selection of the specific wavelength region is highly dependent on the material being studied, as each spectral region corresponds to different atomic or molecular transitions associated with different energy levels.

The data acquired through hyperspectral cameras is stored in the form of a data cube, representing a substantial volume of data in three dimensions. The two spatial dimensions, denoted as x and y, provide information regarding the sample's spatial attributes, while the third dimension, z, encapsulates the spectral data specific to each point on the sample (Mateen et al., 2018). To harness the potential of hyperspectral imaging data, various analytical techniques can be employed, including spectral unmixing, principal component analysis, and machine learning algorithms. These methodologies facilitate the extraction of pertinent information from the data and enhance the precision of the results (Charles et al., 2011).

Hyperspectral imaging systems have been used in various fields such as the food industry, pharmacology, medicine, and numerous other fields. While there have been studies demonstrating the effective utility of hyperspectral imaging in the detection of building materials, There has been a limited number of studies exploring the use of hyperspectral imaging for the characterization of concrete or cementitious systems. This study will be the first to assess the compounds of Portland cement and the hydration of these compounds using HSI.

1.2 Objective and Scope

The primary goal of this study is to explore the technical feasibility of employing hyperspectral imaging (HSI) for characterizing Portland cement features. To achieve this goal, the thesis is structured around three specific objectives. The first objective

involves synthesizing high-purity Portland cement compounds, specifically C_3S , C_2S , and C_3A . Subsequently, these compounds will be characterized using traditional methods in conjunction with HSI. As part of the second objective, HSI will be employed for identifying each of these compounds within a blend. Lastly, the third objective focuses on investigating the potential use of HSI in characterizing hydrated compounds.

This thesis is divided into five chapters. The introductory chapter sets the stage for the research. The second chapter provides a detailed exploration of hyperspectral cameras, data processing techniques, and cement characterization through a comprehensive literature review. The third chapter provides a thorough explanation of the Portland cement compound synthesis process and the experimental methods employed. In the fourth chapter, the experimental results related to cement compounds and cement pastes along with their hyperspectral analysis results are meticulously compiled and analyzed. Finally, Chapter 5 summarizes the conclusions of the study and provides valuable recommendations for future research.

CHAPTER 2

LITERATURE REVIEW

2.1 History of Hyperspectral Imaging

Hyperspectral imaging, also known as imaging spectroscopy, is a relatively new technology that has rapidly gained popularity in various fields of research and industry. This imaging technique has enabled researchers to gather detailed spectral data that can be used to study the properties and characteristics of a wide range of materials, including gases, liquids, and solids (B. Wang et al., 2021).

The history of hyperspectral imaging dates back to the early 20th century when scientists first began to study the spectral characteristics of materials using spectrometers (Selci, 2019). Those devices were initially developed in the late 1800s to study the spectral characteristics of light emitted by stars. However, by the early 1900s, spectrometers had expanded to study materials on Earth, such as plants (Thomas, 1991).

In the 1930s, researchers started using spectrometers to study the reflectance spectra of vegetation (Thomas, 1991). This led to the development of remote sensing techniques for studying the Earth's resources, such as minerals, water, and vegetation. The technology was used by NASA in the 1960s and 1970s to study and monitor land and vegetation changes (Goetz, 2009).

In the 1970s, imaging spectrometry was developed as a part of the Earth Resources Technology Satellite (ERTS) program by NASA's Jet Propulsion Laboratory (Giardino, 2012). The ERTS program aimed to provide high-resolution satellite imagery for studying the Earth's natural resources, such as vegetation, minerals, and water. Hyperspectral imaging data obtained from the ERTS program allowed

researchers to obtain detailed spectral data for studying the Earth's surface and resources (Calin et al., 2021; Goetz, 2009).

The development of hyperspectral imaging technology accelerated in the 1980s, when the first commercial hyperspectral sensors became available. Hyperspectral imaging technology began to be used in various fields, such as remote sensing, agriculture, geology, and military reconnaissance (Goetz, 2009; B. Lu et al., 2020; Padoan et al., 2008; Xing et al., 2019). Particularly, hyperspectral imaging technology applications for military reconnaissance were created during this period. (Manolakis & Shaw, 2002).

In the 1990s, the use of hyperspectral imaging technology expanded further into fields such as medical imaging and mineral exploration. In medical imaging, hyperspectral imaging technology was used to improve the diagnosis of various diseases and conditions, such as skin cancer (Calin et al., 2014; De Beule et al., 2007; G. Lu & Fei, 2014; Martin et al., 2006; Panasyuk et al., 2007). In mineral exploration, hyperspectral imaging technology was used to identify and map mineral deposits (Krupnik & Khan, 2019; Tripathi & Govil, 2019).

The development of hyperspectral imaging technology continued into the 21st century, with the introduction of more advanced sensors and imaging techniques. These advancements have enabled hyperspectral imaging technology to be used in even more fields, such as food quality inspection and precision agriculture (Dale et al., 2013; Hartel et al., 2015; R. Lu & Chen, 1999; D. W. Sun, 2010).

One of the most significant advancements in hyperspectral imaging technology in recent years has been the development of unmanned aerial vehicles (UAVs) equipped with hyperspectral sensors. These UAVs have revolutionized the field of remote sensing, allowing researchers to obtain high-resolution hyperspectral images of large areas of land quickly and at a lower cost than traditional remote sensing methods (Adão et al., 2017; B. Lu et al., 2020; M. B. Stuart et al., 2019; Zhong et al., 2018).

2.2 What Is Electromagnetic Spectrum

The electromagnetic spectrum is categorized into regions based on the frequency or wavelength of the radiation, which corresponds to different energy levels. Each region has its unique properties and characteristics (Ball, 2007). The electromagnetic spectrum comprises all the various forms of electromagnetic radiation, which include gamma rays, X-rays, ultraviolet radiation, visible light, infrared radiation, microwaves, and radio waves as it is shown in Figure 2-1 (Sharma, 1981; Zamanian & Hardiman, 2005).

At the high-energy end of the spectrum, gamma rays and X-rays have the shortest wavelengths and highest frequencies. These types of radiation are highly ionizing and can pose a significant danger to living organisms in large doses. On the other hand, ultraviolet radiation, which has slightly longer wavelengths and lower frequencies, is responsible for skin damage and sunburns (Clydesdale et al., 2001; Hill, 2004; Sharma, 1981; Zamanian & Hardiman, 2005).

Visible light is the portion of the electromagnetic spectrum that human eye can perceive, and it spans from approximately 400 to 700 nanometers in wavelength. Different colors of the rainbow correspond to varying wavelengths of visible light (Balchin, 2021).

Infrared radiation has longer wavelengths and lower frequencies than visible light, and it produces heat radiation (Dawson, 2005; Jun et al., 2010). Microwaves have even longer wavelengths and are utilized in communication and heating applications, such as microwave ovens (Osepchuk, 1984). Radio waves, which have the longest wavelengths and lowest frequencies in the spectrum, are used in communication, broadcasting, and navigation (Ball, 2007).

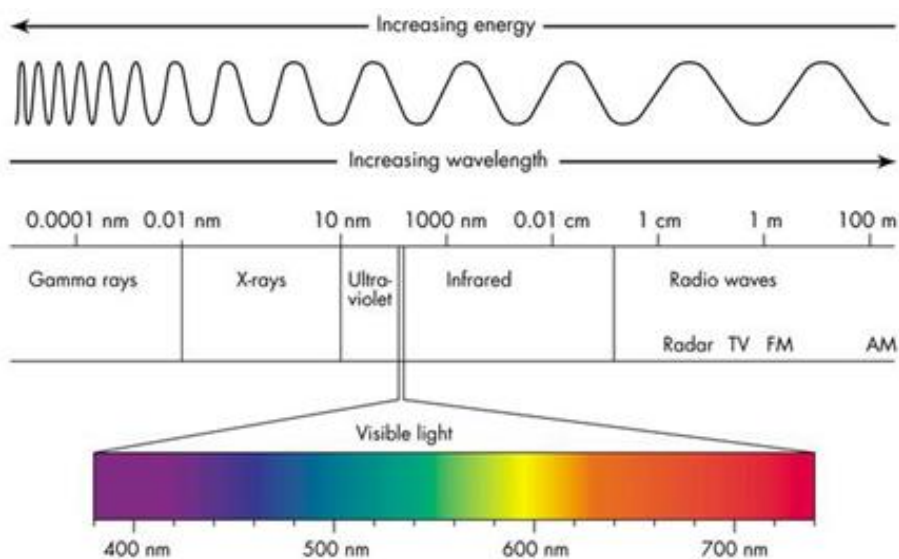


Figure 2-1 Energy and electromagnetic spectrum (Szantoi, 2013)

2.3 What Is Spectroscopy

Spectroscopy is a technique that enables scientists to study chemical constituents of samples by analyzing the energy transfer between waves and matter and is a powerful and versatile tool that has applications in various fields, including chemistry, physics, astronomy, and medicine (Mandal & Paul, 2022; Mirabella, 1998; Pavia et al., 2008). Various forms of spectroscopy can be employed to measure different aspects of the interaction between matter and electromagnetic radiation. Absorption spectroscopy, for instance, quantifies the extent to which the sample absorbs radiation across different wavelengths. Conversely, fluorescence spectroscopy quantifies the amount of radiation discharged by the sample following excitation with a light source (Albani, 2008; Penner, 2017).

Spectroscopic analysis utilizes the interaction between atoms or molecules and electromagnetic radiation to extract qualitative and quantitative chemical and physical data present within the wavelength spectrum.

2.4 Principle of Hyperspectral Imaging

Imaging has been a vital aspect of human civilization since ancient times. Early forms of imaging, such as cave paintings and hieroglyphics, were used for communication and documentation of events. However, it was not until the 19th century that significant progress was made in the development of imaging technology (Beck, 1990; Khosla, 1992). The invention of the camera obscura and later the daguerreotype by Louis Daguerre in 1839 revolutionized the way images were captured and preserved. Over the years, advancements in imaging technology continued to push the boundaries of what was possible, from the first X-ray image by Wilhelm Conrad Roentgen in 1895 to the development of computed tomography (CT) and magnetic resonance imaging (MRI) in the 20th century (Anthony Seibert, 1995; Bracco et al., 2019; Ghosh & Pal, 2022; Wolbarst, 1999).

Currently, the most common imaging system relies on visible light to produce digital images. This system is shown in Figure 2-2, a series of sensors that are affected by light record the colors that make up the image onto a matrix. These sensors, which come in different types, work by converting perceived colors into electrical signals. Consequently, depending on the sensitivity of the sensor used, different electrical signals are generated for each color tone. The resolution of the images recorded by this sensor array depends on the number of sensors used. Each color information of the digital image is obtained from a single sensor in the array, and the points that make up the digital image are called pixels. The more pixels in an image, the more details it contains. The main stages of this process are illustrated below (Nakamura, 2017; Tarrant, 2003; Tatsuno, 2006; Trussell & Vrhel, 2008).

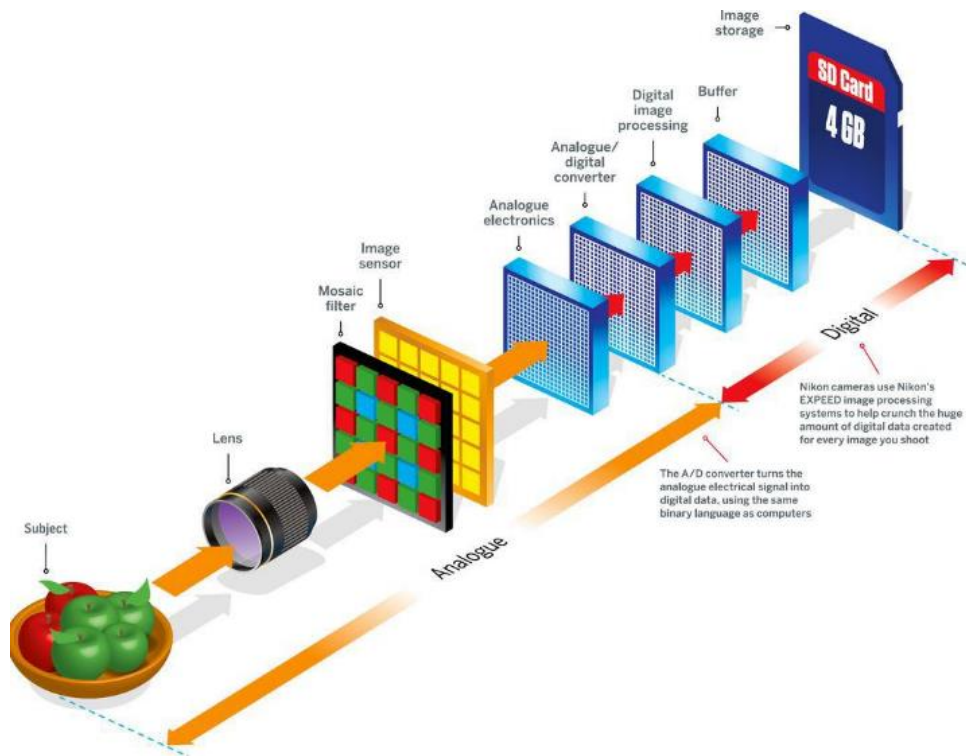


Figure 2-2 Mechanism of turning light to a digital file (Anghel, 2021)

In digital imaging, the amount of red, green, and blue lights reflected or emitted from the object is measured. Incoming light from the sample enters the device through an entrance (incoming light), and a holographic grating separates it into component wavelengths, as shown Figure 2-3. In simple terms, the grating separates each color from white light. A pixel (the smallest element in an array) measures the intensity of each color in the visible spectrum, and the data gathered is subsequently read by a computer. As a result, a spectrum that displays the intensity of every wavelength of light is produced. (Brelstaff et al., 1995; Nakamura, 2017; Peiris et al., 1999; Tatsuno, 2006).

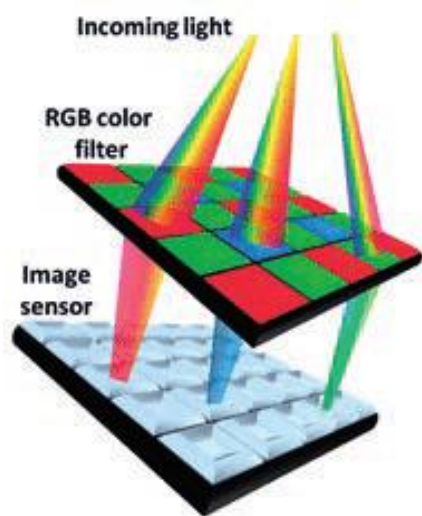


Figure 2-3 Decomposition of white light to red, green and blue colors (Bartczak, 2016)

This technique captures color information and produces images that appear similar to what the human eye would see. On the other hand, spectral imaging captures a much wider range of information beyond just color. Spectral imaging covers all spectral regions, including visible, near-infrared, short-wave infrared, mid-wave infrared, and long-wave infrared, all spatial domains from microscopic to macroscopic scales, and all types of matter including solid, liquid, and gas (Hagen & Kudenov, 2013). All materials with a temperature above 0 K possess the ability to emit electromagnetic energy.

Hyperspectral imaging is a method of acquiring data across a broad range of wavelengths, providing a comprehensive analysis of the spectral characteristics of the imaged object. These images are captured using hyperspectral imaging systems, also known as imaging spectrometers, which consist of three primary components (Garini et al., 2006; Rasti et al., 2020; Tan, 2016). The first component is a light source that illuminates the object's surface during the imaging process. The second element is a spectral separator that divides the reflected light into tens or hundreds of spectral bands. This device can be a prism, grating, or optical bandpass filter. The

application may require this component to be fixed or adjustable. A detector that catches the two-dimensional image with spectral data included in each pixel makes up the third component. (Ghamisi et al., 2017; Khan et al., 2018; Lodhi et al., 2019).

As the object is illuminated during the imaging process, the light interacts with it, either being reflected, transmitted, or absorbed. The diffuse reflected light then passes through the spectral separator, which separates it into tens or hundreds of spectral bands. The resulting light is then captured by the detector, which produces a two-dimensional image with spectral data inherent in each pixel (Chein-I Chang, 2003; Shippert, 2021).

The data acquired from hyperspectral imaging systems is then transferred to a computer for further analysis and processing. Hyperspectral imaging systems have practical applications in numerous fields, including mineralogy, agriculture, biomedical imaging, and remote sensing (R. Lu & Chen, 1999; M. Stuart et al., 2019; Yoon, 2022; Yuen & Richardson, 2010). This technique enables the identification of materials and properties in a scene by analyzing the spectral signatures of different pixels, providing a detailed map of the distribution of different materials or properties in the scene(Khan et al., 2018).

2.5 Scanning Techniques of Hyperspectral Imaging Systems

Over the last few decades, a variety of spectral imaging techniques and associated technologies have been suggested for obtaining spectral image data. This passage describes four different methods that can be utilized to obtain three-dimensional hyperspectral image cubes, also referred to as hypercubes (x, y, l). They are: point scanning, line scanning, area scanning, and the single shot method (An et al., 2022; B. Lu et al., 2020; Ma et al., 2019).

2.5.1 Point Scanning

Point scanning (Whiskbroom) is a method used in spectral cameras to acquire hyperspectral data (ElMasry & Sun, 2010; Funatomi et al., 2022). It involves scanning a single pixel on the sample or object to collect spectral data at different wavelengths (Figure 2-4 (A)). This process is repeated multiple times in x and y directions for each pixel, resulting in a two-dimensional image and gather spectral information simultaneously for each pixel. Point scanning is a slow process and requires precise mechanical movement, but it can produce high-resolution images with high spectral accuracy. It is often used in applications where high spectral resolution is necessary, such as in biomedical imaging or material analysis (Q. Li et al., 2013). The whiskbroom imaging method has a number of benefits, such as the ability to adjust the depth of field, reduce background clutter outside the focal plane, and produce serial optical sections from thick samples. Additionally, this method requires fewer sensor detectors to maintain calibration compared to other sensor types. As a result, many commercial spectral confocal scanning instruments use whiskbroom imaging (Bruning et al., 2020).

The point scanning technique in hyperspectral imaging has several disadvantages compared to other techniques, such as push-broom scanning or snapshot imaging. The sequential acquisition of spectral data for each point in the scene makes point scanning inherently slow, limiting its applicability in time-sensitive applications or for capturing dynamic processes. Additionally, motion artifacts can be introduced into the acquired data due to the movement of the camera or scene, making it problematic for observing moving objects or when the camera is mounted on an unstable platform. Point scanning hyperspectral cameras also have a limited field of view, increased complexity, and a higher risk of spatial misregistration, which can result in image distortion or artifacts. Furthermore, point scanning systems may have a lower signal-to-noise ratio compared to other techniques, reducing image quality and ability to discriminate between different materials or features in the scene, especially in low-light conditions. Thus, these limitations can restrict the

applicability of the point scanning technique in certain applications and make it less preferable compared to other hyperspectral imaging techniques (Baek et al., 2017; Gutiérrez-Gutiérrez et al., 2019).

2.5.2 Line Scanning

Line scanning (push-broom) scanning is a frequently utilized hyperspectral imaging technique that provides rapid and continuous spectral data acquisition is demonstrated in Figure 2-4 (B). The method involves the use of a slit aperture to collect reflected light from the scene, with a sensor array capturing multiple spatial pixels simultaneously in a single frame. As the camera advances, a continuous line of pixels is obtained, and this process is repeated for each subsequent line until the entire image is collected. Every pixel in the image contains a complete spectrum of the reflected light, allowing for the examination of spectral information throughout the entire image (Arce et al., 2014; Jurado et al., 2021; Qin et al., 2017).

Push-broom scanning offers several advantages over other hyperspectral imaging techniques. One of its primary advantages is its high spatial and spectral resolution, enabling the detection and identification of small features and subtle differences in materials. Its ability to cover large areas rapidly also makes it ideal for environmental monitoring, land use mapping, and geological exploration applications (Gamez et al., 2012; Pitak et al., 2021).

Push-broom scanning has some limitations that must be considered. One drawback is its sensitivity to motion disturbances, which may arise if the camera or the subject being imaged moves during data acquisition. This can result in spatial misregistration and image distortion, potentially impacting the accuracy of spectral analysis. Additionally, its high cost can be a constraint for certain applications (Gu et al., 2022).

Despite these limitations, push-broom scanning remains a prominent and widely employed hyperspectral imaging technique, due to its high spatial and spectral

resolution, fast data acquisition, and broad applicability in fields such as remote sensing, agriculture, and mineral exploration (Jurado et al., 2021; Ortega et al., 2019).

2.5.3 Area Scanning (Wavelength Scan)

Area scanning is a prevalent technique for hyperspectral imaging with cameras. It involves acquiring a single-color, two-dimensional image with complete spatial information at a single wavelength and repeating the process across the entire spectral range. The principle of working is depicted in Figure 2-4(C). The resulting stack of single-band images is in a band sequential (BSQ) format, which codes each row of the image in the first band, followed by the next row in the same spectral band, and so on until all band numbers are complete (Song et al., 2021). This format facilitates easy access to spatial information in a single spectral band (Bodkin et al., 2009; Klein et al., 2008).

The area scanning technique has a number of benefits. It makes it possible to adjust the depth of field and reduce or remove background distractions from the focus point. It is a good option for many commercial spectral confocal scanning devices since it also enables the collecting of serial optical sections from thick specimens and has fewer sensors to calibrate than other types of sensors. Additionally, this method permits each wavelength to have an appropriate exposure time since the detector is only exposed to a single wavelength at a time. Moreover, it does not require movement of the sample or detector during the scanning process, making it suitable for applications such as stimulation-emission fluorescent imaging (Wu & Sun, 2013a).

However, one disadvantage of area scanning is its unsuitability for moving specimens or real-time transfer analysis. Despite this limitation, area scanning remains a powerful tool for collecting spectral data with high spatial resolution and is widely used in many scientific and industrial applications (Qin, 2010).

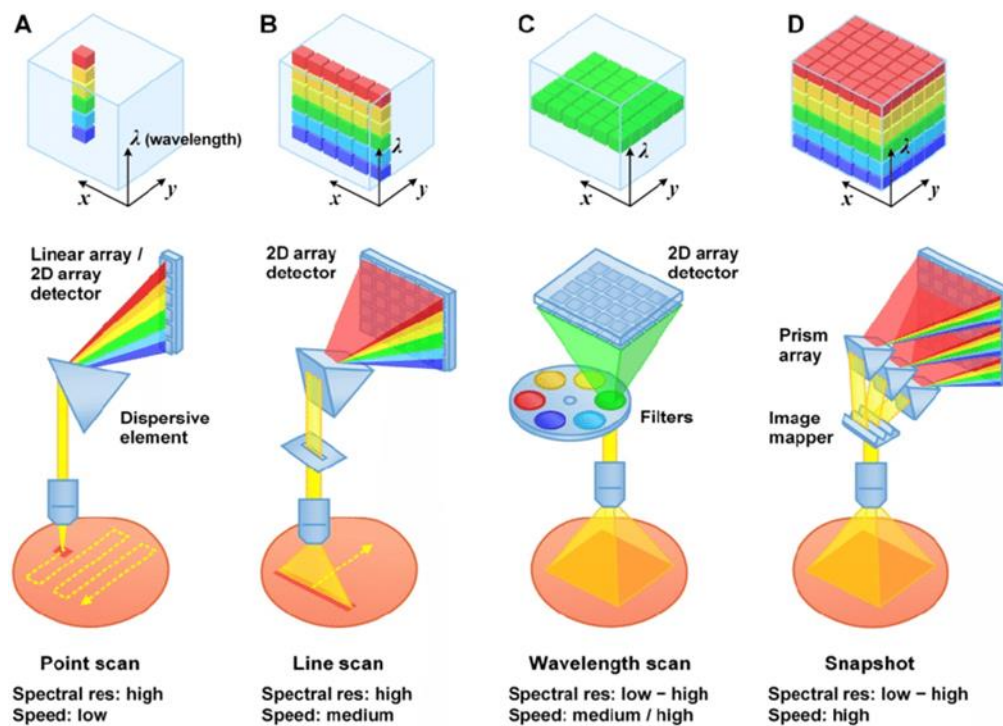


Figure 2-4 Different working principle of hyperspectral cameras, A) Point scanning, B) Line scanning, C) Area scanning, D) Snapshot (Y. W. Wang et al., 2017)

2.5.4 Snapshot Scanning

Single-shot hyperspectral imaging is an emerging technique that captures the entire hyperspectral image cube (x, y, λ) in a single exposure or acquisition (Figure 2-4 (D)). When rapid hyperspectral imaging acquisition is necessary, this technique is very efficient since it records spatial and spectral data simultaneously using a single wide-area detector. However, it has a low spatial resolution and narrow spectral intervals. (Liu et al., 2009).

Hyperspectral imaging systems are primarily utilized by large-scale geological institutions for mapping, mining, and petroleum applications. While some old forms of mapping spectroscopic and photographic data exist, narrow band collection techniques have been found to be suitable only for certain compounds. The flexibility

of hyperspectral imaging makes it a cornerstone for other measurement formats and large-scale analyses. It has proven effective in distinguishing objects such as water levels, floods, plant populations, and health indicators and serves as an excellent tool to coordinate material information with mapping data. Additionally, the food industry has greatly benefited from using this method as a scanning tool to quickly evaluate consistency, maturity, defects, or contamination from piece to piece (ElMasry et al., 2012; Wu & Sun, 2013b).

Single-shot hyperspectral imaging offers a significant advantage in reducing acquisition time and minimizing motion artifacts. Unlike scanning methods, it captures the complete spectral information of the scene simultaneously, allowing for faster and more accurate image acquisition. However, this technique requires specialized hardware such as snapshot spectral cameras to capture multiple spectral bands in a single exposure (Krupnik & Khan, 2019; Nasrabadi, 2014).

2.6 Image Acquisition Modes

Hyperspectral imaging is a technique that captures and processes images across the electromagnetic spectrum. There are three common detection modes for this technique: reflectance, transmission, and interaction (Qin et al., 2017) Each mode has a different configuration for the light source and optical detector (camera, spectrometer, and lens).

2.6.1 Reflectance Mode

Reflectance mode is used in hyperspectral cameras to collect images that represent the reflectance properties of a scene or object. The spectral radiance data collected by the camera is divided by a reference radiance standard, usually a white or gray diffuse reflectance panel (Y. Lu et al., 2020). This normalization process adjusts for variations in illumination and sensor sensitivity, allowing for more accurate

comparison of spectral data between different scenes or objects(Edelman et al., 2012; Klein et al., 2008; Qin et al., 2017).

The resulting images represent the reflectance properties of the scene or object as it is shown in Figure 2-5(a), providing valuable information about material composition and surface characteristics. Reflectance mode is commonly used in remote sensing and environmental monitoring applications to analyze vegetation health, water quality, and other environmental factors (Campbell et al., 2007).

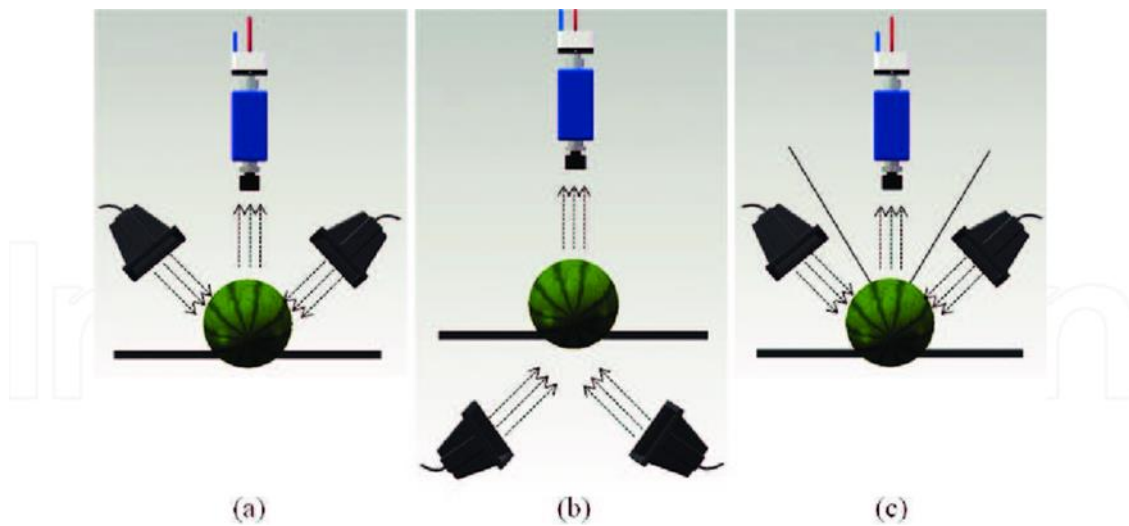


Figure 2-5 Three different modes to generate a hyperspectral image. (a) The reflectance mode. (b) The transmittance mode. (c) The interactance mode(X. Li, Li, et al., 2018)

2.6.2 Transmission Mode

Transmittance hyperspectral imaging is a form of hyperspectral imaging in which the detector is positioned opposite the light source and captures light that has passed through the sample Figure 2-5 (b). This mode is utilized to determine the internal composition of a sample, as it provides more information about the light that has interacted with the sample's internal structure (Munera et al., 2019).

Transmittance hyperspectral imaging is particularly useful for analyzing relatively transparent materials such as fish, fruits, and vegetables. By measuring the light that passes through the sample, it is possible to identify and quantify different compounds present in the sample, including water, sugar, and other nutrients (Ariana & Lu, 2008a, 2008b; Nicolai et al., 2007; Ortaç et al., 2016; H. Zhang et al., 2022).

However, transmittance hyperspectral imaging has some limitations. One major limitation is the weak signal level due to light attenuation, which can result in low-quality data. Additionally, signals obtained by transmittance hyperspectral imaging can be affected by the thickness of the sample; thicker samples can absorb more light and produce stronger signals than thinner samples (Ramer et al., 2017).

2.6.3 Interaction Mode

The light source and detector are parallel to one another and on the same side of the sample in interaction mode. This setup allows for more efficient collection of information from the sample as the light source and detector are near each other. As a result, compared to reflection mode, Interaction mode can detect more detailed information from the sample and has fewer surface effects. as it is illustrated in Figure 2-5 (c). The reduced surface effects in Interaction mode make it suitable for studying materials with complex surfaces, such as rough or uneven surfaces, which may produce multiple reflections and affect the accuracy of the data collected in Reflection mode. Additionally, Interaction mode is suitable for studying materials that have a strong surface interaction with light, as the mode can bypass the surface layer and detect deeper information (Elmasry & Petter Wold, 2008; Schaare & Fraser, 2000) .

Another advantage of Interaction mode is that it reduces the thickness effect, which is a practical advantage over the Transmittance mode. In Transmittance mode, the thickness of the sample affects the amount of light that passes through it, leading to weaker signals and reduced accuracy. Interaction mode reduces this effect, making

it a more reliable option for studying samples of varying thickness. However, it should be noted that special hardware is required in the Transmittance mode to block the direct entry of specular reflection into the detector. This is not necessary in Interaction mode, as the geometry of the setup already prevents the direct entry of specular reflection(Wu & Sun, 2013a).

Interaction mode is used in various applications, such as material identification, biomedical imaging, and remote sensing. In material identification, Interaction mode can be used to identify the chemical composition of materials, study the presence of impurities or defects, and monitor chemical reactions. In biomedical imaging, Interaction mode can be used to study the structure and composition of biological tissues and detect abnormalities. In remote sensing, Interaction mode can be used to study the composition of soil and vegetation and monitor environmental changes (Ramer et al., 2017).

2.7 Hyperspectral Data

Data captured with hyperspectral cameras are generally complex and powerful datasets, which is known as data cube or hypercubes. These three-dimensional datasets include two-dimensional spatial information with x rows and y columns, as well as spectral information composed of z wavelengths, which is presented Figure 2-6 (Manley, 2014a). In hyperspectral data, the individual unit that forms an image is referred to as a voxel, represented by $I(x, y, z)$. In contrast, for a two-dimensional image captured at a single wavelength, the image element is called a pixel (ElMasry et al., 2012; Kim et al., 2001). A hyperspectral data cube can be analyzed in various useful ways, including a single image plane of the sample or the full spectrum of a single pixel, or investigating the chemical composition of a specific point (Nasrabadi, 2014).

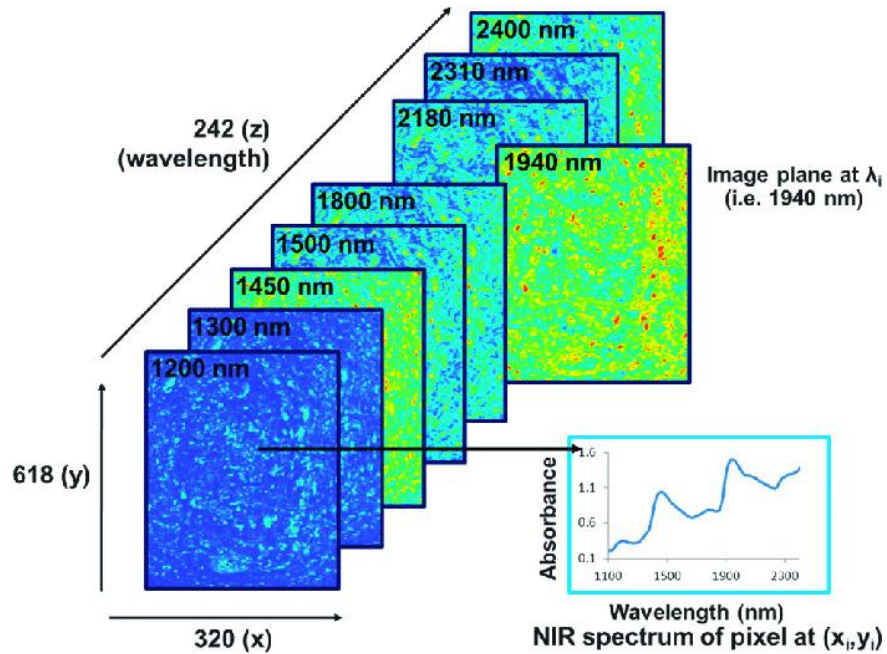


Figure 2-6 Hypercube data for different wavelnghtes (z) in vaarious spatial (x, y) domains (Manley, 2014b)

2.8 Pre-Processing Of Hyperspectral Data

Preprocessing is a crucial step in the analysis of hyperspectral images. These images contain large amounts of data, with each pixel having a whole spectrum associated with it (Pizarro et al., 2004). This results in a highly correlated data set, which can make it challenging to extract meaningful and necessary information. Preprocessing techniques such as noise reduction, distortion correction, and spectral and spatial enhancement are necessary to improve the accuracy and quality of the data, making it easier to analyze and interpret (Wold et al., 1998). Principal Component Analysis and Multivariate Curve Resolution, two classical multivariate data analysis

techniques, have been used to the analysis of hyperspectral data cubes, demonstrating their great usability and ability to successfully extract the needed data. Preprocessing is, therefore, an essential step in making hyperspectral images useful for a variety of applications, including remote sensing, environmental monitoring, and medical imaging (Amigo et al., 2013; Rinnan et al., 2009; Vidal & Amigo, 2012).

The ability to identify and remove trends, outliers, and noise from hyperspectral data is just one benefit of preprocessing the data. It increases data interpretation, the effectiveness of qualitative and quantitative studies, and simplifies machine learning procedures. Preprocessing methods are crucial when working with hyperspectral data, as they play a significant role in determining the quality and reliability of the models developed. Proper preprocessing techniques help in extracting relevant information, reducing unwanted data, and improving the overall accuracy and effectiveness of subsequent data analysis and modeling tasks (Chein-I Chang, 2003; Luypaert et al., 2004; Yao & D Lewis, 2010).

In hyperspectral spectroscopy (in both reflectance and transmittance modes), preprocessing techniques can be divided into three categories: smoothing or denoising, scattering correction methods, and spectral normalizations, which are the most used techniques (Amigo et al., 2013)

2.8.1 Smoothing

Smoothing methods play a crucial role in preprocessing spectral data by reducing the impact of noise, errors, and unwanted variations. Their purpose is to obtain a more accurate and visually appealing representation of the underlying spectral characteristics (Dai et al., 2014; Luypaert et al., 2004). Various smoothing techniques exist, each employing different mathematical algorithms and assumptions about the data (Luypaert et al., 2004; Vaiphasa, 2006). Common methods include moving average, Savitzky-Golay, Gaussian smoothing, and median filtering. Among these, the Savitzky-Golay method stands out as a popular choice. It involves

selecting a subwindow around a specific data point and projecting it onto a polynomial fit of the points within the subwindow. The method is relatively simple to implement but requires careful consideration when choosing the size of the spectral subwindow. Larger subwindows may eliminate informative peaks, while smaller windows may introduce more noise into the smoothed data. The Savitzky-Golay method, in particular, is widely used due to its effectiveness in reducing instrumental noise (Amigo & Santos, 2019; Ruffin et al., 2013; J. Sun et al., 2021).

2.8.2 Multiplicative Scatter Correction

The MSC (Multiplicative Scatter Correction) method is a popular preprocessing technique in NIR spectroscopy. It adjusts for the impact of additional and multiplied changes in the spectral data (Sonobe et al., 2020). MSC operates at the row level, removing physical factors like particle size and surface variations that do not carry relevant chemical or physical information (Sonobe et al., 2020; Xu et al., 2020). It assumes that each spectrum is influenced by both sample characteristics and particle size, represented as baseline variation and trend using a reference spectrum (L. J. Chen et al., 2010). MSC corrects baseline and trend differences, producing transformed spectra similar to the originals for easier interpretation. However, applying MSC to the same spectrum with different datasets can yield different results due to the incorporation of population descriptive values (Windig et al., 2008). Even commonly used software may give varied MSC outcomes without considering the specific MSC model for a dataset. MSC includes two steps:

1. The process involves determining the values of the correction coefficients for both the additive and multiplicative contributions.

$$x_{org} = b_0 + b_{ref,1} x_{ref} + e \quad \text{Equation 2-1}$$

2. The recorded spectrum is adjusted or corrected using the obtained correction coefficients.

$$x_{corr} = \frac{x_{org} - b_0}{b_{ref,1}} = x_{ref} + \frac{e}{b_{ref,1}} \quad \text{Equation 2-2}$$

The recorded spectrum (x_{org}) of an individual sample obtained from the NIR instrument is corrected. This correction involves utilizing a reference spectrum (x_{ref}) and accounting for the un-modeled portion (e) of the original spectrum (Equation 2-1). The result of the correction process is the corrected spectrum (x_{corr}). The correction coefficients, represented by scalar parameters b_0 and $b_{ref,1}$, vary for each sample and play a significant role in the correction procedure (Equation 2-2). In summary, by considering the reference spectrum and accounting for the un-modeled portion, the recorded spectrum is transformed into the corrected spectrum using specific scalar parameters for each sample (Maleki et al., 2007; Witteveen et al., 2022).

2.8.3 Standard Normal Variate (SNV)

The Standard Normal Variate (SNV) preprocessing method is widely employed in hyperspectral data analysis to normalize spectral data and address baseline variations without distorting the shape of the spectra. SNV operates by subtracting the mean and dividing by the standard deviation of each wavelength in each spectrum. By normalizing the data to have a zero mean and unit variance, SNV effectively removes the influence of solid particle size, surface scattering, and optical path changes on NIR diffuse reflection spectra. It is particularly useful when the spectral region is less dependent on chemical information, allowing for more accurate analysis of underlying spectral features (Cozzolino et al., 2023; Wadoux et al., 2021).

SNV is an unsupervised technique, meaning it does not require a response variable during preprocessing, making it versatile for various applications. It is often combined with other preprocessing techniques to enhance the overall data analysis process (Xu et al., 2020). SNV preprocessing is recognized as one of the most commonly applied methods for scatter correction in NIR/NIT data analysis. By

performing row-wise normalization, SNV addresses the row-dependent effects within the spectral matrix. The method corrects for single light scattering and is also referred to as z-transformation or centering and scaling (Bian, 2022).

$$x_{i,SNV} = \left(\frac{x_i - \bar{x}_i}{s_i} \right) \quad \text{Equation 2-3}$$

To perform this correction according to Equation 2-3, the average of each spectrum, \bar{x}_i is subtracted from the entire spectrum, x_i , and these centered values are divided by the standard deviation s_i .

2.8.4 Derivatives

Derivatives play a crucial role in hyperspectral imaging as a preprocessing method for baseline correction and resolution enhancement. They have been widely employed in analytical spectroscopy for several decades. Derivatives offer the capability to remove both additive and multiplicative effects in spectra, making them valuable tools in spectral analysis (Tsai et al., 1998; D. Zhang & Zhang F, 2014). There are two common methods for deriving spectra: direct differences (Norris method) and Savitzky-Golay (S-G) derivative methods. The second derivative is produced by computing the difference between two successive points in the first-order derivative spectra, whereas the first derivative is estimated using the direct differences approach by computing the difference between two distinct spectral measurement points.

Derivation is beneficial in separating overlapping peaks and correcting baseline shifts. However, a potential drawback of deriving spectra is the amplification of noise. To mitigate this issue, smoothing techniques are often employed (Amigo & Santos, 2019; Cozzolino et al., 2023).

The Savitzky-Golay algorithm, which utilizes a moving window averaging method, is commonly used for spectral smoothing. This involves selecting a window size and fitting the data within the window with a polynomial. The central point in the window is then replaced by the value of the polynomial. In hyperspectral imaging, a window size of seven points is typically used for the first derivative and 15 points for the second derivative (Xu et al., 2020). By applying derivation preprocessing in hyperspectral imaging, baseline correction is achieved, allowing for more accurate analysis of spectral features.

2.9 Cement Compounds

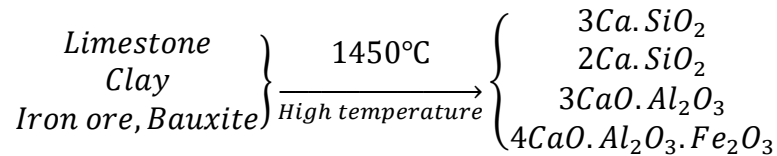
Portland cement is defined by ASTM C 150 as a type of hydraulic cement that is made by grinding clinkers which primarily consist of hydraulic calcium silicates and a small quantity of one or more forms of calcium sulfate that are added during intergrinding. These clinkers are small, round nodules that range in diameter from 5 to 25 millimeters and are created by heating a pre-determined mixture of raw materials to high temperatures until they sinter into a solid material (ASTM C150-07, 2012)

2.9.1 Manufacturing Process

Portland cement is a hydraulic cement that is widely used in the construction industry, which is primarily composed of calcium silicates and calcium aluminates (Bye, 1999; Halstead, 1961). The manufacturing process involves grinding the raw materials, mixing them in predetermined proportions, and burning the mixture in a rotary kiln at a temperature of about 1400°C (2550°F) (Taylor, 1997). Calcareous materials like chalk or limestone, as well as silica and alumina, which are found in clay or shale, are utilized as raw materials to make portland cement. The raw compounds are crushed into a fine powder, which is then combined in proper proportions. The material is subsequently burned in a rotating kiln, where it partially

fuses and sinters to form clinker. The commercial portland cement, which is used all over the world, is created by cooling the clinker and then grinding it into a fine powder with some gypsum (Chatterjee, 2018). Clays and shales, rather than quartz, are preferred as sources of additional silica in the raw mix because quartzic silica does not react easily with lime (Ghosh, 2014).

Alkalies, iron, magnesium ions, and aluminum all contribute to the raw mixture's ability to create calcium silicate at much lower temperatures than normally achievable. Because of this, when sufficient amounts of the iron and alumina minerals are not available in the main raw materials, they are consciously added to the raw mixture by adding secondary elements like bauxite and iron ore. Therefore, in addition to calcium silicate compounds, Portland cement clinker also includes aluminates and calcium aluminoferrites. (Kumar Mehta & M Monteiro, 2014; Neville & Brooks, 1987; Tokyay, 2016).



The primary compounds of ordinary portland cement are four major compounds: C₃S (tricalcium silicate), C₂S (dicalcium silicate), C₃A (tricalcium aluminate), and C₄AF (tetracalcium aluminoferrite). These compounds are also known as alite, belite, celite, and ferrite, respectively. Portland cement is predominantly composed of the two calcium silicates, C₃S and C₂S, which make up around 68-75% of its total composition. This is because the main compounds of portland cement are calcium silicates. Specifically, portland cement is a substance that contains CaO and SiO₂ in a ratio that enables the resulting calcium silicate to react with water under normal conditions of temperature and pressure (Shetty & Jain, 2019).

2.9.2 Hydration of Portland Cement

When anhydrous portland cement (PC) is mixed with water, a chemical reaction called hydration occurs, resulting in the formation of hydrates that possess setting and hardening characteristics. The hydration of PC is a complex process that involves numerous simultaneous and successive reactions, and it is necessary to consider the individual hydrations of the major compounds. The constituents of PC undergo a series of chemical reactions when mixed with water, and the four major clinker compounds, as well as free calcium oxide, calcium sulfate, and sodium and potassium sulfates, all participate in the hydration process (Choo & Newman, 2003).

The hydration of cement is not fully understood, but studying the reaction mechanism of individual compounds separately can help understand the chemistry of hydration (Taylor, 1963). The properties of fresh concrete, such as setting and hardening, are the direct results of hydration, while the properties of hardened concrete are also influenced by the process of hydration. Therefore, some knowledge of the chemistry of hydration is necessary to understand the properties and behavior of cement and concrete (Taylor, 1963).

2.9.2.1 Hydration Of Calcium Silicates

The two primary cementitious compounds in cement are the calcium silicates C_3S and C_2S . When these compounds react with water, they produce an amorphous calcium silicate hydrate known as C-S-H gel, which serves as the main binder that stick the aggregate particles and sand together in concrete (Birchall et al., 1978).

C_3S is much more reactive than C_2S , with approximately half of the C_3S present in a typical cement being hydrated within three days and 80% being hydrated within 28 days. C_2S , on the other hand, does not typically undergo significant hydration until around 14 days (Kumar Mehta & M Monteiro, 2014).

Both C_3S and C_2S produce C-S-H gel with an average Ca to Si ratio of about 1.7. This is significantly less than the 3:1 ratio in C_3S , and the extra calcium accumulates as calcium hydroxide (CH) crystals. C_2S hydration also results in some CH formation. The hydration of C_3S as well results in some lime breaking out as crystalline $Ca(OH)_2$; C_2S exhibits a similar behavior but includes less lime (Double et al., 1978).

One important characteristic of C_3S hydration is the presence of an initial dormant or induction period after the first mixing, during which the reaction appears to be suspended. This allows for the placement and compaction of concrete before setting and hardening begin. When the protective coating of C-S-H on the surface of the C_3S is lost or becomes more permeable due to ageing or a structural change, the dormant phase is over. The amount of time it takes for the major C-S-H product to form after water has access to the C_3S crystals again could also hinder the reaction. (Mindess et al., 2003).

It should be emphasized that PC is a multi-compound system, and that the hydration reaction is a relatively intricate process involving a number of simultaneous and subsequent reactions. While each compound hydrates on its own, the interactions of the compounds with each other and with other cement phases have an impact on the mechanism and kinetics of hydration. The aluminates, which make up the remaining 25% of ordinary portland cement, also play a significant role in determining the hardening characteristics (Bullard et al., 2011).

2.9.2.2 Hydration of Calcium Aluminates

The hydration of aluminates in cement is a complex process that is influenced by various factors, such as the presence of other components, the availability of water, and the particle size of the cement. The two primary aluminates present in cement are C_3A and C_4AF , and their hydration behavior is of great importance in the

production of high-quality cementitious materials (Scrivener et al., 2019; Taylor, 1963).

When C_3A is mixed with water in the presence of gypsum, it initially reacts to form calcium sulfoaluminate hydrate, which is commonly known as ettringite. Ettringite acts as a diffusion barrier around C_3A , slowing down its hydration and preventing flash setting (Joseph et al., 2019). Ettringite is also aggressive and can break down other hydration products, leading to volume instability and the creation of cracks in the concrete. If ettringite is formed before the concrete has hardened, it can contribute to early strength development by reinforcing the surrounding C-S-H. However, if ettringite is formed after the concrete has hardened, it can weaken the concrete by creating cracks and volume instability (Choo & Newman, 2003; Neville & Brooks, 1987).

When enough calcium sulfate is not present in the medium, rapidly reacting C_3A produces the phases C_2AH_8 and C_4AH_{19} , which then change into C_2AH_6 . This is a rapid and highly exothermic reaction. The first reactions are regulated when finely crushed gypsum or hemihydrate is combined with C_3A prior to mixing with water. This is because ettringite forms a protective layer on the crystals' surface (Pourchet et al., 2009).

The majority of commercial portland cements do not contain enough sulphate to support the formation of ettringite. Ettringite interacts with C_3A to produce monosulfate, a phase with a reduced SO_3 concentration that forms once the available sulphate has been consumed (Jia, 2010; Pourchet et al., 2009).

C_4AF hydrates similarly to C_3A , however it happens so more gradually. In the crystal structures of ettringite and monosulfate, iron replaces aluminum in solid solution. Aluminum-ferrite trisulfate (Af_t) hydrate and aluminum-ferrite monosulfate hydrate (AF_m) phases, which are generated by combining C_3A and C_4AF , have varying compositions of ettringite and monosulfate, respectively. (Z. Li et al., 2022; Mindess et al., 2003; Saikia et al., 2012).

2.9.3 Synthesis of Pure C₃S

In cement clinker, C₃S is generally impure and referred to as alite. The impurities have a strong effect on the polymorphs that can be obtained. The most common impurities found in cement clinker are Mg²⁺, Al³⁺, and Fe³⁺, with the M₁ or M₃ monoclinic polymorphs typically dominant. In a study conducted by Quennoz (2011), a synthesis of alite was made using a 3:1 molar ratio of calcium carbonate (CaCO₃) and silicon dioxide (SiO₂), with 1% by weight of aluminum oxide (Al₂O₃) and 2% by weight of magnesium oxide (MgO) (Quennoz, 2011).

The raw materials were mixed in the ratios given in Table 2-1, with 1 liter of pure water in a ball mill for 24 hours. Subsequently, the mixture was dried at 100°C for 24 hours and ground to a powder using a mortar and pestle. The obtained powder was pressed into pellets with a diameter of 5 cm and a height of 1 cm under a pressure of 100 kP/cm², and the pellets were burned in an electric furnace according to the firing procedure shown in Figure 2-7

Table 2-1 Weight of raw materials are used for synthesizing C₃S (Quennoz, 2011)

Raw materials	Weight (g)
CaCO ₃	635.8
SiO ₂	130
Al ₂ O ₃	5.1
MgO	10.3

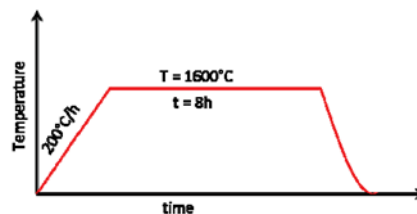


Figure 2-7 Firing procedure of C₃S according to (Quennoz, 2011)

After the burning process, the pellets were rapidly cooled with air, then ground and sieved in a ring mill ($<100\mu\text{m}$). The use of Al and Mg ratios results in the M3 polymorph. The Al and Mg ions affect the grain growth of C_3S . The Mg ions increase the amount of liquid phase during the burning process and decrease the viscosity of the mixture, allowing better diffusion of chemical species and leading to the formation of larger grains compared to pure C_3S . The synthesized phase was analyzed using X-ray diffraction (XRD) and scanning electron microscopy (SEM) and the results are depicted Figure 2-8. According to the results of the Rietveld analysis, the synthesized alite compound contains 0.72% free CaO.

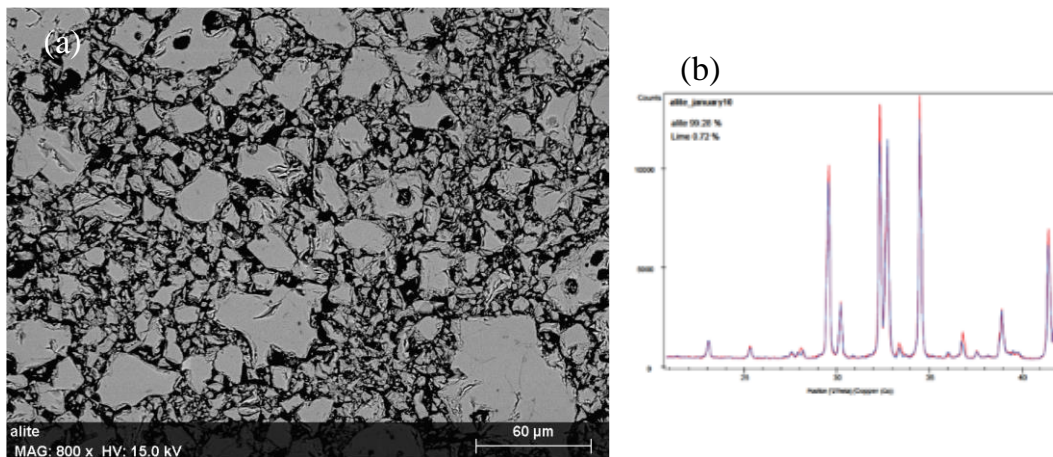


Figure 2-8 Results of (a) SEM, (b) XRD for C_3S (Quennoz, 2011)

In another article, the impact of CaCO_3 on the hydration products of C_3A , C_3S , and portland cement is explored by utilizing techniques such as XRD, SEM, and TG-DTA for analysis. In this article authors synthesized C_3S using a mixture containing 71.9% CaO, 0.6% Al_2O_3 , 25.7% SiO_2 , and 1.8% MgO, which was heated at 1600°C for 16 hours. To obtain a product similar to alite found in clinker, Al and Mg oxides were added to the C_3S raw mixture, with these compounds supporting C_3S formation

at lower temperatures. The cooling process was not reported, and the samples were ground to a size of less than 90 μm after burning. The results revealed that CaCO_3 sped up the hydration of C_3S and the formation of ettringite, while suppressing the creation of monosulfate. The presence of CaCO_3 also decreased the amount of calcium hydroxide in the hydration products of C_3S and portland cement. In contrast, CaCO_3 had little effect on the hydration of C_3A . The study highlighted the complex interactions between cement compounds and external factors influencing the hydration products (Kakali et al., 2000).

In the study conducted by Wesselsky and Jensen, a method for synthesizing both triclinic and monoclinic forms of C_3S was described (Wesselsky & Jensen, 2009). It was noted that the same conditions were used for both forms, but the composition of the raw material mixture was different. In both cases, the $\text{CaO}:\text{SiO}_2$ stoichiometric ratio was 3:1. However, for the monoclinic form, a small amount of MgO and Al_2O_3 was added to the raw material mixture to stabilize this crystal structure. Magnesium atoms replace calcium in the structure, while aluminum replaces both calcium and silicon atoms in equal proportions. In the case of monoclinic C_3S , the given amounts correspond to a weight percentage of 98.2% stoichiometric CaO and SiO_2 mixture, 1.1% MgO , and 0.7% Al_2O_3 (Table 2-2). The sintering procedure involved heating to 1600°C in 2 hours, holding at this temperature for 2 hours, and then rapidly cooling. The effect of the sintering cycle on the synthesized triclinic C_3S was determined by X-ray diffraction (XRD) analysis. The results of XRD analysis after the first and second sintering cycles are shown in Figure 2-9. It was estimated that the C_3S content was 90% after the first cycle. The peak indicated by the arrow was identified as the CaO main peak, and it was noted that all other visible peaks belonged to triclinic C_3S . After the second cycle, the CaO main peak disappeared, indicating a purity of approximately 98-99%.

Table 2-2 Mix composition for 100 g of final C₃S product (Wesselsky & Jensen, 2009)

	CaCO ₃	SiO ₂	Al ₂ O ₃	MgO
C ₃ S triclinic	131.506 Ca/Si = 3.000	26.316	0	0
C ₃ S Monoclinic	127.614 Ca/Si = 2.964	25.843	0.701 Al/Si = 0.302	1.177 Mg/Si

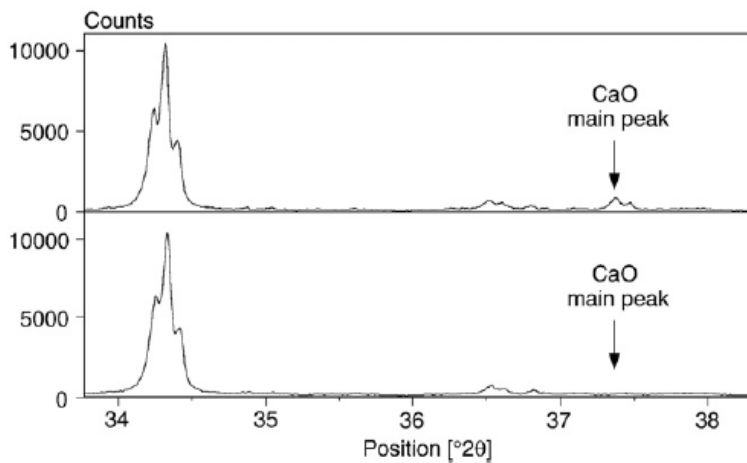


Figure 2-9 XRD results of triclinic C₃S

The article "The Effect of Magnesium and Zinc Ions on the Hydration Kinetics of C₃S" focuses on the effect of magnesium and zinc ions on the hydration rates of C₃S, the primary compound of portland cement (Bazzoni et al., 2014). Using isothermal calorimetry and X-ray diffraction, the authors analyze the hydration products and kinetics of C₃S in the presence of various concentrations of Mg and Zn ions. The findings reveal that both Mg and Zn ions can accelerate the early-stage hydration of C₃S, with Mg having a more significant effect than Zn. However, as hydration

progresses, the presence of Mg ions leads to a decrease in the total heat release and a delay in the formation of hydration products, while the presence of Zn ions has no significant effect on the hydration kinetics. The authors attribute the observed effects to the interaction between the ions and the C₃S surface, which can affect the availability of water and the formation of the hydration products.

The study also shows that there is no evident link between reactivity and crystal structure polymorphs. The alite with magnesium is monoclinic, the alite with zinc is discovered to be triclinic, and the pure C₃S displays triclinic space group symmetry. However, Zinc uptake improves the reactivity of C₃S while preserving a similar triclinic symmetry to pure C₃S, whereas Mg inclusion results in a distinct polymorph with a nearly identical reactivity. Nevertheless, it cannot be excluded that the levels of disorder in the structure of the different triclinic polymorphs may influence the reactivity. The major peak of hydration is affected by both zinc and magnesium, although in two different ways, according to the results of the calorimetry. Magnesium produces a wider peak, while zinc produces a higher peak. Due to the presence of ions in solution, these two behaviors appear to be connected to the modification of C-S-H's nucleation and growth. (Bazzoni et al., 2014).

Li, et al. found that using amorphous silica as a raw material and inter-grinding it with CaCO₃ and water significantly enhanced the efficiency of C₃S synthesis. The dried raw mixture had enough green strength to be self-supporting, which allowed for large cylinders to be placed in platinum crucibles. With this method, it was estimated that a production capacity of approximately 2 kg of C₃S within a week was possible (X. Li, Ouzia, et al., 2018).

Amorphous silica and extremely fine CaCO₃ particles in the raw mix after grinding contributed to the raw mix's better burnability, which raised the effectiveness of the C₃S synthesis. Additionally, the streamlined procedure for creating samples, which avoided pressing discs, saved time and effort. Lastly, the increased capabilities of the furnace and crucible allowed for larger cylinders to be sintered. The researchers used X-ray powder diffraction with Rietveld analysis to quantify the mineral

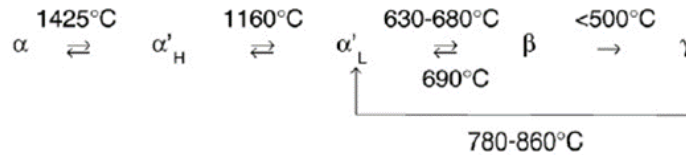
composition of the sintered sample. They proposed a five-step solid-state reaction-based procedure for C_3S /alite synthesis but listed several disadvantages of this procedure, such as the time-consuming pressing of the raw mixture into discs, long sintering times, the need for repeated sintering, and the furnace and platinum crucible's constrained capacity (X. Li, Ouzia, et al., 2018).

To overcome these issues, the authors suggested an alternative method that avoids pressing the raw mixture into discs and allows for a production capacity of approximately 2 kg of C_3S within a week. They used calcium carbonate (VWR) and two types of amorphous silica (fumed silica, Sigma-Aldrich) with different particle size distributions as the raw materials. The final product contains 96-98% C_3S by weight and <0.4% free CaO. The authors also provided a summary of the mineral composition of the test samples using Rietveld analysis. The porous structure of the dried cylinder sample allowed for easier grinding and the release of CO_2 during the decomposition of $CaCO_3$. In summary, the authors made three main changes to the production process: using cylinders instead of pressed discs for the raw mixture, shortening the sintering time by increasing the burnability of the raw mix, and increasing the capacity of the Pt crucible and furnace by using cylinders instead of discs (X. Li, Ouzia, et al., 2018).

2.9.4 Synthesis of Pure C_2S

C_2S is the second most abundant compound present in cement. The mineral compound C_2S is a stable phase at room temperature and can undergo multiple phase transitions at temperatures up to 2130°C (Maheswaran et al., 2015). The β - C_2S modification is typically found in industrial clinkers, while α or α' modifications are present during sintering but transform into the β phase upon cooling. The β - γ transformation is undesirable as it destroys clinker nodule integrity and reduces reactivity with water. α' - C_2S , which is more reactive than β - C_2S , is not normally present in Portland cements but is of interest to manufacturers of "Belite cement." C_2S can incorporate foreign ions, such as Al^{3+} and Fe^{3+} , up to 4-6 wt.%, and good

miscibility with P_2O_5 and B_2O_3 has been observed. Synthesis of C_2S can be achieved through the sol-gel method using calcium nitrate and silicon oxide as initiating materials (Y. L. Chen et al., 2009).



X-ray diffraction (XRD) can be used to identify β - C_2S , but matching α' - C_2S is more challenging as there is no single and specific pattern covering all encountered peaks. Therefore, other potential phases and modifications must be eliminated, by attempting to match their corresponding patterns. In addition to the solid-state sintering method, the Pechini procedure, which uses appropriate oxides or salts with an alpha-hydroxycarboxylic acid in a solution, can successfully synthesize C_2S . This method involves chelation and results in stable α' - C_2S , which has higher reactivity than β - C_2S .

In an article by Zhao, the authors discuss the crystal transformation of dicalcium silicate (C_2S) and its influence on the microstructure, hydraulicity, and grindability of cement clinker, (Zhao, 2012). The transformation of β - C_2S to γ - C_2S can be used to pulverize cement clinkers for saving grinding energy, but the hydraulicity of γ - C_2S is lower than β - C_2S . The study investigated the influences of sintering temperatures, cooling methods, and chemical impurities on transformation. The findings highlight that the crystal transformation ratio of C_2S is inversely related to the cooling rate. Faster cooling speeds hinder the transformation of β - C_2S to γ - C_2S according to the results shown in Figure 2-10. Therefore, to produce clinkers with a high content of β - C_2S , it is essential to rapidly cool the clinker, and the cooling rate should not be lower than $500^\circ C$ per minute.

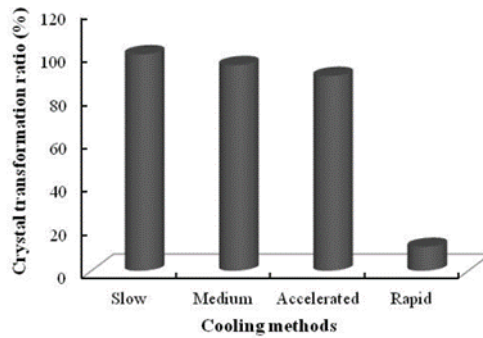


Figure 2-10 The crystal transformation rate of β -C₂S to γ -C₂S with different cooling methods (Zhao, 2012)

Chemical impurities (Na₂O, P₂O₅, B₂O₃, Cr₂O₃, and K₂O) were found to be stabilizers of β -C₂S, and their concentration was related to the stability effect. The characteristic concentrations of Na₂O, P₂O₅, B₂O₃, Cr₂O₃, and K₂O were approximately 1.2%, 0.3%, 0.3%, 1.0%, and 1.5%, respectively. The study also examined the effect of cooling methods on C₂S crystal transformations and found that a high cooling rate prevented β -C₂S from transforming into γ -C₂S. A proper selection of sintering temperatures and cooling rates in combination with stabilizer concentrations could quantitatively control C₂S crystal transformation. The raw materials used for the synthesis of C₂S were CaCO₃ and SiO₂, while Na₂O, P₂O₅, B₂O₃, Cr₂O₃, and K₂O chemicals were used for the stabilization of β -C₂S (Zhao, 2012).

One other article, (Singh, 2006), discusses the hydrothermal synthesis of β -dicalcium silicate (β -C₂S) using different sources of silica and calcium oxide. The study compares the reactivity and hydration properties of the β -dicalcium silicates obtained through hydrothermal synthesis with those obtained through a conventional method using B₂O₃ as a stabilizer. The hydrothermal method resulted in a highly reactive β -C₂S, even when low-cost sources of silica, such as rice husk ash and fly ash, were used. The high reactivity was attributed to the high specific surface area of β -C₂S, resulting in the formation of nano-size C-S-H with a porous structure that did not hinder the approach of water molecules to the fresh surface of β -C₂S.

The authors prepared the reacting systems by mixing stoichiometric ratios of CaO and silica from different sources, followed by adding water and keeping the mixtures in an autoclave at high temperatures and pressures. The hydrated masses were then characterized using X-ray diffraction, DSC, and SEM techniques. The results showed that β -C₂S obtained through the hydrothermal method had much higher extents of hydration compared to those obtained through the conventional method. Moreover, the hydrothermal method resulted in the formation of β -C₂S with low free lime values, indicating high reactivity. The study provides insights into the effect of synthesis methods and source materials on the properties of β -C₂S, which can be useful for designing new materials with desired properties. In conclusion, the hydrothermal synthesis of β -C₂S using low-cost sources of silica was found to be highly effective in producing a reactive material with high extents of hydration (Singh, 2006).

2.9.5 Synthesis of Pure C₃A

Tricalcium aluminate (C₃A) is a vital constituent of ordinary portland cement (OPC) clinkers, albeit in relatively small proportions (2-10% by weight). Its pronounced influence on cement setting and control over early-age heat release stems from its high reactivity. Uncontrolled reaction of C₃A with water can result in rapid setting, commonly known as flash set. Therefore, comprehending and effectively managing the reactivity of C₃A in cement formulations is of utmost importance (Y. L. Chen et al., 2009).

The structure of C₃A can be modified by the presence of minor elements like Na⁺, K⁺, Mg²⁺, and Fe³⁺ during the clinkering process. Additionally, the alkali content, predominantly Na⁺ originating from raw materials and fuels during clinkering, impacts the behavior of C₃A, leading to the formation of diverse C₃A polymorphs (Rheinheimer et al., 2016).

During the initial stages of cement hydration, C_3A exerts a substantial influence on cement setting and hardening characteristics. Through ionic substitution, the crystal structure and other properties of C_3A can be altered. Consequently, understanding the role and behavior of C_3A when formulating and utilizing cement becomes paramount. By effectively managing the reactivity and structure of C_3A , researchers and engineers can manipulate the setting time and overall performance of cement, ensuring its suitability for a wide array of applications in construction and infrastructure development (Pourchet et al., 2009).

Despite the apparent simplicity in the synthesis of C_3A , it is accompanied by certain complexities. The phase transition behavior of the $CaO-Al_2O_3$ binary system is depicted Figure 2-11, illustrating the influence of raw material compositions and temperature. Notably, C_3A undergoes melting at a temperature of $1542^\circ C$. In its pure form, C_3A commonly adopts a cubic crystalline structure (Wesselsky & Jensen, 2009).

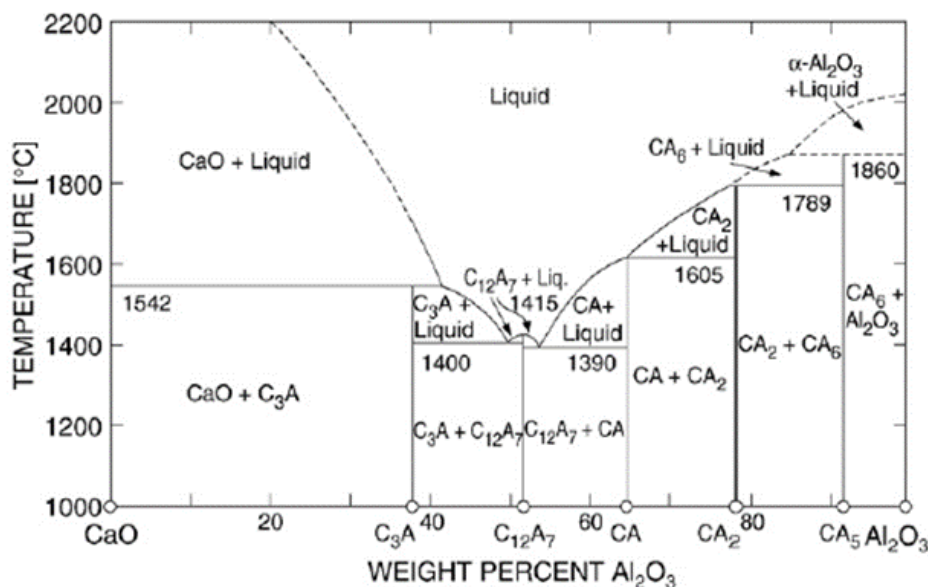


Figure 2-11 phase transition behavior of the $CaO-Al_2O_3$ binary (Wesselsky & Jensen, 2009)

In a study conducted by Quennoz and Scrivener, the hydration behavior of C_3A -gypsum systems with varying gypsum additions, focusing particularly on the second

steps of the reaction following gypsum depletion was investigated (Quennoz & Scrivener, 2012). The objective of this study was to specifically synthesize cubic C_3A . The author acknowledged the challenges associated with achieving pure C_3A synthesis and implemented modifications to the synthesis procedure following multiple unsuccessful attempts. The primary method employed for C_3A synthesis involved the mixing of CaO (derived from $CaCO_3$) and Al_2O_3 in stoichiometric proportions (3:1). Subsequently, XRD analyses were carried out on exemplary specimens from each batch. It was observed that certain batches exhibited the presence of a mayenite ($C_{12}A_7$) peak at approximately $18^\circ C$. This particular phase, depicted in Figure 2-11, denoted a transitional stage during the synthesis of C_3A . Nonetheless, the presence of the mayenite phase was deemed unfavorable due to its significant influence on modifying the reaction kinetics of the C_3A -gypsum system and inducing rapid setting .

One other study (Tian et al., 2016) about the formation of aluminates focuses on the synthesis of sintering procedure for calcium aluminate compounds at a temperature range of $1100-1400^\circ C$. The synthesized compounds had been characterized by various analytical techniques such as XRD, FT-IR, SEM, EDS, and DSC. The results reveal the presence of several calcium aluminate compounds, including $Ca_3Al_2O_6$, $Ca_5Al_6O_{14}$, $Ca_{12}Al_{14}O_{33}$, $CaAl_2O_4$, $CaAl_4O_7$, and $CaAl_{12}O_{19}$, in the sintered products with varying molar ratios of CaO to Al_2O_3 . These compounds exhibit a layered distribution, with the outer layer containing higher amounts of CaO and the core primarily composed of Al_2O_3 . The initial reaction stage involves the formation of $Ca_3Al_2O_6$ and $Ca_5Al_6O_{14}$, where CaO gradually diffuses into the distribution of Al_2O_3 . The molar ratios of the equilibrium phases align closely with those of the sintered products. Furthermore, the unit cell volumes of certain calcium aluminate compounds, such as $Ca_3Al_2O_6$, $CaAl_2O_4$, and mayenite, decrease as the sintering process progresses.

In the early stages of the high-temperature solid-state reactions, the formation of calcium aluminate compounds C_5A_3 and C_3A is observed, which remains unaffected by the varying ratios of CaO to Al_2O_3 in the mixtures. As the consumption of Al_2O_3

and CaO occurs, the content of the equilibrium phase increases at the expense of other calcium aluminate compounds. These include CA_2 , CA, $C_{12}A_7$, C_5A_3 , and C_3A , which all act as intermediate phases leading to the formation of the equilibrium phases. The molar ratios of the equilibrium phases closely resemble those observed in the sintered products.

The initial reaction stage also involves the formation of mayenite, with a chemical formula of $Ca_{11.3}Al_{14}O_{32}$, which gradually transforms into $Ca_{12}Al_{14}O_{33}$ with increasing sintering duration. Additionally, the unit cell volumes of C_3A , $C_{12}A_7$, and CA initially exceed standard values but gradually decrease as the sintering process proceeds. The distribution characteristics of calcium aluminate compounds reveal a core region primarily composed of Al_2O_3 , surrounded by layers of CA_2 and CA. C_3A and $C_{12}A_7$ are detected in the layer closest to the surface, and as the reactions proceed, CaO diffuses into the region where Al_2O_3 is distributed. (Tian et al., 2016)

2.10 Characterization of Materials by Hyperspectral Imaging

While hyperspectral imaging is a relatively recent addition to the array of material recognition techniques, there have been limited studies utilizing this method to differentiate between construction materials.

In one of the recent studies (Bonifazi et al., 2018), the authors focus on the quality assessment of recycled concrete aggregates (RCA), particularly in terms of evaluating the presence of attached mortar paste on their surfaces. To achieve this goal, an innovative sensor-based quality control strategy using hyperspectral imaging in the near-infrared range (1000–1700 nm) is developed by the authors. The HSI data is processed, employing principal component analysis (PCA) for data exploration and, subsequently, partial least square-discriminant analysis (PLS-DA) is utilized to construct classification models that can detect the presence of mortar paste on aggregate surfaces and quantify its percentage as it is illustrated in Figure

2-12. Micro X-ray fluorescence (micro-XRF) maps are also used to validate the HSI classification results. The authors demonstrate that their approach is effective in identifying and quantifying the mortar attached to the aggregate surface, providing an objective, fast, non-destructive, and cost-effective method for assessing the quality of recycled aggregates. They suggest that this methodology could be implemented at a recycling plant scale to improve the competitiveness of recycled aggregates in the market compared to the natural ones.

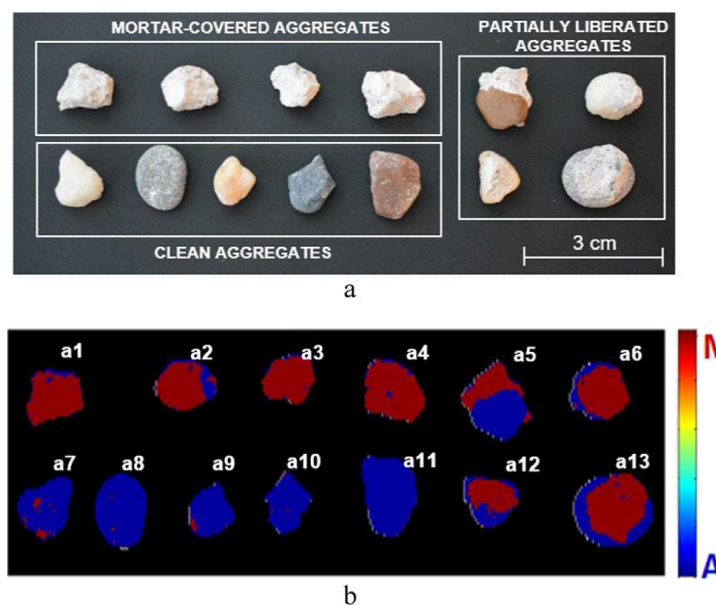


Figure 2-12 The source image (a) comprises clean aggregates, mortar-covered aggregates, and partially liberated aggregates, while the corresponding prediction image (b) results from the application of PLS-DA, illustrating the classification into aggregates (A) and mortar (M), along with the micro-XRF map (Bonifazi et al., 2018)

In another study, the authors have conducted a research using hyperspectral imagery and computational algorithms to classify different types of mortar and assess the in-situ strength of fresh mortar in near real-time (Fan et al., 2020). They collected reflectance data from mortar surfaces over a range of 400–2500 nm. Three groups of mortar samples with varying water-to-cement (W/C) ratios were prepared and

scanned from Day 1 to Day 14 of curing. They specifically focused on the reflectance data in the wavelength range of 1920 nm to 1980 nm, associated with the O-H chemical bond. They used K-Nearest Neighbors (KNN) and Support Vector Machine (SVM) algorithms for classifying the mortar types and predicting their compressive strength. The results showed a clear correlation between the average reflectance and curing time, indicating changes in the mortar's hydration process (Figure 2-13). The SVM classification model demonstrated the highest prediction accuracy of approximately 90%, making it the recommended algorithm for mortar classification. Furthermore, they found a strong correlation between the mortar's compressive strength and the average reflectance in the 1920–1980 nm wavelength range, with a correlation coefficient exceeding 0.95. This suggests that hyperspectral imaging can be a valuable nondestructive tool for rapidly predicting the compressive strength of mortar, with potential applications in concrete pavement strength prediction (Fan et al., 2020).

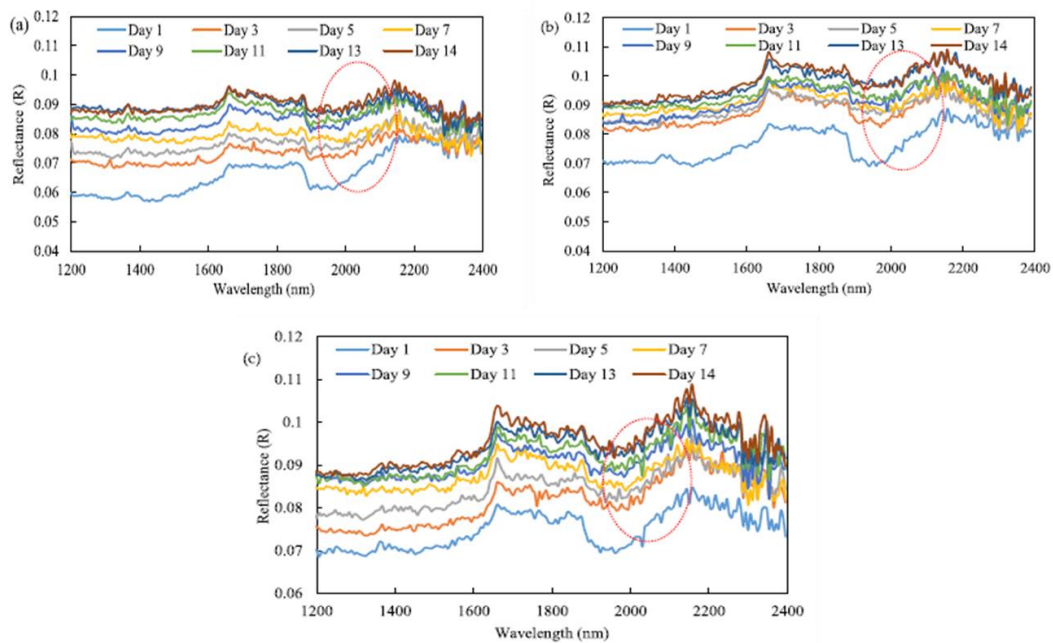


Figure 2-13 Average reflectance spectra in the wavelength range of 1200 nm to 2400 nm for samples with a W/C ratio of: (a) 0.6, (b) 0.5, and (c) 0.4 (Fan et al., 2020)

Additionally, in other paper (Zahiri et al., 2018) the use of short-wave infrared (SWIR) spectrometry to classify concrete samples based on their water-to-cement (w/c) ratios and predict their density was explored. Concrete spectra from various w/c ratios (50%, 65%, 80%) were analyzed within the 1300–2200 nm range. They developed a Partial Least Square Discriminant (PLSD) Analysis model using 36 samples, achieving an 89% correct classification rate for 18 validation samples. The study demonstrates that SWIR spectrometry effectively detects differences in initial w/c ratios for hardened concretes (Zahiri et al., 2018).

Furthermore, the research shows that differences in density and compressive strength related to w/c ratios can be indirectly estimated through SWIR spectrometry. The results indicate the potential of spectral analysis for rapid detection of faulty concrete in large, in-situ applications, although further extensive laboratory and field testing across various materials and conditions is needed for direct adoption of these approaches (Zahiri et al., 2018).

In the most recent study about the application of hyperspectral imaging in cement industry by Diane et al. (2023), a novel and rapid method for predicting the mass loss of cement samples using a combination of Machine Learning (ML) and hyperspectral imaging is introduced. They aim to provide an alternative and non-destructive analytical approach to estimate analyte concentration in a specific matrix accurately and immediately, addressing the needs of analytical chemistry (Diane et al., 2023).

The study demonstrates the reliability and accuracy of their approach by developing a predictive ML model that performs well, especially with partial least squares regression. They achieve high validation scores, indicating the effectiveness of the method. Furthermore, the authors suggest the potential for further optimization and enhanced performance by selectively focusing on relevant wavelengths through a feature selection approach. The article concludes that the combination of HSI and ML will play a crucial role in cement quality control in the future, offering a

sophisticated and multidisciplinary approach for estimating mass loss in cement samples(Diane et al., 2023).

CHAPTER 3

EXPERIMENTAL PROGRAM

The main lines of the experimental work were based on obtaining the hyperspectral imaging system (HSI) and getting it to work. After that, in order to obtain the hyperspectral images of the main cement compounds, a synthesis work plan was set to produce enough amount of each of those compounds that can be utilized in all the required characterization work. Finally, the hyperspectral imaging system was used to scan the prepared samples, and the test results were processed and used to create an identification model for those compounds using HSI techniques.

3.1 The Hyperspectral Imaging System

The hyperspectral imaging system used in this thesis, which combines a hyperspectral camera and a light microscope enables the acquisition of hyperspectral images using a special software as shown in Figure 3-1.

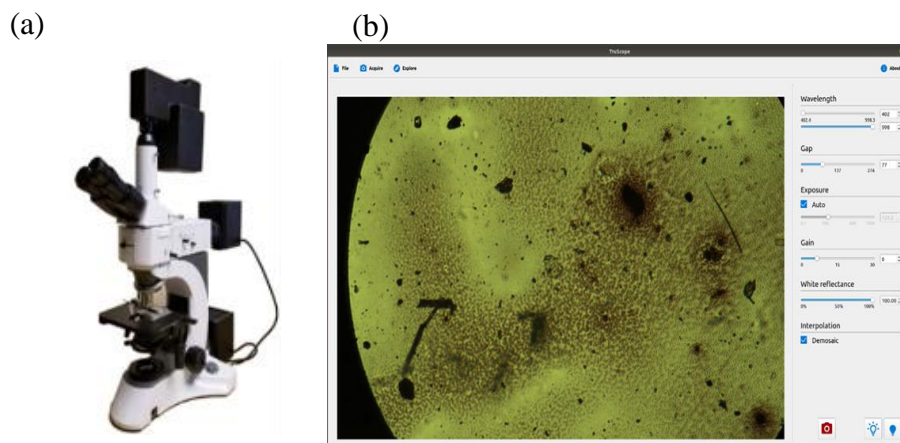


Figure 3-1 (a) Hinalea hyperspectral camera mounted on the microscope, (b) Truescope software interface

3.1.1 The Hyperspectral Camera

The Hinalea Model 4200 Wide-Field Hyperspectral Camera used in this study, as it is shown in Figure 3-2 is a versatile instrument designed for laboratory and industrial use. It offers high configurability, capturing contiguous, high-resolution images from 400 nm to 1,000 nm across the visible to near-infrared spectrum. This camera eliminates the tradeoff between spectral bands and spatial resolution. It supports up to 300 standard spectral bands with a spectral resolution of 4 nm FWHM. The measuring area for this camera (for industrial uses) is 310 mm × 80 mm × 80 mm and can operate in a temperature range of 20°C ± 5°C with a humidity level of 65% non-condensing. The camera also offers optional illumination and the capability to scan objects at a perpendicular angle for versatile imaging. However, the camera used in this study was modified to be installed on the trinocular of a polarized microscope.

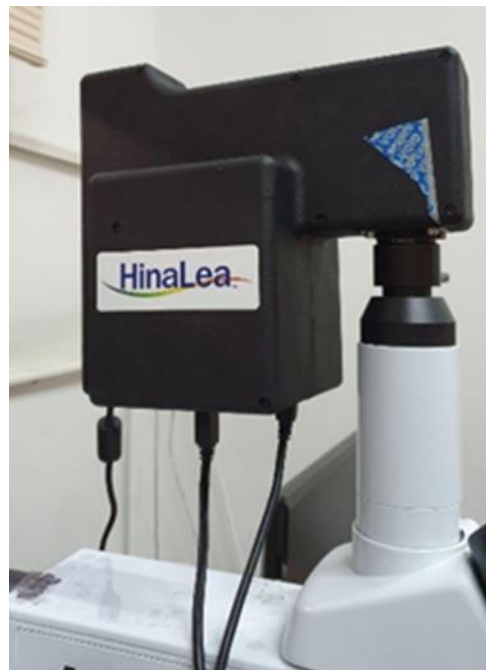


Figure 3-2 The Hinalea Model 4200 hyperspectral camera

3.1.2 The Microscope

The microscope used in this study was AMSCOPE ME 520 T microscope, which offers a total magnifications (through the binoculars) from 50x to 1000x using seven plan-achromatic objective lenses. It features dual illumination for various sample types, and supports brightfield, darkfield, and polarization microscopy, which can reveal intricate material details, such as stress patterns. Its infinity-corrected optical system has the ability to reduce optical errors when using filters and in-line components.

3.1.3 The Hyperspectral Imaging Software

The system manufacturer provided a software package named Truescope, allowing the transfer of images to a computer via a high-speed USB 3.0 connection (Figure 3-1(b)).

The software facilitates the adjustment of camera settings through an additional USB connection. To ensure image clarity under high magnifications, it is necessary for the samples to possess flat surfaces or be specially prepared as thin or polished sections suitable for microscope examination. The focusing process is manually performed on the microscope to achieve optimal image quality. The software enables users to adjust various settings related to hyperspectral imaging.

The wavelength range detected by the software tool can be adjusted within the range of 400 to 1000 nm. Moreover, the software allows for the adjustment of exposure time, gap, and white light reflection values. These settings exhibit varying degrees of influence on the type of sample and the desired level of measurement precision. However, the most significant factor affecting the outcomes is the gap adjustment, which is a variable in the Fabry-Perot interferometer (FPI) method, Illustrated in Figure 3-3. The reflective component of this filter comprises two parallel mirrors with a specific distance interval, possessing high reflection capabilities and oriented

towards each other. The gap between the mirror surfaces represents a resonant gap, where incident light undergoes multiple reflections amidst the coated surfaces defining the gap. When the gap width corresponds to an odd multiple of half the wavelength of the incident light, the resulting reflected beams constructively interfere, leading to maximal optical transmission. Conversely, at other gap width values, the reflected beams interfere destructively, potentially causing a decrease in optical transmission towards zero. Consequently, this device functions as a selective bandpass filter, facilitating the transmission of specific wavelengths. To achieve high reflectivity and transmission, insulating mirrors are employed instead of metallic mirrors (Koonen, 2006; Milne et al., 2009; Sikdar & Kornyshev, 2019).

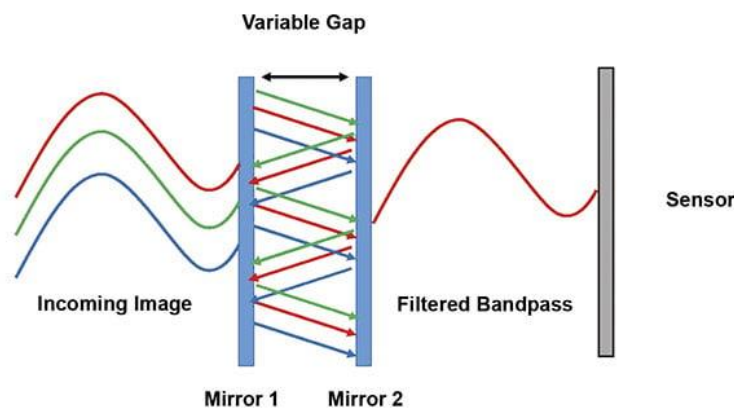


Figure 3-3 The working principle of FPI filter used in HS camera (Fong et al., 2018)

After the necessary adjustments are made using the microscope and the software, the complete process of acquiring measurements from the sample takes an average of approximately 60 seconds. The measurements are recorded in two file formats: a data cube (that contains the spatial data and the corresponding spectrums) and a header file (that provides metadata for the acquired data). Furthermore, the obtained measurements can be visually displayed within the Truescope software, enabling the

extraction of spectral measurements from specific desired points (up to 10 points) on the image. The scale visible in Figure 3-4 spans a total length of 1 mm, which corresponds to a distance of 900 pixels in the image captured with a 10x objective lens. Consequently, in the images obtained with the 10x objective lens in this system, each pixel corresponds to 1.11 μm of the sample. Beneath each acquired pixel spectral data is recorded, representing the measured reflectance ratio for the selected wavelengths ranging from 400 to 1000 nm.

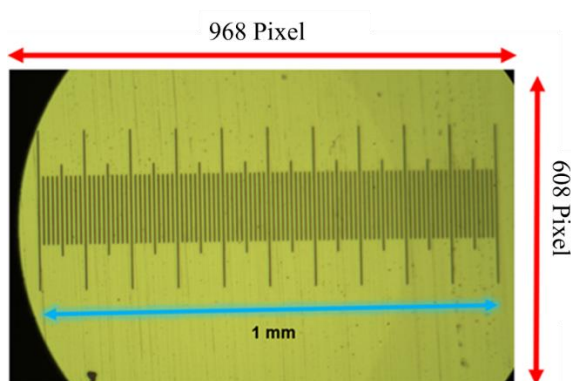


Figure 3-4 scale of 1 mm in pixel measurements

3.2 Raw Materials

In this thesis study, the utilization of pure raw materials was employed due to the crucial significance of purity in the synthesized compounds of cements. Those materials are explained in the upcoming sections.

3.2.1 Calcium Carbonate, CaCO₃

One of the primary constituents of the cement compound is CaCO₃, and the purity of CaCO₃ plays a crucial role in the quality of the resulting material. The CaCO₃ used in the conducted tests was sourced from TEKKIM company, known for providing highly pure materials (purity level of 98% or greater). The XRD pattern depicted in the Figure 3-5 represents the outcome of the analysis conducted on this specific material.

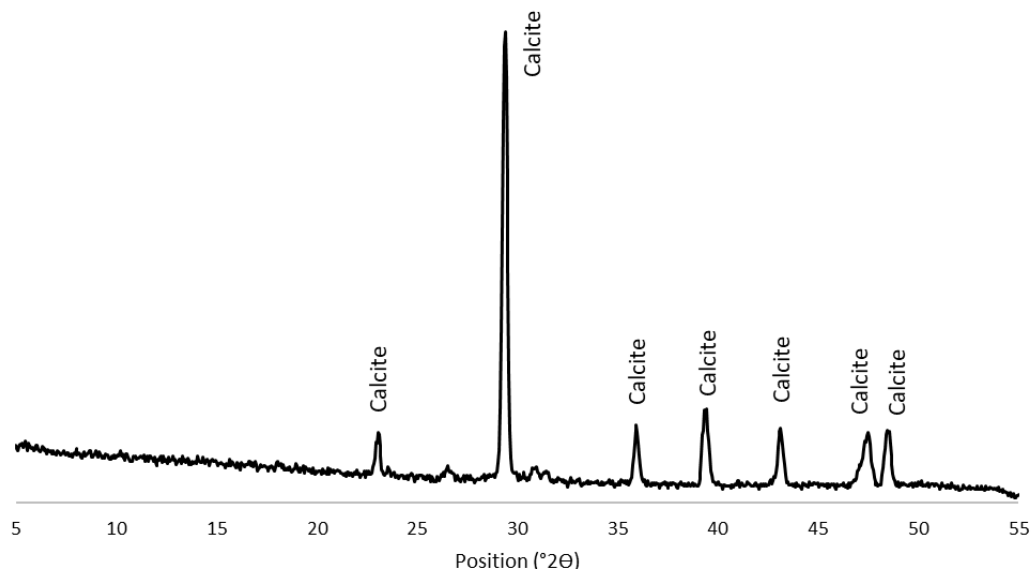


Figure 3-5 XRD pattern of TEKKIM CaCO₃

3.2.2 Quartz, SiO₂

The quartz sand used for this study was obtained from Kırıkkale region, which exhibited a high purity level of 97% as determined by XRD analysis. Sand particles were grinded with special ball mill grinder and subsequently, the ground material

was sieved through a 75 μm sieve. The XRD test result for this material is illustrated in Figure 3-6.

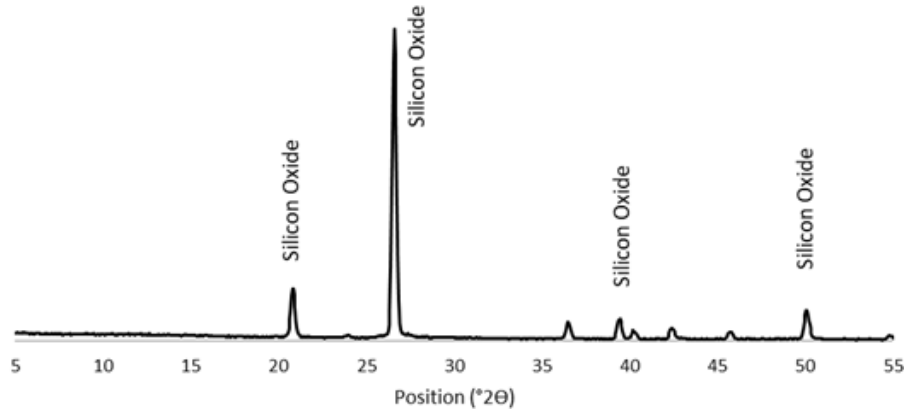


Figure 3-6 XRD pattern of SiO₂

3.2.3 Aluminum Oxide, Al₂O₃

In order to produce the aluminate phase of cement, a highly pure Al₂O₃ from TEKKIM with a purity level of 98% or greater was utilized. The XRD result for this material is depicted in Figure 3-7.

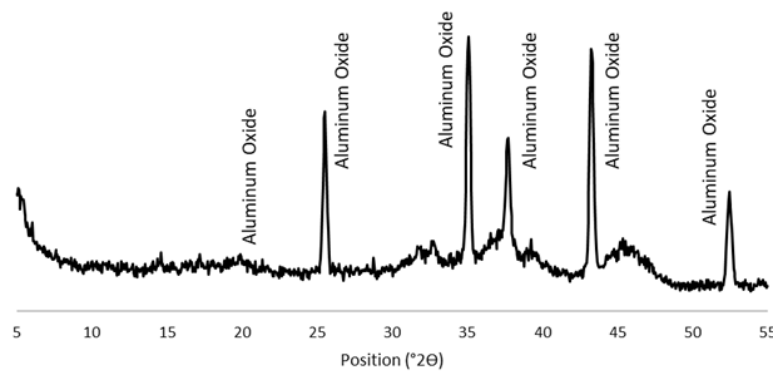


Figure 3-7 XRD pattern of Al₂O₃

3.2.4 Minor Stabilizers

To minimize the likelihood of phase alterations during the production and quenching processes of the materials, minor stabilizers were incorporated into each mixture. These stabilizers were carefully selected for their high purity chemical compositions. Al_2O_3 and MgO were employed as a stabilizer in the production of C_3S , while H_3BO_3 was utilized in the production of C_2S . The minor stabilizers in each case constitute less than 1% of the total mixture weight.

3.3 Synthesis Processes of Cement Compounds

Various synthesizing methods of Portland cement compounds were identified in the literature. By selecting the proportions and heating regime from one article as a base, through a series of trial-and-error processes, the methods used by Wesselsky et al. were refined with minor modifications to improve the production of the cement compounds in this study (Wesselsky & Jensen, 2009). In addition, a specially designed furnace was used for the synthesis process.

This custom-designed Protherm ELV MOS 160 furnace stands out for its safety feature, permitting door opening at high temperatures without compromising user safety or oven integrity. This furnace is tailored for laboratory bottom loading procedures, known for its impressive temperature range up to 1600°C . Figure 3-8 depicts the Protherm ELV MOS 160 oven.



Figure 3-8 Protherm ELV MOS 160 furnace showing the elevated specimen holding platform on the right

3.3.1 C₃S Synthesis

The crystalline structure of C₃S adheres to a stoichiometric ratio of 3:1 for CaO to SiO₂. To stabilize the monoclinic form of C₃S, small quantities of MgO and Al₂O₃ are introduced into the raw material mix, resulting in the substitution of calcium by magnesium atoms and the replacement of both calcium and silicon atoms by aluminum in equal proportions. These raw materials are combined in a cylindrical container and acetone is added to create a fluid mixture. The resulting mixture is then transferred to a platinum crucible and placed in the oven. The sintering process involves a 2-hour heating ramp to 1600 °C, followed by a 2-hour hold at that temperature. After removal from the oven, the crucible is promptly transferred to a minus 40°C refrigerator for the quenching process. The materials were kept in the refrigerator for 1 hour then placed in a desiccator. The raw materials proportions and heating regime is given in and Figure 3-10 Table 3-1 respectively. Due to the restricted capacity of the crucible used in each trial, there was a limitation on the

amount of material that could be produced (since the total volume of the special platinum crucibles used was 40 ml) as it is shown in Figure 3-9.



Figure 3-9 Hot crucible while removed from the furnace

Table 3-1 Raw materials proportions for synthesizing C_3S

Material name	$CaCO_3$	SiO_2	Al_2O_3	MgO
Weight (g)	102.091	20.674	0.56	0.9416

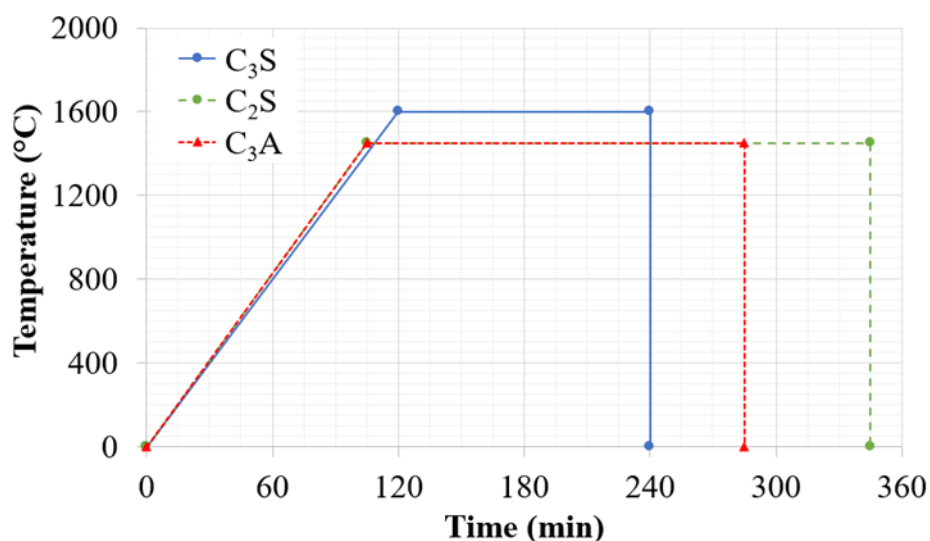


Figure 3-10 Heating regimes of the oven during the synthesis of cement compounds

3.3.2 C₂S Synthesis

In this research, the β -form of C₂S was synthesized. The mixtures in the β -form consist of a precise combination of 2 moles of CaO and 1 mole of SiO₂, which are stabilized using H₃BO₃, as listed in Table 3-2. Similar to C₃S, all the ingredients were thoroughly mixed in powdered form inside a cylindrical container with a lid. Acetone was added to the mixture, before it was transferred to a platinum crucible. The filled crucible was subsequently placed in the furnace and heated to 1450 °C over a duration of 105 minutes. It was then maintained at this temperature for an additional 4 hours before being promptly moved to the refrigerator for the quenching process at -40 °C (Figure 3-10). The quenching was particularly critical for preserving the C₂S compound, as it can easily transform into its non-reactive form, known as γ -C₂S. After 1 hour of cold treatment C₂S was removed from the crucible and kept in a desiccator to prevent any possible hydration.

Table 3-2 Raw materials proportions for synthesizing C₂S

Material name	CaCO ₃	SiO ₂	H ₃ BO ₃
Weight (g)	92.601	29.533	0.300

3.3.3 C₃A Synthesis

The stoichiometric combination of 3 moles of CaO and 1 mole of Al₂O₃ results in the formation of the Cubic modification of C₃A (Table 3-3). Like the other compound mixtures, the raw materials are first mixed in a container with a lid, in powdered form. Acetone is then added to create a paste-like mixture, which is subsequently placed in a crucible.

The sintering process involves heating the sample for a duration of 1 hour and 45 minutes, gradually reaching a temperature of 1450 °C. The sample is then held at this temperature for 3 hours. Following the sintering process, the sample is rapidly quenched at -40 °C (Figure 3-10).

Table 3-3 Raw materials proportions for synthesizing C₃A

Material name	CaCO ₃	Al ₂ O ₃
Weight (g)	94.454	32.075'

3.4 Sample Preparation for Pastes

The clinkers are first crushed and then finely ground using the Retsch ball mill PM 100, located in the Materials of Construction Laboratory at METU, to prepare the paste. This planetary benchtop single station ball mill uses centrifugal forces to produce in very high pulverization energy and therefore short grinding times. The

grinding process takes place in a grinding jar with a volume of 500 ml, capable of grinding up to 220 ml of material per batch. The grinding duration varies for each material due to differences in their hardness. The specific grinding periods for each material can be found in Table 3-4. In order to prevent excessive heat buildup in the grinding jar and minimize material sticking to the jar walls, a pause in the grinding process is implemented every 2 minutes. During this pause, the mixture is manually stirred using a spoon. The determination of these specific grinding durations and speeds involved a process of trial and error to optimize the grinding efficiency.

Table 3-4 Grinding duration and rotational speed for each cement compound with Retsch ball mill grinder

Material name	Duration	Rotational speed
C ₃ S	5 minutes	450 r.p.m
C ₂ S	8 minutes	600 r.p.m
C ₃ A	4 minutes	500 r.p.m

3.5 The Physical Properties of the Cement Compounds

Following the grinding process, the cement compounds were sieved using a 63 µm sieve (no.240). The resulting powdered material's fineness was determined using a particle size distribution (PSD) device, specifically the Malvern Mastersizer 2000 laser diffraction equipment, located at TürkÇimento. This equipment allows for precise measurement and the analysis of particle sizes in the cement compounds.

In addition, the density of cement compounds was determined according to EN 196-3.

3.6 Sample Preparation For HSI

Both thin sectioning and polish sectioning techniques were employed, to examine clinkers and cement compounds under the microscope.

3.6.1 Thin Sectioning

Cement compound clinkers are meticulously prepared as thin sections for subsequent examination under a hyperspectral microscope. Initially, the clinker form was employed for the creation of thin sections; however, due to the occurrence of broken clinker fragments during the filing phase, the cement form was subsequently utilized. The cement clinker compounds underwent a grinding process and were subsequently combined with an impermeable synthetic resin to undergo transformation into a solid cuboidal sample. This sample was meticulously polished using precision files to achieve a uniform thickness. Subsequently, these prepared samples were affixed to glass slides. In the final stages of preparation, the samples underwent filing and smoothing processes to achieve a thinness conducive to detection under the transmittance format of hyperspectral studies. Prepared samples are shown in Figure 3-11.

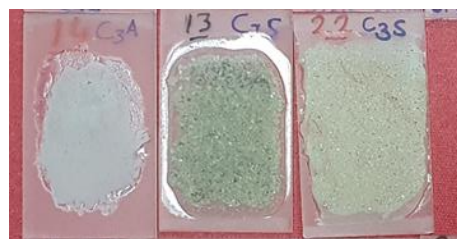


Figure 3-11 Thin sections of cement compounds

3.6.2 Polished Sectioning

In the polished sectioning method, clinker pieces were embedded in a colored resin within cylindrical molds. The addition of color to the resin enhanced light reflection during microscopic analysis. After 24 hours, when the resin had hardened, the specimens were removed from the molds, and the surfaces were sequentially ground using coarse and fine grinders. Finally, the specimens were polished using aluminum paste to achieve a smooth and reflective surface. The detailed steps involved in specimen preparation can be found in the accompanying Figure 3-12. For each cement compound 10 readings from the surface of the polished section were gathered.



Figure 3-12 Steps for molding cement compound for polish sectioning for HIS

3.7 Characterization Methods

Different characterization methods were used to verify the quality of the produced cement compounds and support the outcomes of the test results.

3.7.1 X-ray Diffraction (XRD) Analysis

X-ray diffraction (XRD) is a widely employed technique for investigating the crystal structure of materials. It capitalizes on the interaction between X-rays and atoms within a crystalline sample. When X-rays are directed at a crystal, they scatter in diverse directions due to their interaction with the electron clouds surrounding the atoms. This scattering phenomenon generates a distinct diffraction pattern that provides valuable insights into the arrangement of atoms within the crystal lattice. By precisely measuring the angles and intensities of the diffracted X-rays, the positions and distances between atoms in the crystal structure can be determined, allowing for the characterization of different materials based on their unique diffraction patterns.

The XRD measurements of raw materials, cement compounds, and pastes at various time intervals (1, 3, 7, 28, and 90 days) were taken using the BTX III Benchtop XRD Analyzer, located at the Materials of Construction Laboratory in METU. This device enables measurements within a range equal to $5-55^\circ$ 2θ angle of diffraction. The obtained X-ray diffraction data was presented in a graphical form. Match! Phase Analyzer software was used to analyze the XRD results. By comparing the peaks in the diffractograms with known peaks of various minerals, the corresponding mineral phases were identified.

3.7.2 Fourier Transform Infrared Spectroscopy (FTIR) Analysis

Fourier transform infrared spectroscopy (FTIR) is a rapid, non-destructive, and cost-effective method for analyzing the chemical structure of materials. It falls under the category of spectroscopy and shares similarities with hyperspectral imaging systems. FTIR spectroscopy offers valuable insights into the chemical composition and structure of materials in a reliable and efficient manner. It has become a widely used technique in various fields, providing researchers with a powerful tool for qualitative and quantitative analysis.

In FTIR spectroscopy, a sample is exposed to a beam of infrared light, and the resulting transmitted light is detected. Infrared light covers a wide range of wavelengths within the electromagnetic spectrum. When the infrared light interacts with the sample, certain frequencies are absorbed by the molecules due to their vibrational and rotational motions.

The detector in an FTIR instrument measures the intensity of the transmitted light across different wavelengths. The collected data is then processed using a mathematical technique called Fourier transformation. This transformation converts the raw data into a spectrum that illustrates the absorption of infrared light by the sample at various frequencies. For this study, the FTIR analysis was conducted using a Bruker FRA 106/S instrument located in the METU Central Laboratory. The cement compounds and their pastes were examined at intervals of 1 day, 7 days, and 28 days.

3.7.3 Isothermal Calorimetry Testing

Isothermal calorimetry is a technique used to quantify the heat flow occurring during a chemical reaction or process at a constant temperature. By monitoring the heat variations within a sample placed in a calorimeter, valuable information about reaction energetics, heat capacity, and reaction kinetics can be obtained. In this study, the TAM AIR isothermal calorimeter, an 8-channel micro-calorimeter, was utilized in the DSI laboratories.

Sand was employed as a reference material on each channel. The sand reference material, along with the sample, experienced the same isothermal conditions throughout the experiment. The heat flow in the reference material and the sample was simultaneously monitored, allowing for the determination of the heat flow specific to the reaction or process of interest. Sand was chosen as the reference material due to its widespread availability, stability, and minimal reactivity. Its well-

known heat capacity and thermal properties served as a reliable baseline for comparison.

In the experiment, 4 g for each of C_3S , C_2S , C_3A , and C_3A mixed with 25% weight of gypsum were mixed with 2 g of distilled water outside the chamber and then placed in the isothermal calorimetry device. However, the first 3 minutes of the hydration reaction were not captured in the results due to this setup. The heat flow for 28 days of reaction was recorded in this test.

3.7.4 Compressive Strength Testing

The individual compounds of cement paste play a significant role in determining its compressive strength. To assess the contribution of each ingredient to the compressive strength, the compressive strength of each material was tested at various hydration durations: 3, 7, 28, and 90 and 180 days.

Due to the daily production limitations of the cement compound, special designed small cubic molds with a side length of 2.5 cm were used (Figure 3-13).

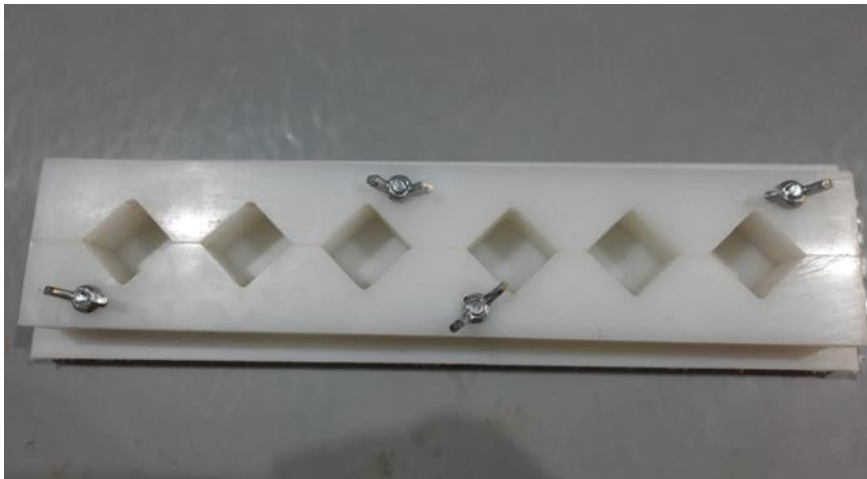


Figure 3-13 Cubic specimen molds for compressive strength test with side of 2.5 cm

An MTS universal testing machine was employed to apply load to the specimens, with a loading rate of 0.01mm/second. A displacement-controlled loading was used for more precise measurement and due to the sensitivity of the produced pastes. To ensure consistency, the water-to-cement ratio (W/C) was carefully selected for each sample to achieve a normal consistency, and EN 197-3 was employed for mixing procedure. The W/C ratio for each paste mixture is provided in Table 3-5. Furthermore, C₃A paste was tested both individually and in combination with 25% gypsum by weight to measure the compressive strength. The effect of water curing and air curing in 95±5% humidity was also checked for each compound.

Table 3-5 Water to cementitious material ratio

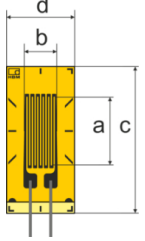
Paste material	C ₃ S	C ₂ S	C ₃ A	C ₃ A+gyp
W/C	0.3	0.25	0.5	0.5

3.7.5 Modulus of Elasticity

The modulus of elasticity, also referred to as Young's modulus or elastic modulus, provides a measure of a material's stiffness and its ability to deform when subjected to stress. It establishes a quantitative relationship between stress and strain within the material. Typically, the modulus of elasticity is expressed in units such as Megapascals (MPa) or gigapascals (GPa).

In the context of measuring the elastic modulus of cement compounds, the mixing proportions described in section 3.7.4 were used. Special cylindrical specimens with a diameter of 2.5 cm and a height of 5 cm were prepared for testing purposes. The MTS Universal Testing Machine was employed to apply the required load. To measure the strain, strain gauges from HBM were utilized. Detailed information about these strain gauges can be found in Table 3-6.

Table 3-6 Properties of used strain gauges

	a	b	c	d	K	Nominal resistance
	10 (mm)	5 (mm)	18.5 (mm)	9.5 (mm)	2.11	120 Ω

The strain gauges were affixed securely (using a special glue) to the specimen's side surface, which had been smoothed using a sandpaper. This method facilitates the precise measurement of strain, as illustrated in Figure 3-14.

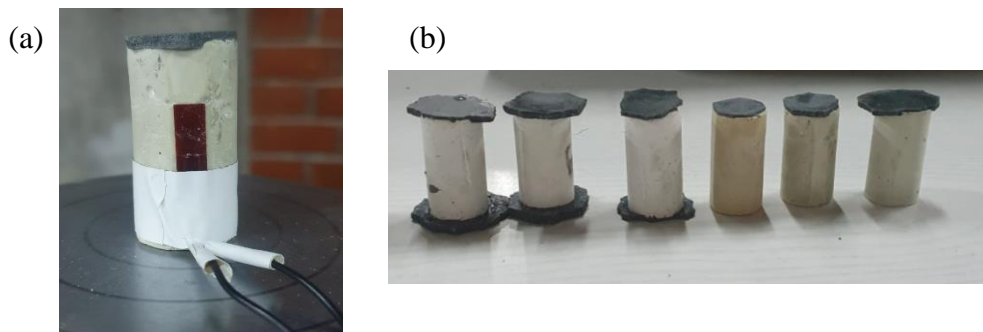


Figure 3-14 (a) Attached strain gauge to the cylindrical specimen, (b) capped cylindrical specimens

The changes in strain were recorded using a data acquisition system. After gathering the required data, the strain was calculated using a formula that considers various parameters.

$$\frac{\Delta R}{R} = K \cdot \varepsilon$$

Equation 3-1

In this formula, ΔR represents the resistance change during the application of stress, R denotes the nominal resistance, k represents the gauge factor or sensitivity factor, and ε represents the strain.

3.7.6 Scanning Electron Microscopy (SEM)

SEM is an advanced imaging technique that offers in-depth surface information of specimens by employing a focused electron beam to scan the sample surface. During this process, the electron beam interacts with the atoms in the sample, resulting in the emission of secondary and backscattered electrons. Specialized detectors capture these emitted electrons, enabling the creation of highly detailed, three-dimensional images that provide insights into the sample's surface topography. Furthermore, SEM can conduct elemental analysis using energy-dispersive X-ray spectroscopy (EDS), which allows for the identification and mapping of elements within the sample. In this study, the clinkers and hydration products of cement compounds paste were examined using a QUANTA 400F Field Emission SEM with a resolution of 1.2 nm, located at the Central Laboratory in METU. The investigation for paste samples spanned various time intervals, including 1 day, 3 days, 28 days, and 90 days of reaction.

CHAPTER 4

RESULTS AND DISCUSSION

4.1 Use of Conventional Techniques for Characterization of Cement Compounds

4.1.1 X-Ray Diffraction Results

X-ray diffraction (XRD) analysis is employed to ensure the quality and purity of the produced cement compounds. The XRD patterns for the three main compounds are presented in Figure 4-1.

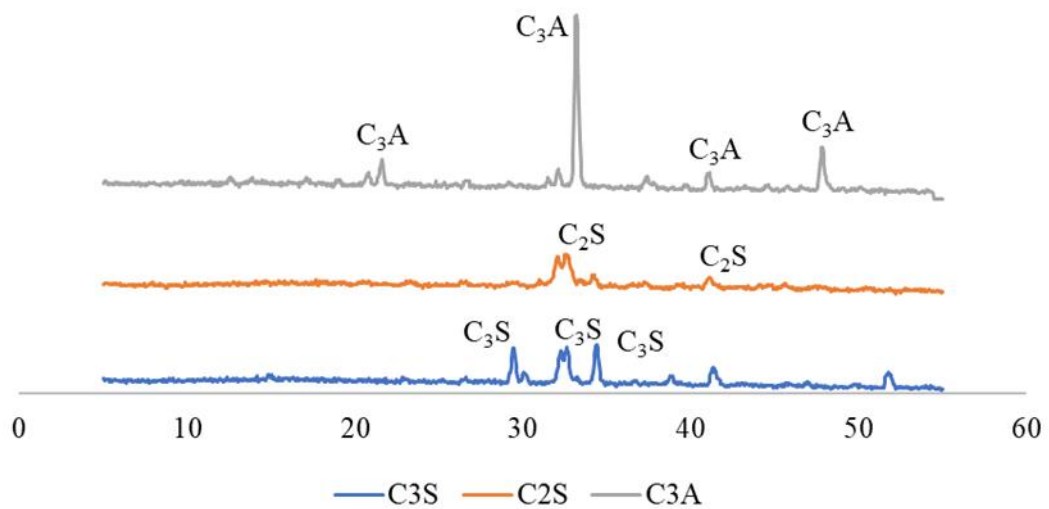


Figure 4-1 XRD patterns of synthesized C₃S, C₂S, and C₃A, where the peaks are for the pure form of each compound

The primary 2θ positions for C_3A are recorded at 33.169° and 47.625° , as per the PDF 2 database. In the case of both C_3S and C_2S , their 2θ positions coincide with three of the principal peaks at 32.007° , 32.570° , and 41.03° . However, C_3S exhibits additional distinctive peaks at 29.505° , 30.147° , 34.413° , and 51.784° . The XRD analysis reveals that C_3A exhibits the most crystalline structure among the compounds. Furthermore, the absence of any impurities in the produced cement compounds is confirmed by these XRD findings.

4.1.2 Fourier Transform Infrared Results

Figure 4-2 presents the FTIR spectra for each of the pure cement phases. Additionally, Table 4-1 provides a list of the significant bands observed for each compound. Based on the available literature on FTIR analysis of C_3S , it is noted that strong peaks at 883 and 925 cm^{-1} can be attributed to the asymmetric stretching (ν_3) Si-O band, while a smaller peak at 815 cm^{-1} corresponds to the symmetric stretching (ν_1) Si-O band within the SiO_4 tetrahedron (Lü et al., 2016; Omotsoa et al., 1995; Sáez Del Bosque et al., 2014).

The absorption peaks of the second silicate compound in portland cement (C_2S) are predominantly observed in the range of 800 to 1000 cm^{-1} . Specifically, the strong peaks at 836 and 944 cm^{-1} can be attributed to β - C_2S and correspond to the symmetric stretching vibration of Si-O bonds within the silicon tetrahedron. Furthermore, an absorption peak at 867 cm^{-1} indicates the presence of asymmetric stretching vibrations of Si-O bonds (Y. Liu et al., 2017; Maheswaran et al., 2016; Rodrigues, 2003a).

The FTIR results for C_3A are characterized with thin peaks between 500 to 900 cm^{-1} . The major peaks near 900 , 865 , 820 , 780 and 705 cm^{-1} are assigned to the condensed AlO_4 tetrahedral groups (Fernández-Carrasco & Vázquez, 2009; Solanki et al., 2021; Trezza & Lavat, 2001).

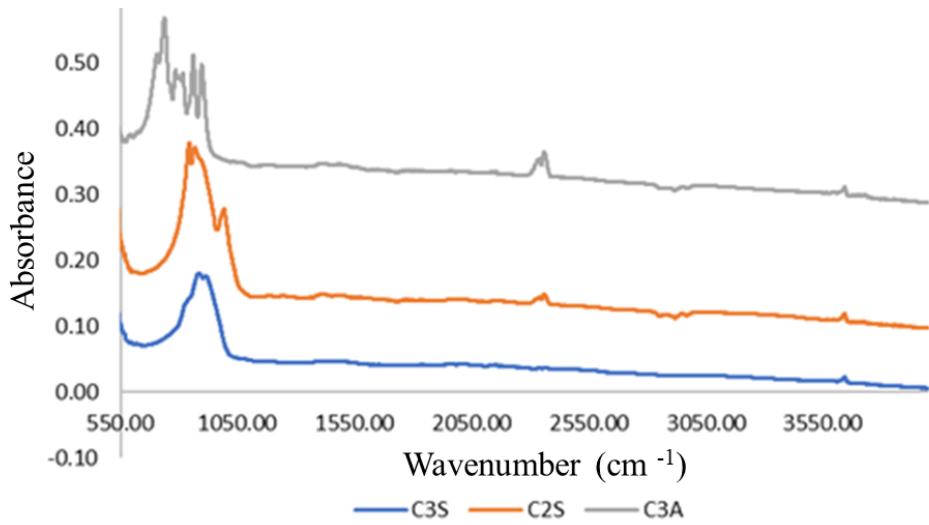


Figure 4-2 FTIR patterns of synthesized C₃S, C₂S, and C₃A

Table 4-1 Peak lists of FTIR results for synthesized C₃S, C₂S, and C₃A

	Absorption wavenumber (cm ⁻¹)					
C ₃ S	815	883	925			
C ₂ S	836	867	944			
C ₃ A	702	741	783	814	862	895

4.1.3 Microstructural Characterization of Clinker Compounds through Scanning Electron Microscopy

4.1.3.1 C₃S Clinker

Figure 4-3 showcases the smooth surface of anhydrous C₃S clinker, providing a visual representation of its homogenous structure. Some debris can be observed in Figure 4-3 (a), along with the presence of open and closed pores distributed

throughout the samples and their sizes varies from 2 μm to 100 μm . EDX analysis of the samples in Figure 4-3 (d) confirms the presence of Ca and Si as the main compounds of the produced C_3S .

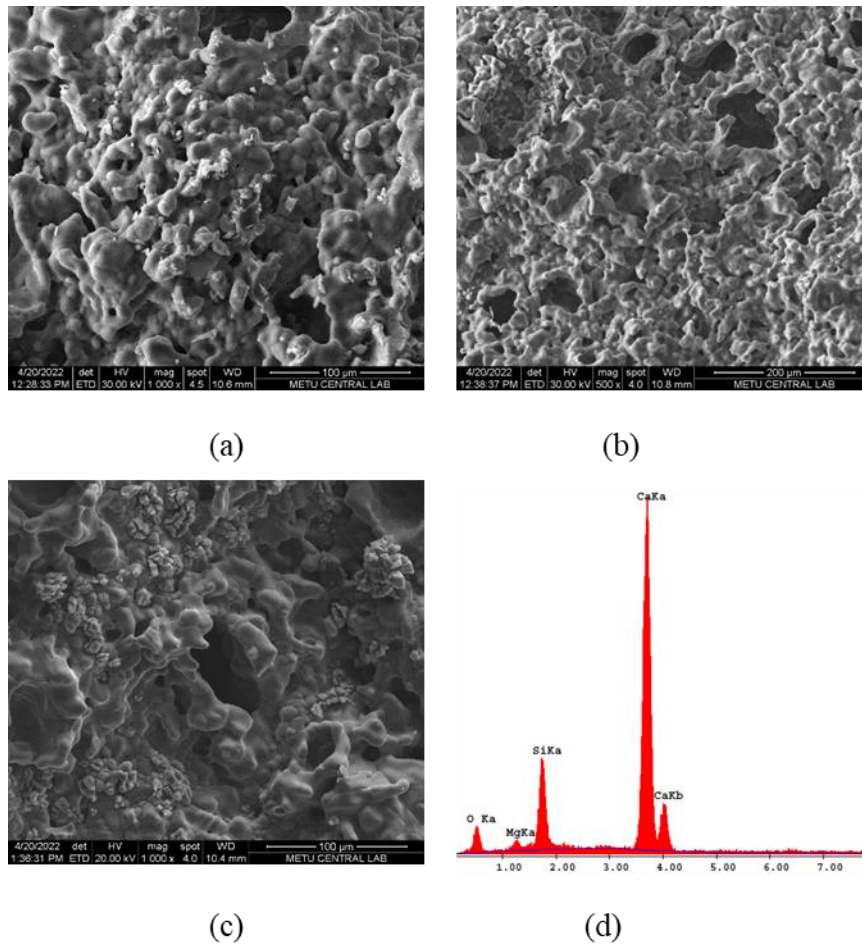


Figure 4-3 SEM images of synthesized C_3S (a) 1000 x (b) 500 x, (c) 1000 xx, (d) EDX of (b)

4.1.3.2 C_2S Clinker

Figure 4-4 displays SEM images of β - C_2S clinker, revealing spherical and smooth belite crystals as depicted in Figure 4-4 (a & d). Similar to C_3S (Figure 4-3), the β - C_2S clinker exhibits openings of varying sizes, ranging from 10 μm to 115 μm , which

are illustrated in Figure 4-4 (b). The crystal sizes typically range from 10 μm to 20 μm . Additionally, the EDX results for Figure 4-4 (a) highlight the presence of abundant Ca and Si in the sample.

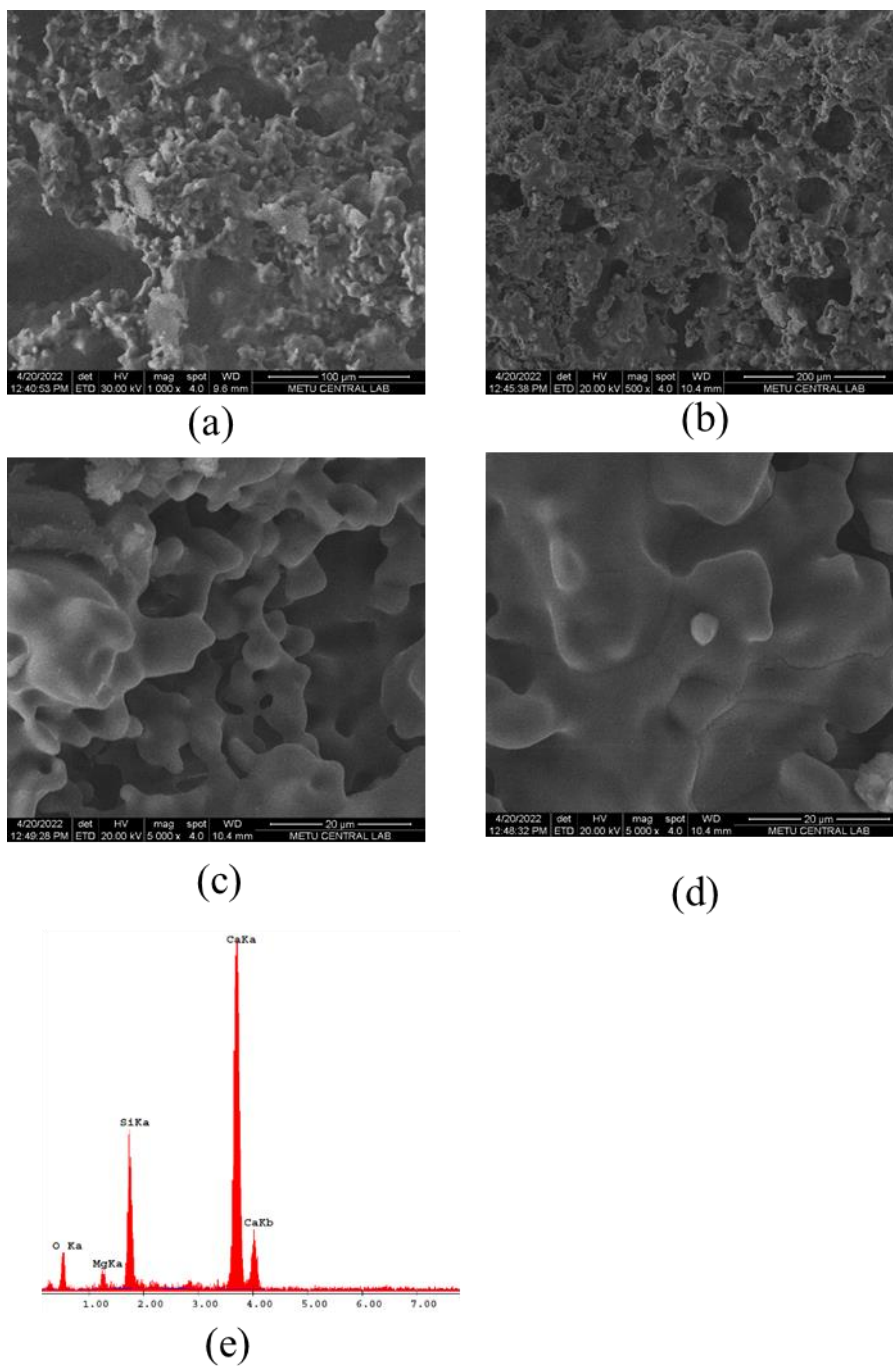
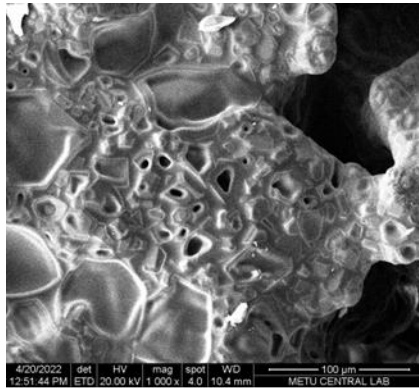


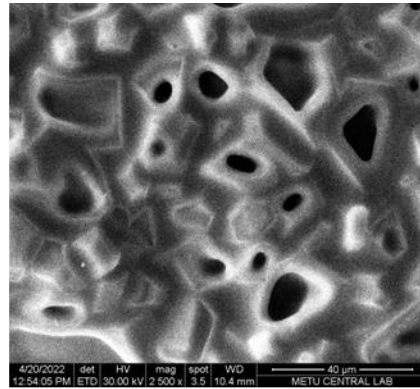
Figure 4-4 SEM images of synthesized C_2S (a) 1000 x, (b) 500 x, (c) 5000 x, (d) 5000 x, (e) EDX of (b)

4.1.3.3 C₃A Clinker

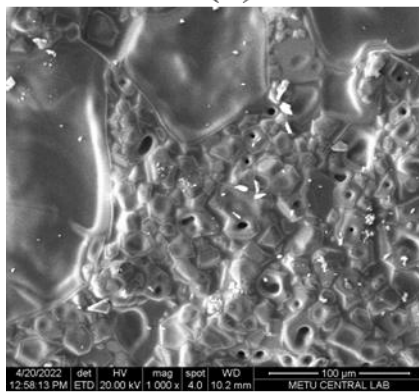
Figure 4-5 demonstrates that among the produced cement compounds, C₃A clinkers exhibit the most crystalline shape compared to the others. The crystals appear as angular particles with smooth surfaces, and they exhibit various shapes such as hexagonal and orthorhombic. Additionally, the crystal sizes vary significantly, ranging from 2 μm to 200 μm (Figure 4-5 (b)). This wide range of crystal sizes may be attributed to the cooling rate of the clinker after being removed from the furnace. The EDX analysis of the sample is depicted in Figure 4-5 (e), confirming the composition of the C₃A clinker.



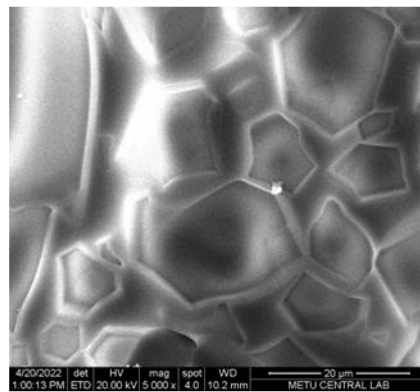
(a)



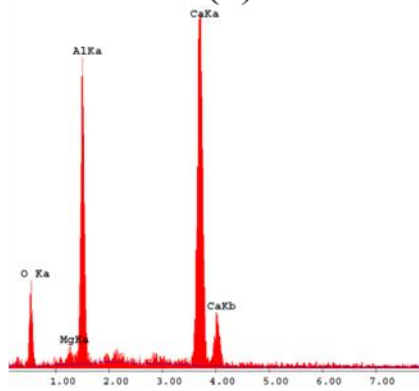
(b)



(c)



(d)



(e)

Figure 4-5 SEM images of synthesized C_3A (a) 1000 x, (b) 2500 x, (c)1000 x, (d) 5000 x, (e) EDX of (a)

4.2 Characterization of the Hydration Behavior of the Cement compounds

4.2.1 Physical Properties of the Ground Cement Clinker

4.2.1.1 Density

The density of each cement compound was determined according to the EN 196-3 standard after the grinding process. The results of the density tests are presented in the Table 4-2.

Table 4-2 Density results of synthesized C₃S, C₂S, and C₃A

Compound	C ₃ S	C ₂ S	C ₃ A
Density (g/cm ³)	3.17	3.26	3.03

4.2.1.2 Particle Size Distribution

The powder form of cement clinker phase is required for preparing paste samples, and the fineness of the cement powder plays a crucial role in the hydration reactions, setting time, and compressive strength of the samples. The particle size distribution results are depicted in Figure 4-6, which provides information about the distribution of particle sizes in the cement powder. In addition, the ratio of the particles passed from each sieve opening listed in Table 4-3.

Analyzing the particle size distribution helps in understanding the reactivity and performance of the cement material in subsequent applications. The grinding results reveal that, within the particle size range of 1 μm to 50 μm, all phases exhibit a notable 3-10% increase in the quantity of finer particles when compared to the standard CEM I. However, for coarser grains surpassing 50 μm, it's noteworthy that

C₂S particles demonstrate a substantial 10% increase in quantity. It is observed that both C₃A and C₂S are finer than CEM I in all cases. The coarser particles of C₂S can be attributed to its hardness, as excessive grinding can result in an excess of fine material within the 10-50 μm particle range and an uneven particle size distribution.

Table 4-3 Passed ratio (%) of particles for each cement compound

Sieve opening	C ₃ S	C ₂ S	C ₃ A	Average of (C ₃ S- C ₂ S- C ₃ A)	CEM I
10 (μm)	48.27	46.73	50.22	48.41	41.39
30 (μm)	87.74	72.94	80.2	80.30	81.12
45 (μm)	97.53	88.06	92.85	92.81	94.07
60 (μm)	99.98	96.51	98.64	98.38	98.97
90 (μm)	100	100	100	100	100

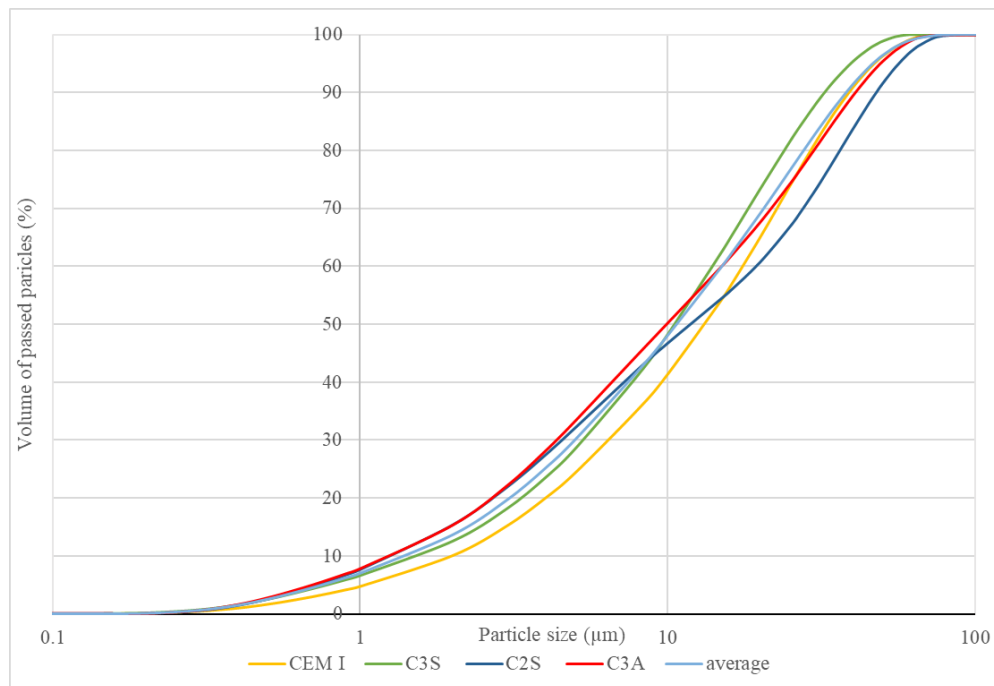


Figure 4-6 Particle size distribution of synthesized C₃S, C₂S, and C₃A, CEM I, and average of synthesized C₃S, C₂S, and C₃A

Furthermore, when these materials are mixed in approximately the same proportions as in ordinary Portland cement (60% C₃S, 28% C₂S, 12% C₃A), the average grading is very similar to CEM I.

4.2.2 Heat Evolution (Isothermal Calorimetry)

The isothermal calorimetry testing of the produced compounds was conducted over a period of 28 days, and the rate of heat evolution (measured in mW/g of solid) during the initial 75 hours (3 days) is depicted in Figure 4-7. Besides the main compounds C₃S, C₂S, C₃A, a fourth mixture (C₃A+G) including 75% C₃A and 25% of gypsum (by mass) was also tested, as the hydration reaction of C₃A was too fast and commenced prior to the placement of the sample capsule inside the isothermal calorimetry device, with the maximum measurable heat evolution rate for this material being 9.6 mW/g. The results obtained from the isothermal calorimetry indicated that the C₃A+G mixture exhibited the highest rate of heat evolution, reaching its peak value of 11 mW/g at 210 minutes (3.5 hours). Subsequently, the heat flow rate for C₃S ranked third. The hydration of C₃S displayed an increasing trend and reached its peak at the 12th hour, with a heat flow rate of 2.5 mW/g of solid. As known, C₂S contributes to the compressive strength of cement at later stages, indicating a delayed onset of hydration. The findings from isothermal calorimetry supported this observation, with C₂S exhibiting the lowest exothermic heat evolution rate during the initial 4 days. It displayed a small peak at the 15th hour of hydration, with the maximum rate of heat evolution reaching 0.3 mW/g.

For C_3A+G , the dormancy period occurs approximately 70 minutes after the initial hydration, and the initial set commences after this duration. Similarly, for C_3S , the dormancy period lasts for approximately 3.15 hours, followed by the initiation of the hydration process. In the case of C_2S , the dormancy period extends to around 7.3 hours before the onset of the hydration reaction.

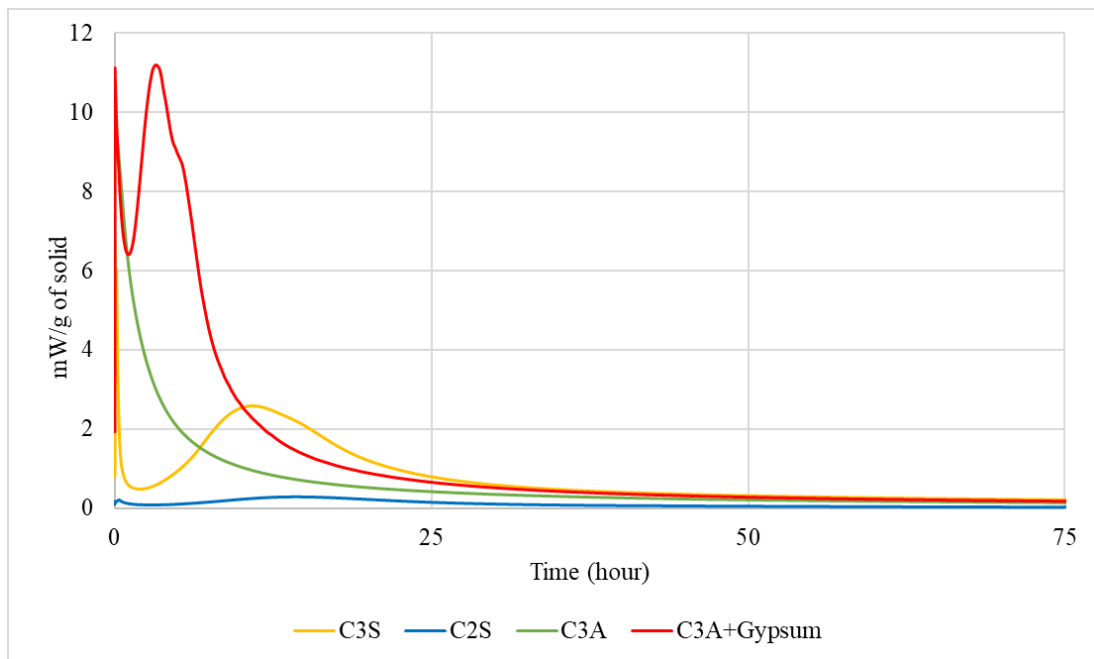


Figure 4-7 heat evolution of cement compounds during the initial 100 hours

The cumulative heat profiles over a period of 28 days, as illustrated in Figure 4-8, demonstrate similar trends for C_3S , C_2S , and C_3A+G . Among these compounds, C_3A+G exhibits the highest heat evolution, reaching a value of 491 J/g, followed by C_3S with a heat evolution of 300 J/g. In contrast, C_2S shows the lowest energy release among the cement compounds, measuring only 54 J/g. It is worth noting that the heat production of C_3A resulted in an abnormal outcome, as the high heat generation at the beginning of hydration and the expansion of hydration products led to the

breaking of the container. To ensure accurate measurements, the test was repeated for C₃A, and in each instance, it concluded with the capsule breaking.

Furthermore, in order to monitor temperature fluctuations during the combination of water and C₃A, these two materials were mixed outside the container in a mixing bowl, and temperature variations were measured using a thermal camera. According to the thermal camera results, during the initial minutes of hydration, an exothermic reaction led to an increase in the mixture's temperature, reaching up to 90°C, as illustrated in Figure 4-9.

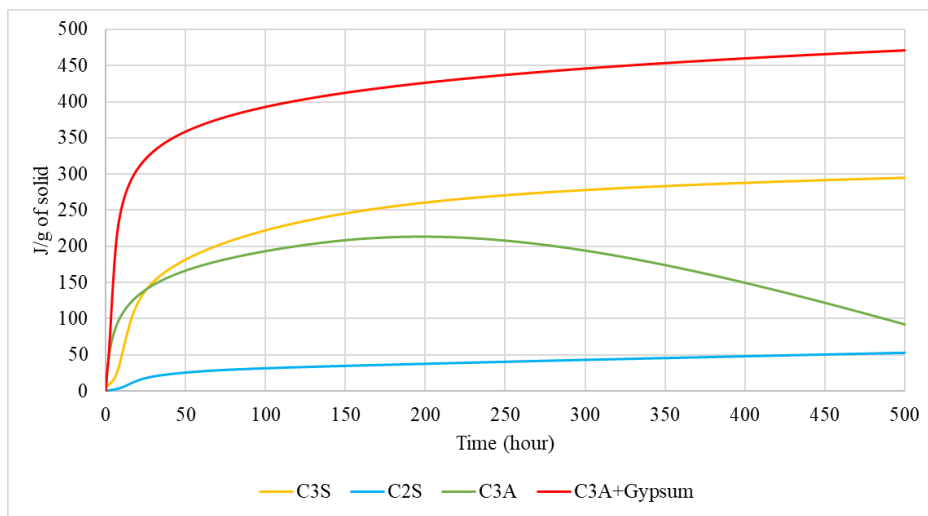


Figure 4-8 Cumulative heat profiles over a period of 28 days for cement compounds

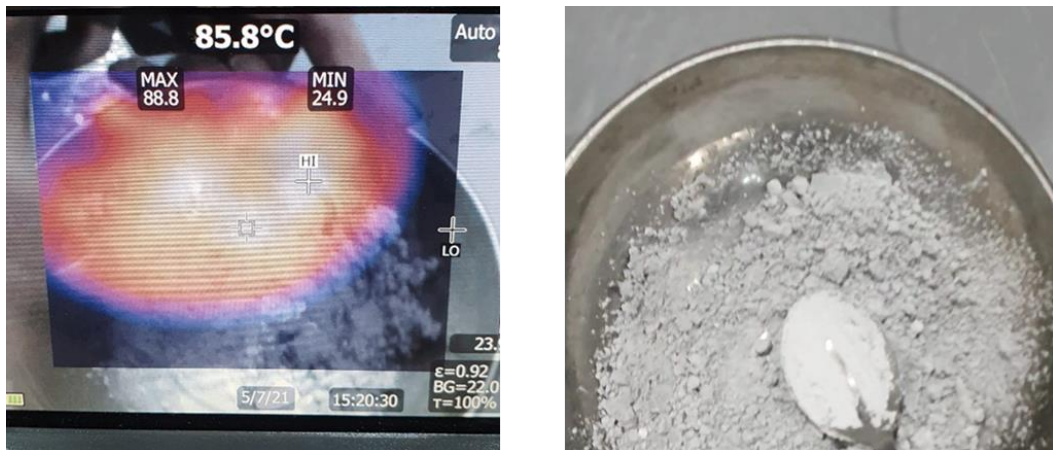


Figure 4-9 Temperature increases of C_3A during first minutes of hydration according to thermal camera

4.2.3 X-Ray Diffraction Analysis of the Hydrated Compounds

Curing plays a crucial role in the process of hydration and the subsequent development of strength in concrete. To investigate the impact of curing methods on cement compound samples, attempts were made to subject them to both air curing and water curing. However, it was observed that not all the hydrated cement compounds could endure water curing, as some of them exhibited dissolution in the water medium. Notably, water curing yielded meaningful results for the case of C_3S , and the 28-day hydration of C_2S was assessed and recorded as follows.

4.2.3.1 Hydrated C_3S

C_3S specimens were subjected to two distinct curing conditions to investigate their strength development and the potential emergence of product variations. The initial set of samples cured at room temperature under controlled humidity conditions of $95\pm 5\%$. Conversely, the second set of specimens was subjected to curing in a water medium with a saturated calcium hydroxide (CH) ratio.

a) Air cured samples

The XRD patterns for the samples cured in air are presented in Figure 4-10. As per the X-ray diffraction (XRD) findings, even after a duration of 180 days, a residual quantity of unreacted C_3S persists. The identification of C-S-H gel, a fundamental hydration product, remains challenging through XRD analysis due to its intrinsically amorphous structural properties, which complicate the process. However, the progression of the hydration process can be effectively monitored by assessing the content of CH within the resultant hydration products. CH exhibits a crystalline structure, and its concentration exhibits a noticeable and continuous increase beyond the 180-day hydration period. The presence of a peak at 29.5° can be attributed to both $CaCO_3$ and C_3S . This phenomenon explains why, over time, while the amount of C_3S decreases as it gets consumed in the reaction, the quantity of $CaCO_3$ concurrently increases in the sample. In addition, the hump in the area between 5° to 10° indicates the increase of amorphous phase, CSH, in the compounds of products.

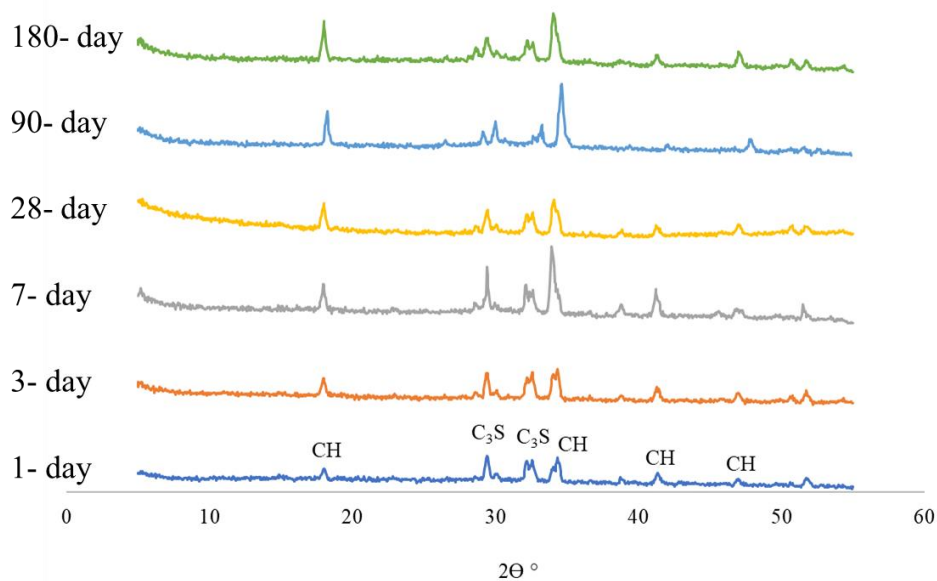


Figure 4-10 XRD patterns of air cured C_3S pastes after 1, 3, 7, 28, 90, 180 days of hydration

b) Water-cured samples

The XRD patterns of hydrated C_3S is shown in Figure 4-11. In this case also the produced material, which could be investigated by XRD, is CH crystals. The greater intensity of CH crystals observed in the XRD patterns is primarily associated with the higher concentration of CH within the hydrated materials.

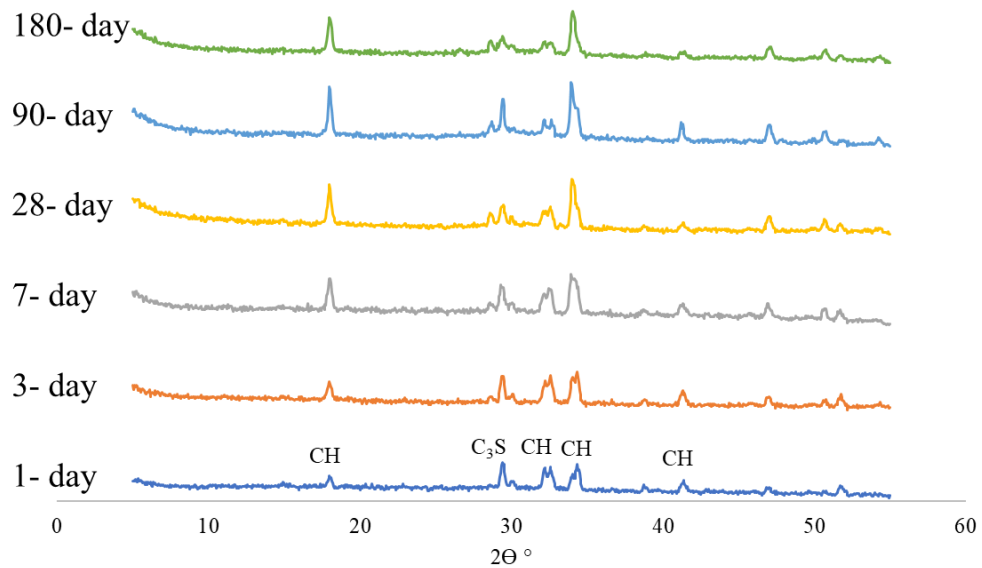


Figure 4-11 XRD patterns of water cured C_3S pastes after 1, 3, 7, 28, 90, 180 days of hydration

4.2.3.2 Hydrated C_2S

For C_2S samples, the application of water curing was only feasible at a later stage, specifically for ages exceeding 28 days. Additionally, it was not feasible to conduct X-ray diffraction (XRD) testing on the 1-day C_2S samples due to their elevated water content. As a result, XRD analysis was only carried out on the C_2S samples that were air cured for 3, 7, 28, 90, and 180 days.

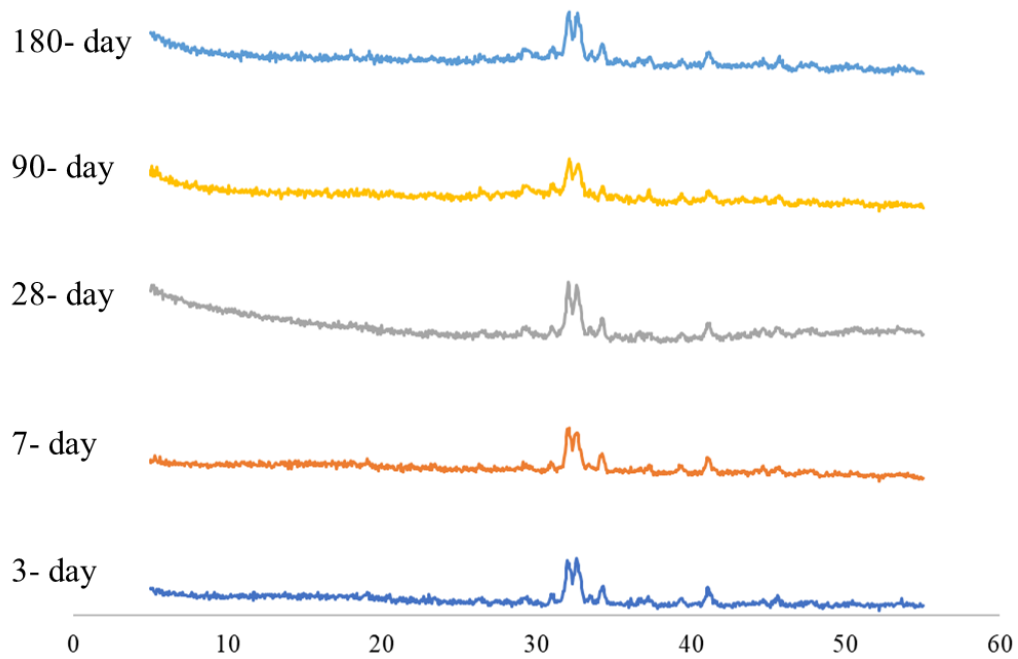


Figure 4-12 XRD patterns of air cured C_2S pastes after 3, 7, 28, 90, 180 days of hydration

Notably, the generation of CH is relatively restrained compared to C_3S , which is why it could not be discerned through distinct and well-defined peaks. However, the presence of CH can be inferred from the presence of small peaks in the XRD pattern (Figure 4-12). Furthermore, the broad hump observed in the range of $5-10^\circ$ signifies an increase in the amorphous phase, likely indicating the presence of C-S-H gel within the material.

4.2.3.3 Hydrated C₃A

XRD patterns depicting the hydrated C₃A are presented in the Figure 4-13. Analysis of these patterns reveals that during the initial 24 hours of hydration with water, C₃A transforms into C₃AH₆, commonly known as hydrogarnet. In the early stages, within the first 3 days, there is a notable decrease in the quantity of C₃A, accompanied by an increase in the formation of C₃AH₆. However, a reversal of this trend occurs between the 3rd and 7th days of hydration. During this period, the amount of C₃A starts to increase, while the quantity of C₃AH₆ decreases. This pattern continues until the completion of the 28-day hydration process.

Upon examining the XRD pattern at 90 days, a distinct and significant alteration is observed. This pattern indicates the decomposition of C₃AH₆ into CaCO₃ and Al(OH)₃. Furthermore, it is noteworthy that the amount of unreacted C₃A diminishes significantly after the 90-day period.

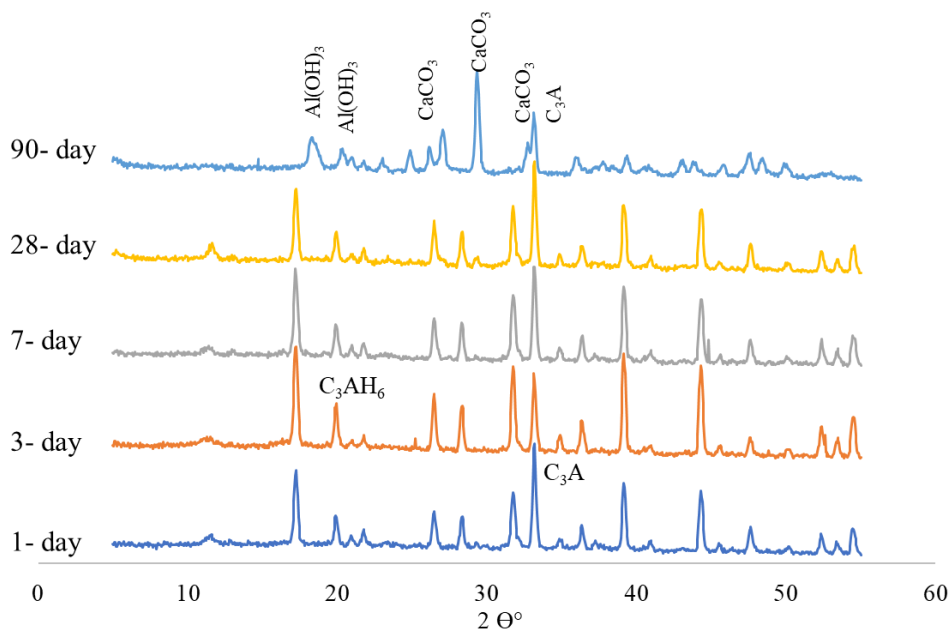


Figure 4-13 XRD patterns of air cured C₃A pastes after 1, 3, 7, 28, 90 days of hydration

4.2.3.4 Hydrated C₃A + G

The process of C₃A hydration in the presence of gypsum is known to be highly intricate and susceptible to instability, primarily due to the variable sulfate content in the surrounding environment. XRD analysis results depicted in Figure 4-14 provide clear evidence of this instability.

Upon examination of the XRD patterns, it becomes apparent that the initial stages of hydration, specifically within the first 24 hours, reveal the presence of ettringite and unreacted C₃A in the sample. However, as the hydration progresses and reaches the 28-day mark, a discernible shift occurs. At this stage, the production of mono-sulfate and various calcium aluminum sulfates, characterized by different Ca/S ratios, becomes evident.

Remarkably, as the hydration process extends beyond 28 days and reaches 180 days, there is a resurgence of gypsum in the XRD results. This cyclical appearance of gypsum underscores the complex and dynamic nature of the C₃A-gypsum interaction, indicating a recurring interplay between different sulfate-bearing phases throughout the extended hydration period. The decomposition of ettringite was investigated using XRD analysis, revealing a specific chemical formula representing the decomposition process. (Grounds et al., 1988)



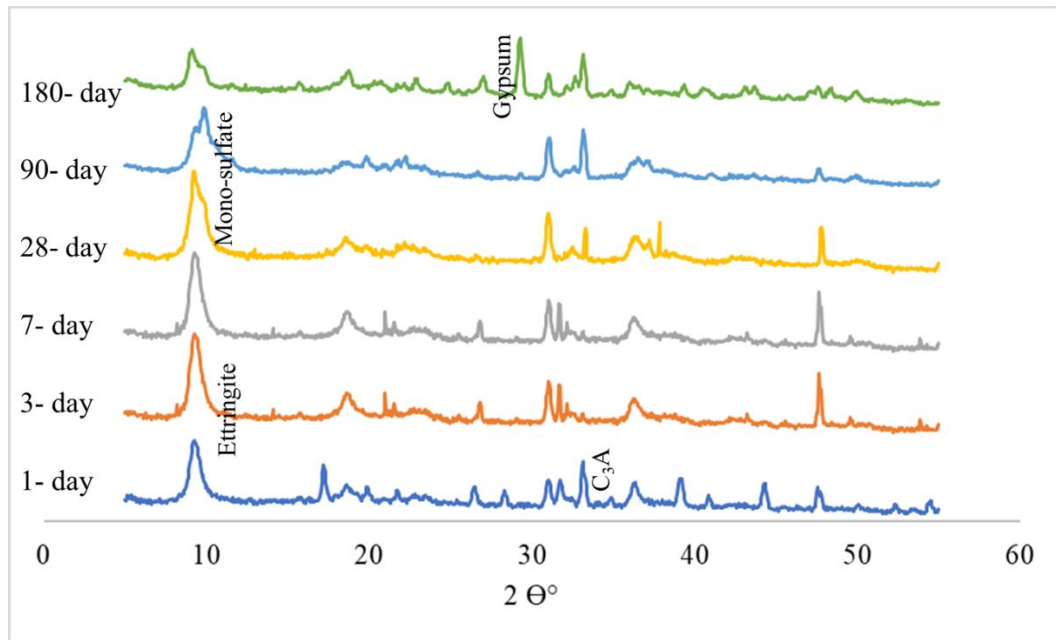


Figure 4-14 XRD patterns of air cured $C_3A + G$ pastes after 1, 3, 7, 28, 90 days of hydration

4.2.4 FTIR Analysis of the Hydrated Compounds

Figure 4-15 shows FTIR spectra for pure cement phases and their hydrated forms at 28 and 90 days. Table 4-4 summarizes significant bands for each compound for comparison. Specifically, peaks at 883 and 925 cm^{-1} are indicative of Si-O stretching (ν_3), while the 815 cm^{-1} peak represents Si-O symmetric stretching (ν_1) within the SiO_4 tetrahedra. (Higl et al., 2021; Lü et al., 2016; Sáez Del Bosque et al., 2014). After a 28-day period, the 925 cm^{-1} peak shifts to 814 cm^{-1} , which can be attributed to alterations in C_3S units and an increase in Q_1 units within the gel. This shift reflects variations in the Ca/Si ratio. Furthermore, the band at 3640 cm^{-1} corresponds to Ca(OH)_2 symmetric stretching (ν_1). However, following a 90-day interval, the 925 cm^{-1} peak experiences a shift to 954 cm^{-1} , which indicates polymerization of the C-S-H gel. (Mollah et al., 2000; Ping et al., 1999). The wide band observed at 3440 cm^{-1} corresponds to vibrations of H_2O molecules (ν_3 and ν_1), while the band at 1650 cm^{-1}

cm^{-1} represents H_2O vibration (ν_2). Additionally, bands located at 1420, 1490, and 870 cm^{-1} , among others, are associated with CO_3 vibrations and lattice (Omotoso et al., 1995).

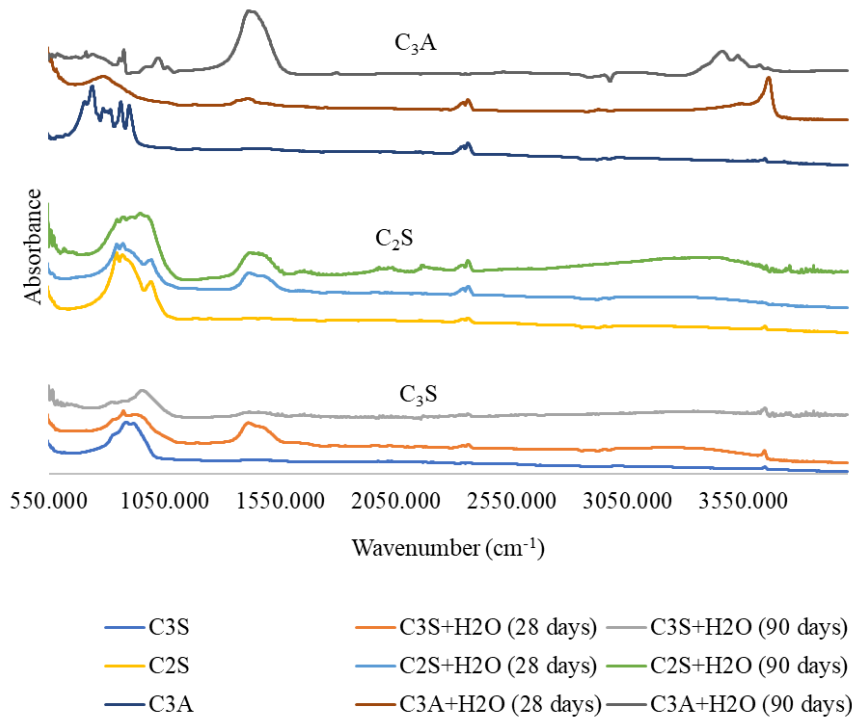


Figure 4-15 Results of FTIR test for synthesized C_3S , C_2S , and C_3A and their hydrated form after 28 and 90 days

Table 4-4 Peak list of FTIR results for pure C_3S , C_2S , 28 days and 90 days hydrated form

	Absorption wavenumber (cm^{-1})					
C_3S	815.7	883	925	0	-	-
$\text{C}_3\text{S}+\text{H}_2\text{O}$ (28 d)	814	875	934	1405	1478	3640
$\text{C}_3\text{S}+\text{H}_2\text{O}$ (90 d)	819	871	954	1409	3630	-
C_2S	836	867	944	-	-	-
$\text{C}_2\text{S}+\text{H}_2\text{O}$ (28 d)	844	879	992	1407	1482	-
$\text{C}_2\text{S}+\text{H}_2\text{O}$ (90 d)	844	875	909	954-976	1416	3642

The primary peaks in the C-S-H gel generated from both C₃S and C₂S are close in proximity. However, variations in crystal structure can be the cause of minor variations in peak positions and the C/S ratio within the C-S-H gel. The delayed hydration of C₂S leads to the emergence of the OH bond associated with calcium hydroxide in the sample that has been hydrated for 90 days.(Rodrigues, 2003b).

In the FTIR spectrum of C₃A (Figure 4-15) and its peaks list (Table 4-5), a notable band observed at 3666 cm⁻¹ signifies vibrations associated with water. Additionally, there is a peak around 3527 cm⁻¹, which suggests the potential presence of monocarboaluminate in the sample (Gismera-Diez et al., 2015). If carbonate groups are present in C₃A, they typically exhibit peaks in the 1400-1600 cm⁻¹ range, corresponding to carbonate (CO₃) group stretching vibrations. C₃A is more prone to carbonation compared to other Portland cement compounds, as supported by the FTIR results in this range (Fernández-Carrasco et al., 2012).

Table 4-5 Peak list of FTIR results for pure C₃A, 28 days and 90 days hydrated form

Absorption wavenumber (cm ⁻¹)						
C ₃ A	702	741	783	814	862	895
C ₃ A+H ₂ O (28 d)	789	1354	1419	3524	3660	-
C ₃ A+H ₂ O (90 d)	739	1018	1422	1797	3527	3666

4.2.5 Compressive Strength Testing

Cubic samples, each having a side length of 2.5 cm, along with their respective molds, are depicted in Figure 4-16. Notably, the compressive strength of C₃A, in the absence of gypsum, could not be determined due to the occurrence of cracking within the initial three days of the hydration process. These cracks appear to be linked to the phase transitions of C₃AH₆ into various calcium aluminate hydrate phases,

subsequently leading to its decomposition, as explained in section 4.2.2. The development of cracks in the hydrated C_3A is visually represented Figure 4-17, and these cracks progressively expand over time, ultimately resulting in the breakdown of the sample.

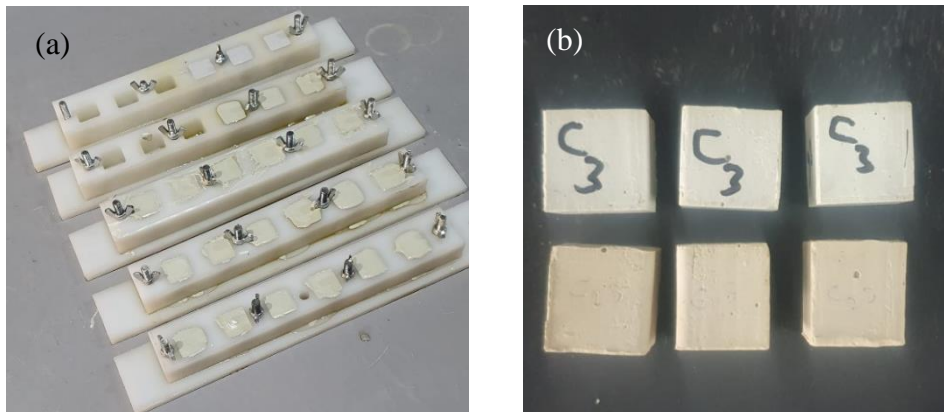


Figure 4-16 (a) Cubic molds for compressive strength test with side of 2.5 cm, (b) unmolded samples from the mold shown in (a)



Figure 4-17 Cracks generation after 4 days of hydration in C_3A sample

The results obtained from the compressive strength tests conducted on air-cured samples using universal testing equipment are also illustrated Figure 4-18. As expected, C_3S and C_3A compounds exhibit early strength development during hydration, surpassing the contribution of C_2S . Within the first 24 hours, the compressive strength of C_3S and C_3A reaches nearly 7 MPa. The rate of strength gain is higher for C_3S , as it reaches 35 MPa after 28 days of hydration, while C_3A achieves a strength of 10 MPa.

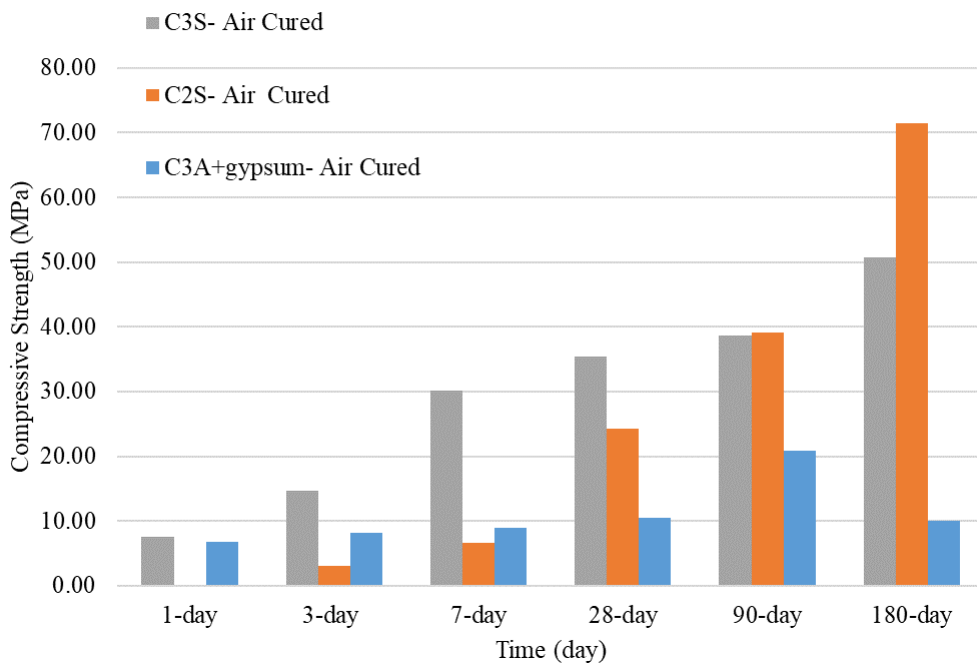


Figure 4-18 Compressive strength results of synthesized C_3S , C_2S , and $C_3A + G$, after 1, 3, 7, 28, 90 and 180 days of hydration

After three days of hydration, C_2S begins to exhibit increased strength, which becomes more pronounced in subsequent stages of the hydration process. Following a 180-day period of hydration, C_2S demonstrates a strength approximately 1.5 times higher than that of C_3S . However, after this 180-day period, a noticeable decline in strength becomes evident for $C_3A + G$ samples, likely due to the degradation of ettringite induced by carbonation.

Furthermore, in certain cases, water-cured tests were conducted. Specifically, C₃S could undergo water curing from the initial stages of hydration, while C₂S could only be water cured after 28 days, as before that period, cubic samples began to dissolve in water. C₃A mixed with gypsum could not be water cured throughout the 180-day hydration period, as it consistently exhibited either cracking or dissolution when exposed to water at all stages of the hydration process. Figure 4-19 indicates the results of water cured in comparison with air cured samples.

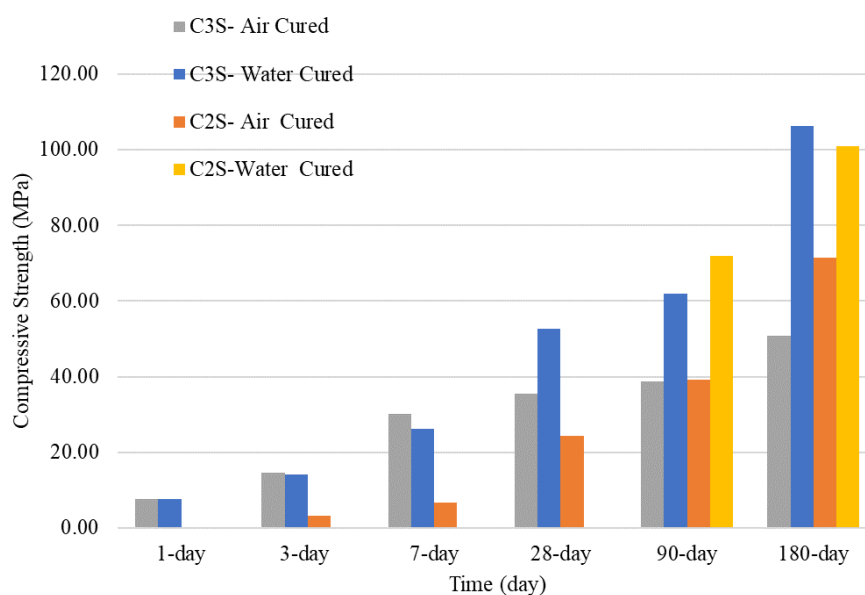


Figure 4-19 Comparison of air curing and water curing on results of Compressive strength for synthesized C₃S, C₂S, after 1, 3, 7, 28, 90 and 180 days of hydration

In the case of C₃S, the compressive strength of the samples subjected to water curing during the initial 7 days displayed either an equivalent or slightly lower strength, up to 10%, compared to those air cured. However, beyond this initial period, the rate of strength gain for water-cured samples significantly outpaced that of air-cured samples. After a hydration period of 180 days, the compressive strength of the water-cured C₃S samples reached 107 MPa, which exceeded twice the strength of their air-cured counterparts at 50 MPa.

Regarding C_2S , the substantial strength development primarily commenced after 28 days. To mitigate the risk of sample dissolution in water, water curing was initiated after this 28-day period. In this scenario, the compressive strength of water-cured C_2S samples equaled 72 MPa and 101 MPa at 90 days and 180 days, respectively.

4.2.6 Modulus of Elasticity

In adherence to ASTM C469 guidelines, the calculation of the modulus of elasticity necessitates the utilization of prepared specimens that have been appropriately capped, subjected to compressive strength testing conducted over three distinct cycles. Utilizing resistance change data, the modulus of elasticity is computed for each constituent. As per the findings obtained after a 28-day testing period, it is observed that the modulus of elasticity for C_3S exhibits the highest value when juxtaposed with the other two compounds, namely 22.45, 15.28 and 8.3 GPa, respectively.

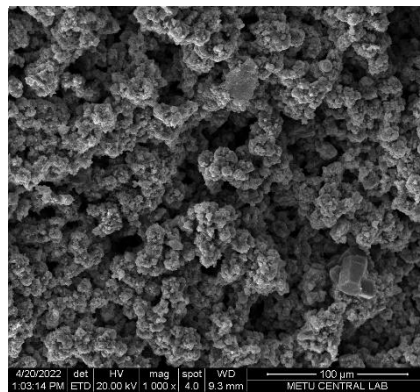
4.2.7 Microstructural Characterization of Hydrated Clinker Compounds through Scanning Electron Microscopy

4.2.7.1 Hydrated C_3S

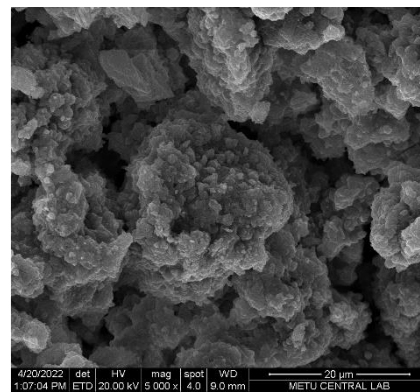
Figure 4-20 presents an examination of the morphological characteristics of hydration products in the context of C_3S following a 28-day reaction period. Analysis through SEM reveals the formation of a densely packed cluster consisting of C-S-H gel. Notably, this gel exhibits a uniform distribution throughout the sample, indicating substantial reactivity of C_3S during the 28-day duration.

It is worth highlighting that the calcium-to-silicon (C/S) ratio in the examined samples was determined to be 2.83 according to EDX results listed in Table 4-6.

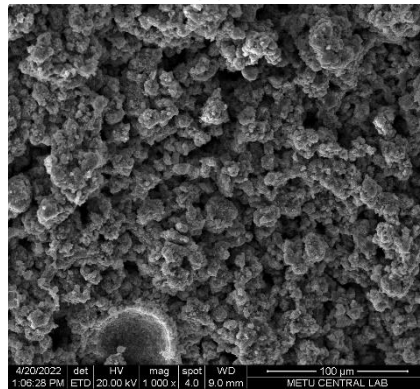
Furthermore, the investigation also discerns the presence of distinctive hexagonal CH crystals, as depicted in Figure 4-20 (d) with EDX analysis confirming the chemical composition of CH, as delineated in Figure 4-20 (e).



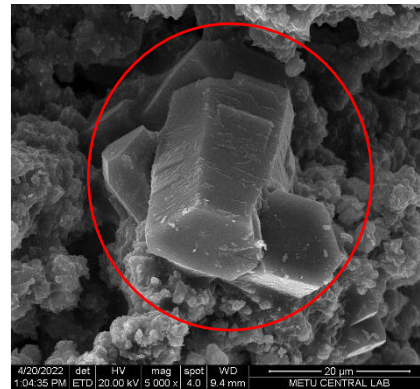
(a)



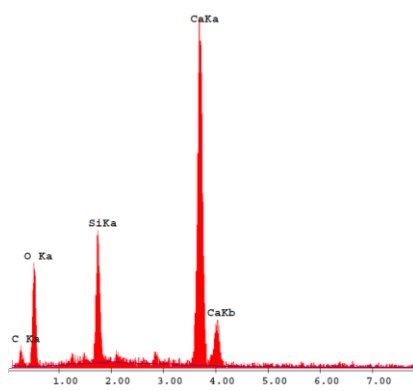
(b)



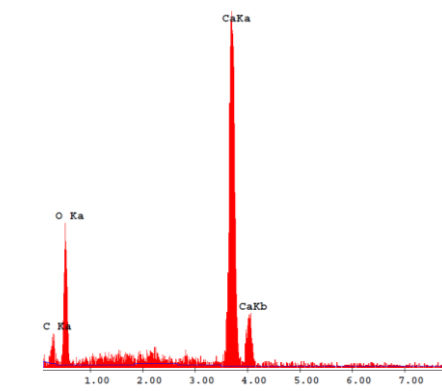
(c)



(d)



(e)



(f)

Figure 4-20 SEM images of 28- day hydrated C_3S , (a) 1000 x, (b) 5000 x, (c) 1000 x, (d) 5000 x, (e) EDX results of (a), (f) EDX of specified part at (d)

Table 4-6 Elemental analysis of produced C-S-H gel from hydration of C₃S

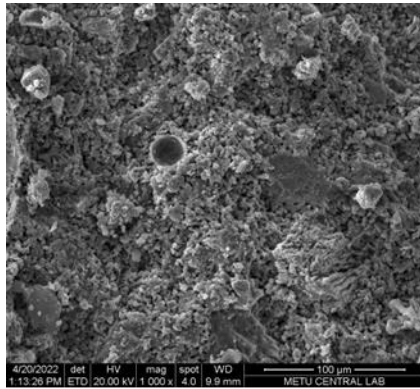
Element	Wt %	At%
O K	41.08	55.13
CaK	40.17	21.52
SiK	9.94	7.60
C K	8.80	15.74
Total	100.00	100.00

4.2.7.2 Hydrated C₂S

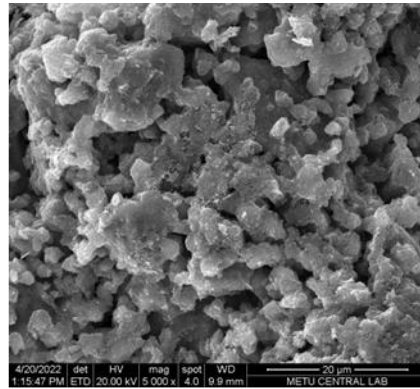
During the process of hydration for C₂S, it is noteworthy that the resulting C-S-H gel exhibits a notably denser structure when compared to the C-S-H gel derived from C₃S. This phenomenon is effectively illustrated in Figure 4-21 (a), where air voids ranging from 20 μm to 100 μm are visible in the samples. In Figure 4-21 (b), partially unhydrated C₂S particles can be observed, which are enveloped by a coating of CSH gel. Notably, the analysis via EDX Spectroscopy indicates a C/S ratio of 1.9 within the generated CSH gel as it is listed in Table 4-7.

Table 4-7 Elemental analysis of produced C-S-H gel from hydration of C₂S

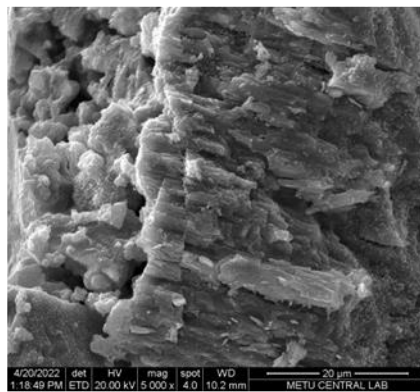
Element	Wt %	At%
O K	40.71	55.3
CaK	37.68	20.43
SiK	14.32	11.08
C K	7.28	13.18
Total	100.00	100.00



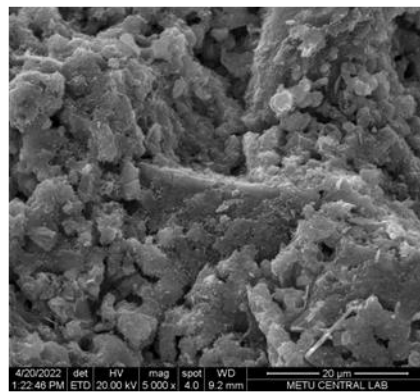
(a)



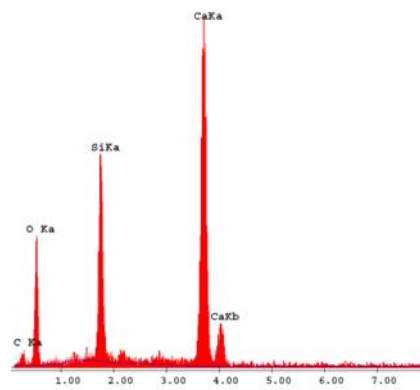
(b)



(c)



(d)

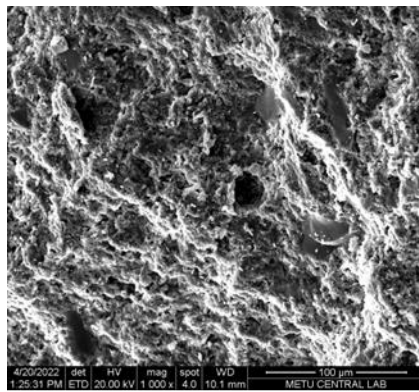


(e)

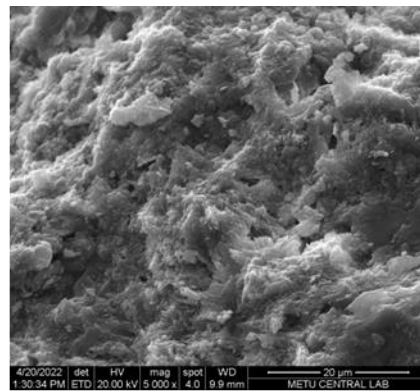
Figure 4-21 SEM images of 28- day hydrated C_2S , (a) 1000 x, (b) 5000 x, (c) 5000 x, (d) 5000 , (e) EDX results of (a)

4.2.7.3 Hydrated C₃A

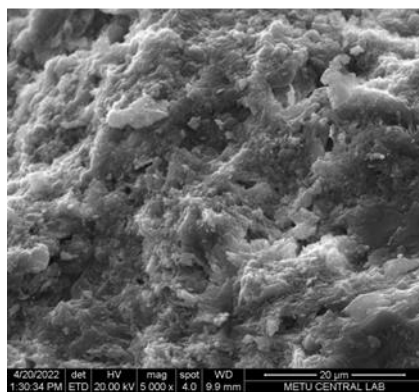
Figure 4-22 depicts SEM images of the 28-day hydrated C₃A. The results clearly indicate the formation of homogeneous calcium alumino-hydrate crystals after this hydration period. At a higher magnification (20,000 x), it becomes evident that these products exhibit an orthorhombic structure. Notably, one might anticipate the resulting material to be C₃AH₆, characterized by hexagonal plates. However, the results from the EDX test reveal varying Ca/Al ratios, ranging from 1 to 1.5 in different sample locations.



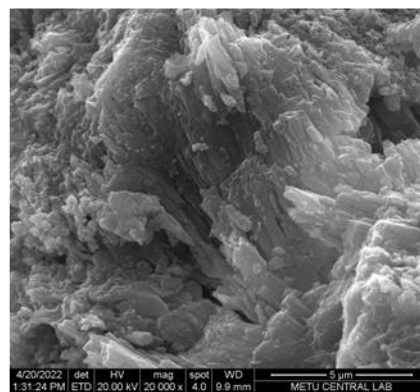
(a)



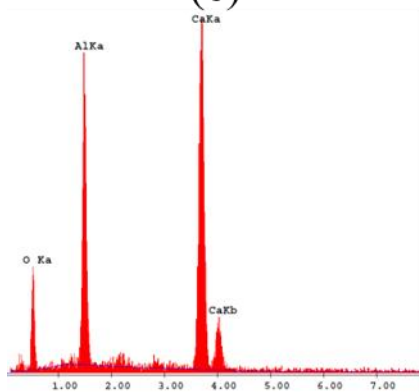
(b)



(c)



(d)



(e)

Figure 4-22 SEM images of 28- day hydrated C_3A , (a) 1000 X, (b) 5000 X, (c) 5000 X, (d) 20000 , (e) EDX results of (a)

4.2.7.4 Hydrated C₃A + Gypsum

Ettringite, a prominent hydration product resulting from the reaction of C₃A in the presence of gypsum with water, is readily discernible in the SEM images of the sample (Figure 4-23 (b)). These images also provide a depiction of the slender, needle-shaped ettringite structures, with their dimensions illustrated in Figure 4-23 (c) and (d). Furthermore, within the products of hydration, various calcium aluminate hydrates and monosulfate structures exist, characterized by both hexagonal and orthorhombic arrangements. The precise chemical formula of these structures remains elusive, primarily due to variations in the Ca/Al and Ca/S ratios.

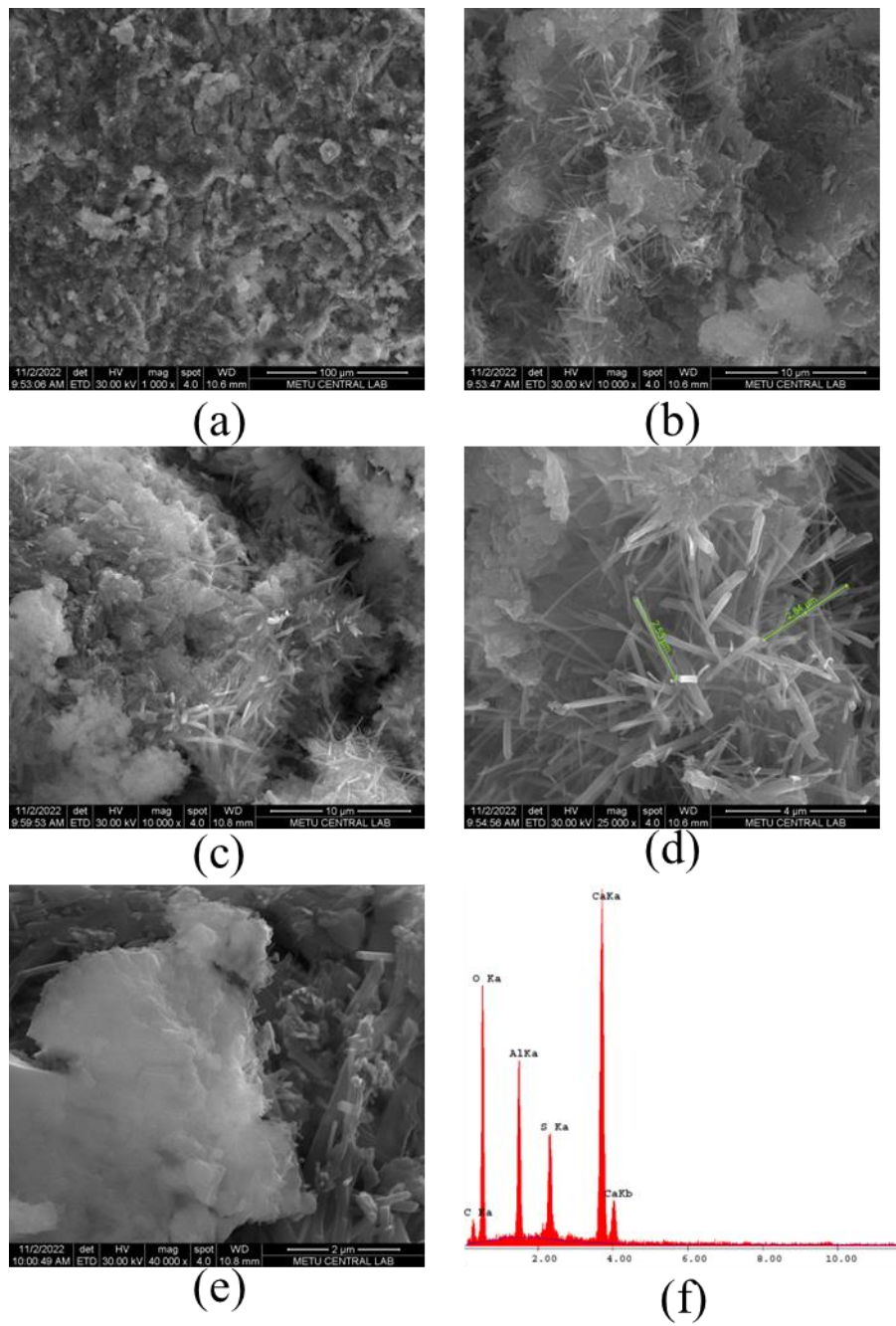


Figure 4-23 images of 28- day hydrated $C_3A + G$, (a) 1000 X, (b) 10000 X, (c) 10000 X, (d) 25000 X, (e) 40000 X, (f) EDX results of (a)

4.3 Hyperspectral Imaging Results

4.3.1 General

The results of hyperspectral imaging for cement compounds were examined in two modes of analysis: *i*) transmittance and *ii*) reflectance. Different sample preparation techniques were used for each mode, with thin sections used for the transmittance mode and polished sections used for the reflectance mode..

4.3.1.1 Transmittances mode

Images acquired using a hyperspectral camera in transmittance mode are presented in Figure 4-24. These images reveal challenges in distinguishing between particles, particularly noting the difficulty in characterizing synthetic resin due to its pronounced hardness in this mode. Furthermore, the initial materials, existing in a powder form, posed difficulties in achieving a perfectly smooth surface for precise microscope focusing on the thin sections. Notably, the presence of glue and glass components introduced additional interference, impacting the ability to discern the characteristics of the pure material. Consequently, in light of these complexities and challenges observed in the results, the investigation proceeded by employing the reflectance mode of the hyperspectral microscope.

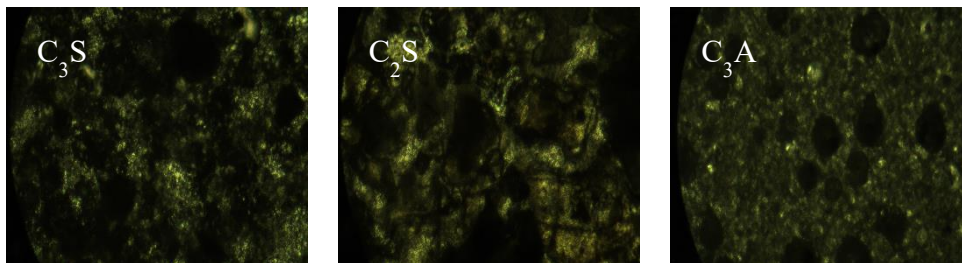


Figure 4-24 Transmittance mode hyperspectral image results for cement compounds

4.3.1.2 Reflectance mode

Prepared polish sections are used for measuring the reflectance ratio measurements. Total of 10 random readings from each sample are gathered as it is shown in Figure 4-25.



Figure 4-25 Locations of 10 random readings from polished sections

The hyperspectral camera's microscopic view enables the detection of all pores and resin material. In Figure 4-26, a microscopic hyperspectral image of C_2S at 10x magnification is presented, with a distinct color coding for each compound. The blue area corresponds to C_2S , the red area represents silicon material, and the green area indicates the presence of aluminum paste. This advanced hyperspectral imaging technology allows for detailed and accurate identification of the individual cement compounds based on their unique spectral characteristics. A total of 150 readings were conducted for each sample, and the average results for each cement compound clinker were determined and depicted in Figure 4-27.

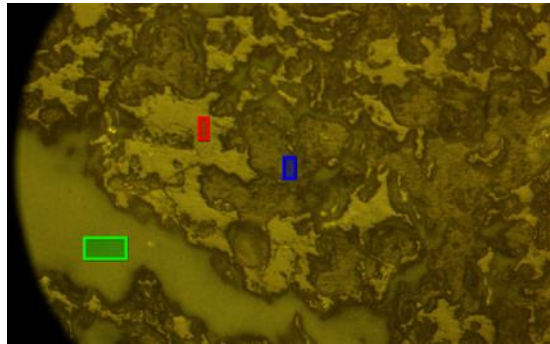


Figure 4-26 Microscopic HSI of C₂S with 10x magnification

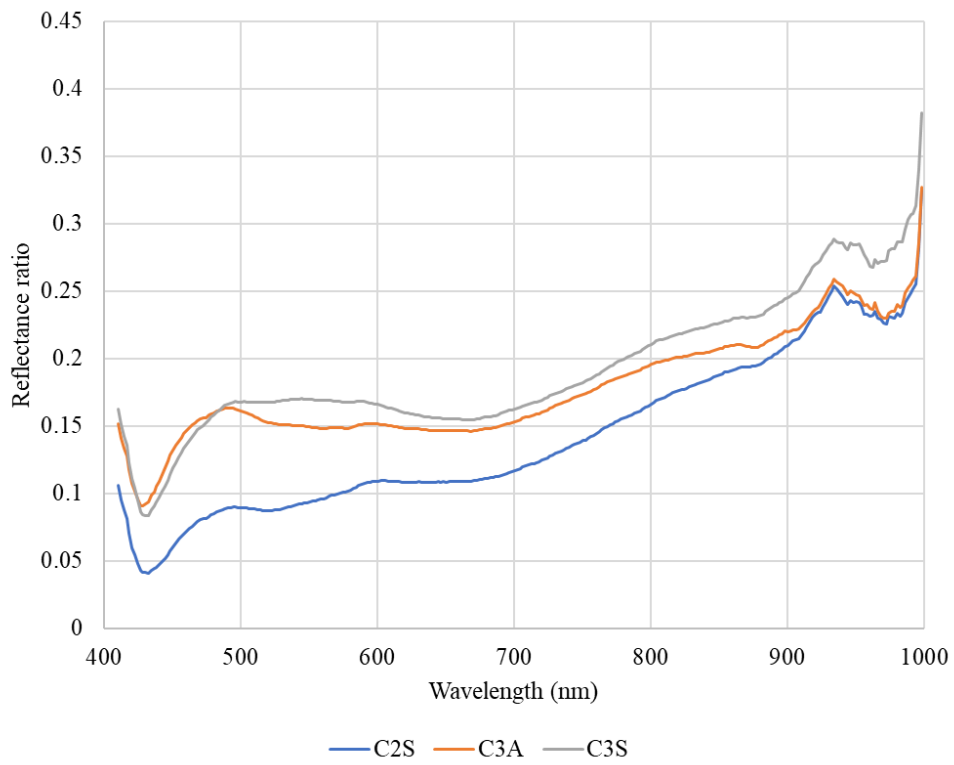
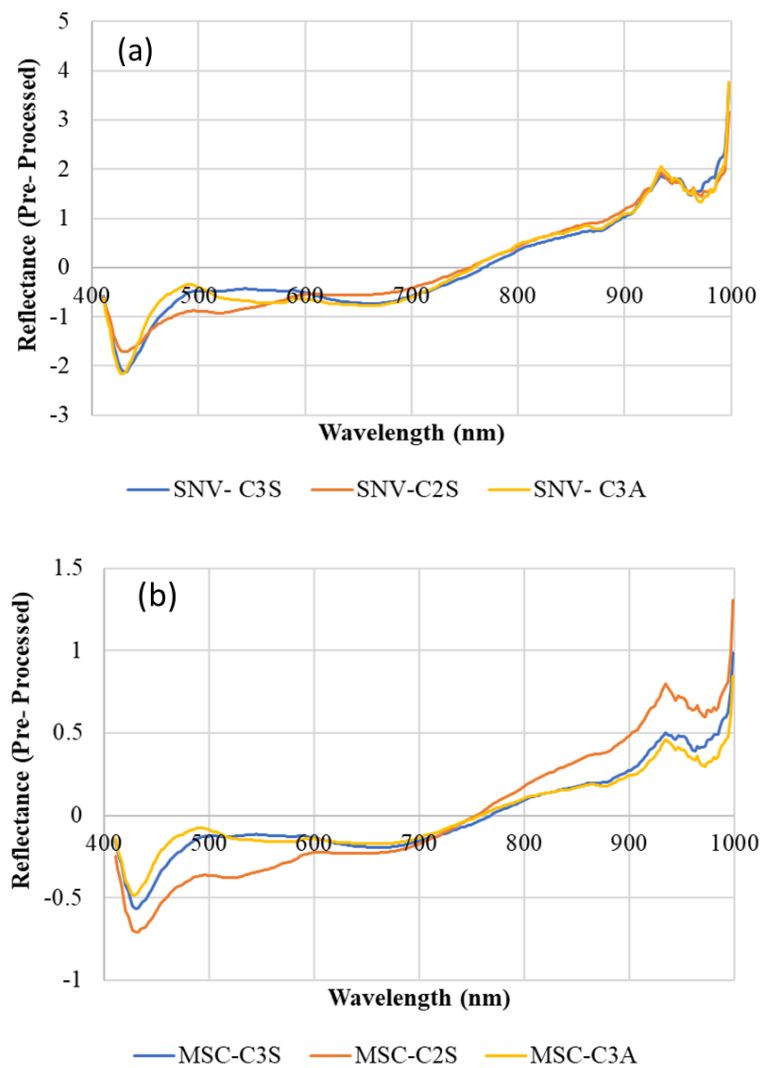


Figure 4-27 Hyperspectral imaging results of cement clinker compounds

4.3.1.3 Pre-Processing method

Standard Normal Variate (SNV), Multiplicative signal correction (MSC), derivative methods which are the most commonly used preprocessing methods are applied for extracting the hyperspectral signature of raw data. This filtering process serves the purpose of smoothing the data and mitigating noise effects arising from variations in microscope zoom levels and light scattering impacts. The results of applied pre-processing techniques are shown in Figure 4-28.



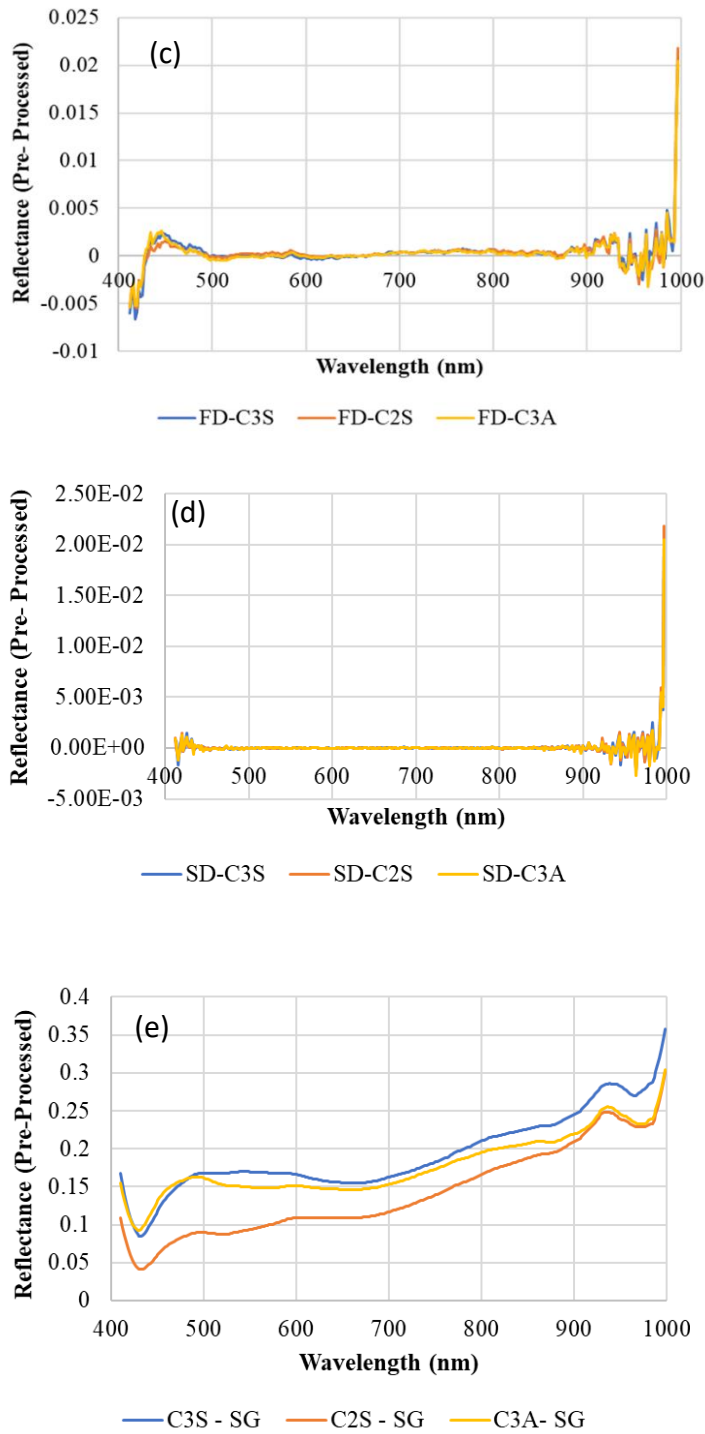


Figure 4-28 Results of applied preprocessing methods to the raw data (a) SNV, (b) MSC, (c) first order derivatives, (d) second order derivatives, (e) Savitzky-Golay

Following the application of the filters, Savitzky-Golay pre-processing method is chosen for further steps of analyzes for extracting the wavelengths corresponding to local minima and maxima.

4.3.1.3.1 C₃S Clinker

The outcomes of the preprocessed data are visually depicted in the Figure 4-29. Based on the findings, the hyperspectral signature of C₃S reveals the presence of seven local maxima and eight local minima. The enumerated list of these peaks is documented in Table 4-8. Among these peaks, 10 of them lies in the near infrared region of the electromagnetic spectrum, i.e. greater than 750 nm.

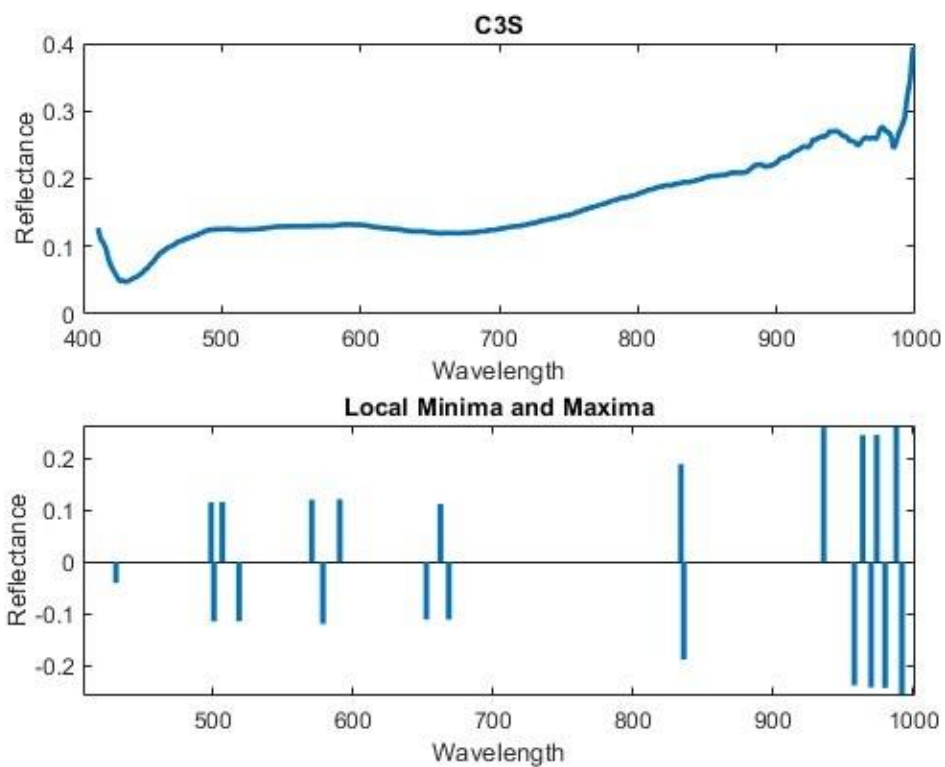


Figure 4-29 Pre-processed data and determination of local minimum and maximum for C₃S

Table 4-8 Positions of local minima and maxima for pre-processed data of C₃S

C ₃ S	
Positions of Maximums (nm)	Positions of Minimums (nm)
500.6388	423.6983
512.3498	503.4810
574.5023	532.9324
588.5789	578.5857
671.7640	666.5258
838.4091	684.8195
934.3435	841.1872
964.6085	958.8722
978.8403	971.2884
989.6259	987.8099
	991.2681

4.3.1.3.2 C₂S Clinker

The identical pre-processing methodology is applied to C₂S. The outcomes of the peak determination are presented in both the Figure 4-30 and Table 4-9. In the preprocessed data of C₂S, a total of 16 peaks were identified, comprising 8 local maxima and 8 local minima. Although C₂S and C₃S share similar components (Ca, Si), distinct variations in their spectral signatures are evident. Specifically, C₃S

exhibits a notable abundance of peaks within the spectral ranges of 500-600 nm and 900-1000 nm. In contrast, for C₂S, the prevalence of peaks is more pronounced within the range of 600-700 nm.

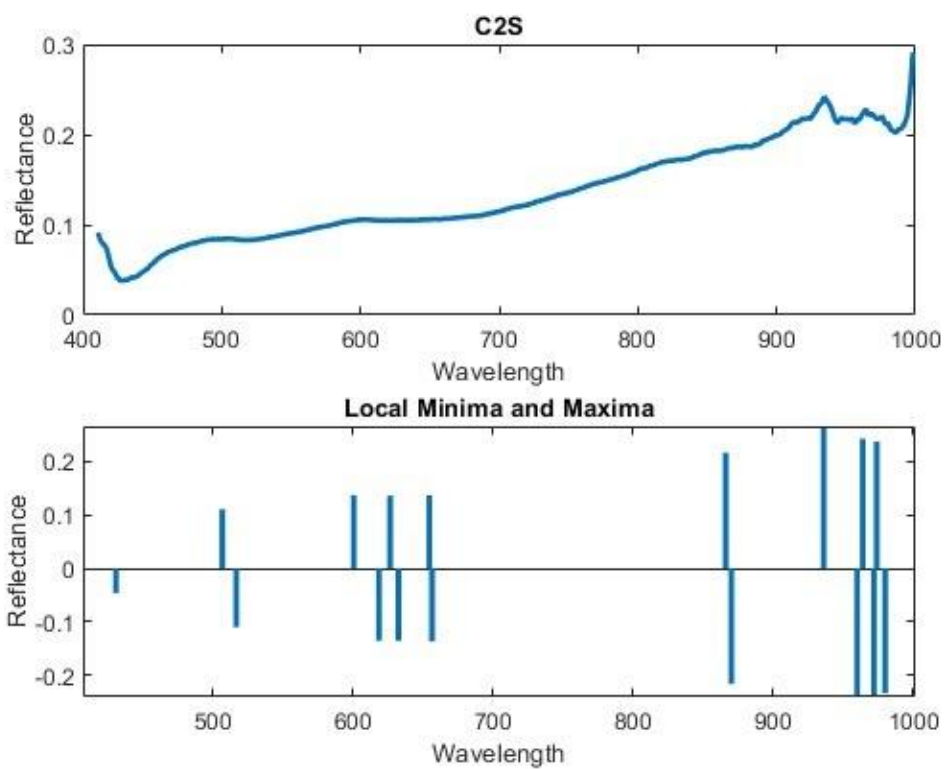


Figure 4-30 Pre-processed data and determination of local minimum and maximum for C₂S

Table 4-9 Positions of local minima and maxima for pre-processed data of C₂S

C ₂ S	
Positions of Maximums (nm)	Positions of Minimums (nm)
508.72	425.53
601.91	511.63
630.55	624.55
662.79	668.41
872.36	874.32
941.51	967.36
973.59	978.09
982.63	986.59

4.3.1.3.3 C₃A Clinker

The hyperspectral signature results for C₃A are illustrated in both Figure 4-31 and Table 4-10. A total of 19 peaks were discerned in this dataset, with 4 of these 19 peaks falling within the 500-600 nm range.

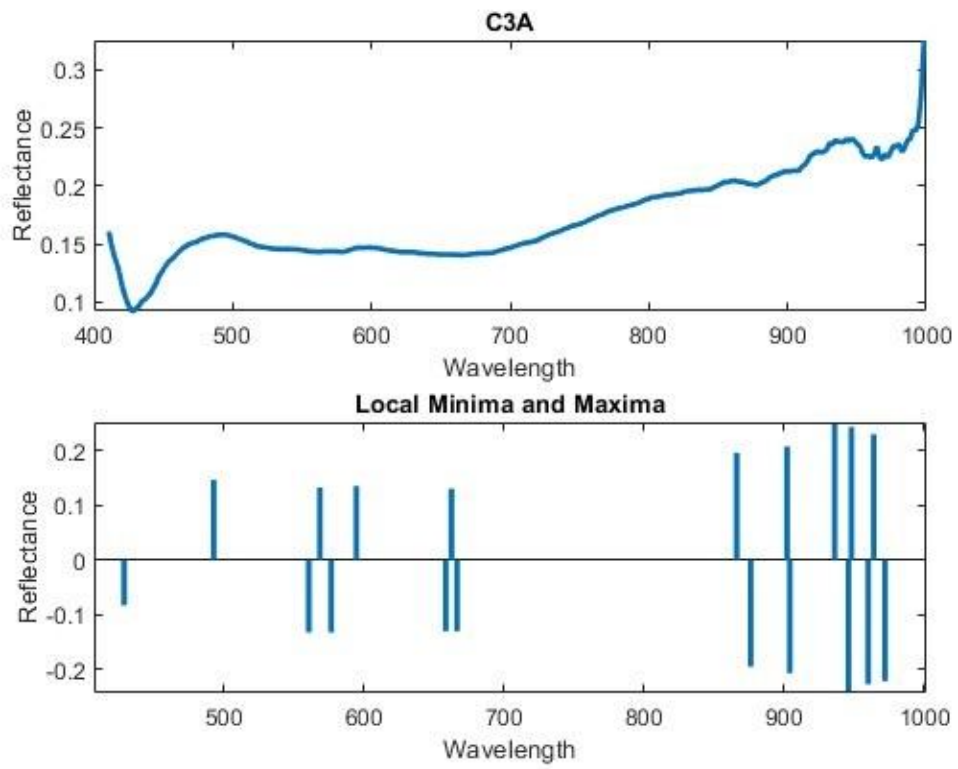


Figure 4-31 Pre-processed data and determination of local minimum and maximum for C₃A

Table 4-10 Positions of local minima and maxima for pre-processed data of C₃A

C ₃ A	
Positions of Maximums (nm)	Positions of Minimums (nm)
492.64	423.32
568.59	561.49
594.57	576.51
671.24	664.52
874.93	670.91
901.71	884.08
938.74	904.61
946.61	942.42
968.43	961.81
	971.69

4.3.2 Ground Portland Cement Clinker Compounds

4.3.2.1 Comparison of Matlab Model and Hyperspectral Imaging Results

To check the ability of the HSI setup used in this study to classify the cement compounds, powdered forms of clinkers were mixed in specific ratios (C₃S = 60 %, C₂S = 30%, C₃A = 10%) to create a sample with a specific blend of compounds. The categorization of the main compounds of cement clinker was performed using the Truscope software, which was integrated with the camera. The software's capabilities allowed for efficient and accurate analysis of the hyperspectral data, facilitating the classification of cement compounds based on their spectral characteristics. The spectrum that represents the average results of each cement compound was loaded into the software. The combination of advanced hyperspectral

imaging with the Truscope software provided a reliable and effective approach for the identification and categorization of cement clinker samples.

Table 4-11 comparison of real mixed ratio and HSI classification results

Cement compound	Ratio in the mixture	Average of HSI readings
C ₃ S	60.0 %	61.6%
C ₂ S	30.0 %	27.4%
C ₃ A	10.0 %	10.3 %

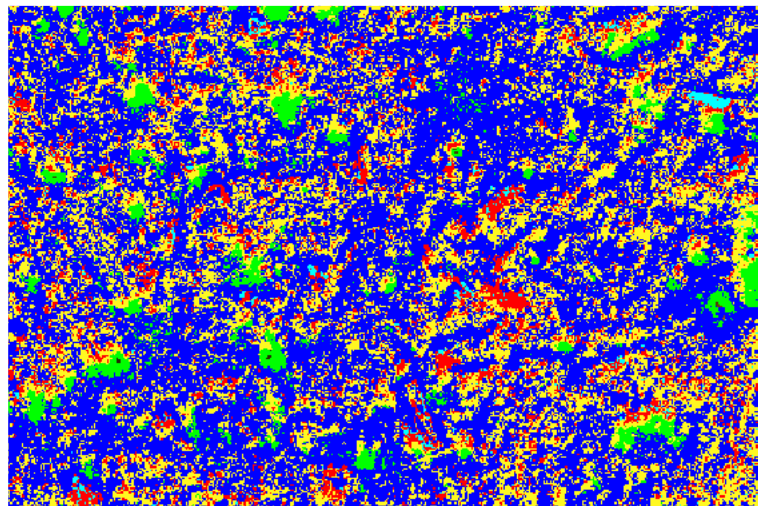


Figure 4-32 Classified hyperspectral image of C₃S, C₂S and C₃A

The Deep Learning Toolbox in Matlab was used to design and implement deep neural networks to train, test, and create classification functions, for checking the validity of the data obtained from the truscope software. First, the training process was performed against 11 different model types, as listed in Table 4-12. These

models were among the most used ones in literature. While one of the models failed the prediction, four other models gave a high accuracy (over 90%). The validation process was performed on the test dataset after that, to check the accuracy of the created model. Finally, the model with the highest accuracy test result (No 11, Kernel Logistic Regression) was selected and converted into a Matlab function. The validation confusion matrix of the selected models is presented in Figure 4-33.

Table 4-12 Summary results of Deep Learning process

Model Type	Status	Accuracy % (Validation)	TotalCost (Validation)	Accuracy % (Test)	Total Cost (Test)
Quadratic Discriminant	Failed	NaN	NaN	NaN	NaN
Efficient Logistic Regression	Tested	25.00	90	39.75	241
Guassian Naive Bayes	Tested	83.33	20	81.5	74
Linear SVM	Tested	96.67	4	96.25	15
Medium Guassian SVM	Tested	94.17	7	96.25	15
Medium KNN	Tested	88.33	14	88	48
Coarse KNN	Tested	25.00	90	29.25	283
Cosine KNN	Tested	88.33	14	89.25	43
Ensemble	Tested	25.00	90	25	300
Trilayered Neural Network	Tested	95.83	5	97.5	10
Kernel Logistic Regression	Tested	93.33	8	98.25	7

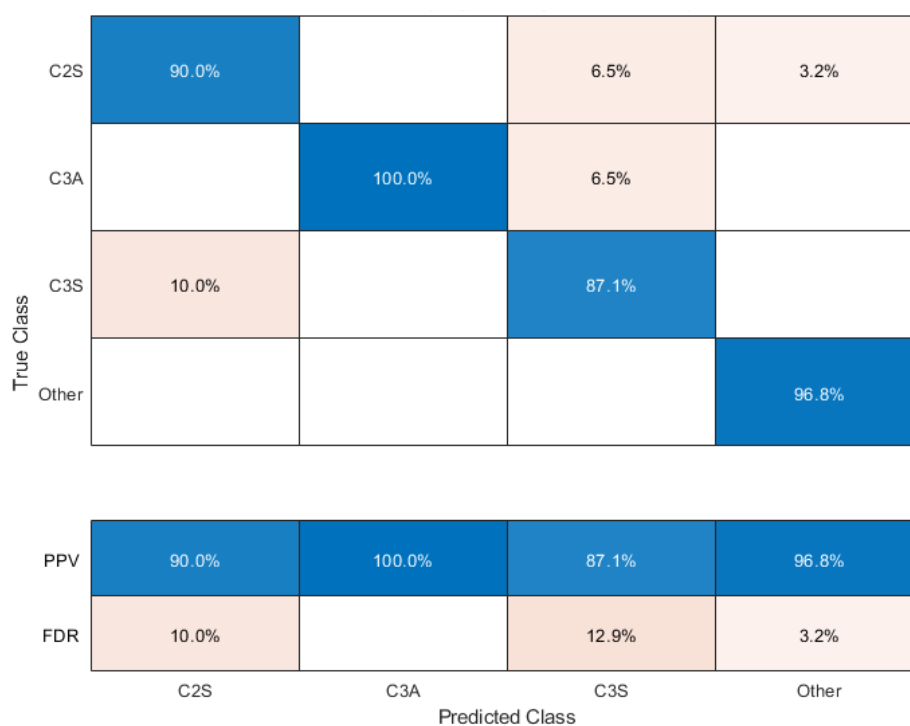


Figure 4-33 The validation confusion matrix of Kernel Logistic Regression model (PPV: Positive Predictive Values, FDR: False Discovery Rates)

4.3.3 Analysis of an Industrial Clinker

After evaluating the individual cement compounds, an industrially produced clinker sample was procured for analysis. Initially, the selected clinker underwent assessment using conventional methodologies. These tests are conducted in the R&D Laboratories of the Turkish Cement Manufacturers' Association (TURKCIMENTO). Subsequently, hyperspectral imaging was employed in the subsequent phase to further characterize the sample for comparison purposes.

4.3.3.1 X-ray Diffraction Analysis of the Industrial Clinker

The results of XRD analysis for this cement clinker is presented in Figure 4-34. According to the results of XRD presence of C_3S , C_2S and C_3A is confirmed in the sample.

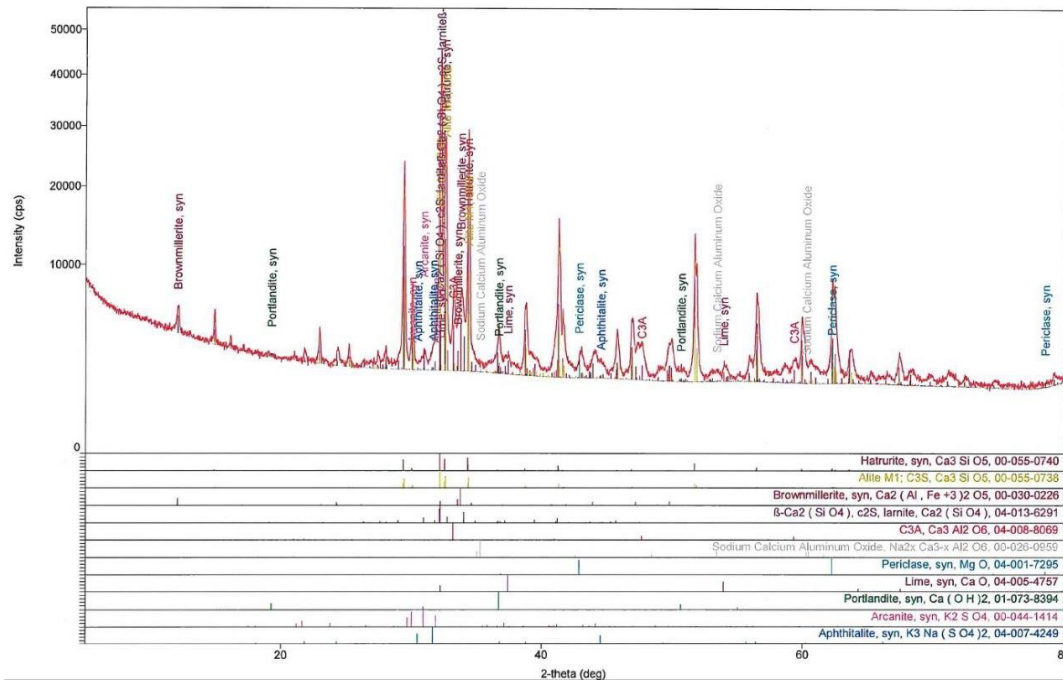


Figure 4-34 Results of XRD analysis for industrial clinker sample

Additionally, employing the Rietveld model facilitated the computation of the quantities of each compound. According to the obtained results, the total proportions of C_3S , C_2S , and C_3A are determined to be 64.0%, 17.4%, and 6.3%, respectively as they are listed in Table 4-13.

Table 4-13 Rietveld results for the industrial clinker

Compounds	Percentage
C ₃ S	64.0 %
C ₂ S	17.4 %
C ₃ A	6.3 %
C ₄ AF	10.4 %
MgO	1.0 %
CaO	0.6 %
Ca(OH) ₂	0.1 %
K ₂ SO ₄	< 0.1 %
K ₃ NaSO ₄	0.2 %

4.3.3.2 Analysis by Bogue's Equation

The chemical analysis results of the clinker, and the quantities of individual compounds that were determined using the Bogue's equations are presented in Figure 4-14.

Table 4-14 Chemical Analysis and the Compound Composition of the Clinker

Parameter	Analysis Result (%)	Compound	Analysis Result (%)
SiO ₂	20.73	C ₃ S	67.13
Al ₂ O ₃	4.99	C ₂ S	8.84
Fe ₂ O ₃	3.20	C ₃ A	7.81
CaO	65.03	C ₄ AF	9.74
MgO	2.07		
SO ₃	1.69		
Na ₂ O	0.52		
K ₂ O	0.76		
Cl ⁻	0.0198		
Free CaO	0.47		
Loss on Ignition	0.13		

4.3.3.3 Optical Polarized Light Microscope Analysis

As an additional step in the classification of compounds within the clinker sample, optical polarized light microscopic tests were conducted. In this test the ratio of each compound was determined by enumerating the quantity of individual crystals and measuring the dimensions of their respective crystals. The visual representation of these samples under the optical polarized light microscope is shown in Figure 4-35. Applied magnification is 100x for all those pictures. Brown-hued crystals correspond to C_3S , while the blue-hued crystals are indicative of C_2S . The crystal structures associated with C_3A are not discernible at this magnification level, but in Figure 4-35 (c) the sample is shown with 500x magnification and the crystals of C_3A could be detectable in gray color on the cream color background. Figure 4-36 shows the size distribution data for both C_3S and C_2S .

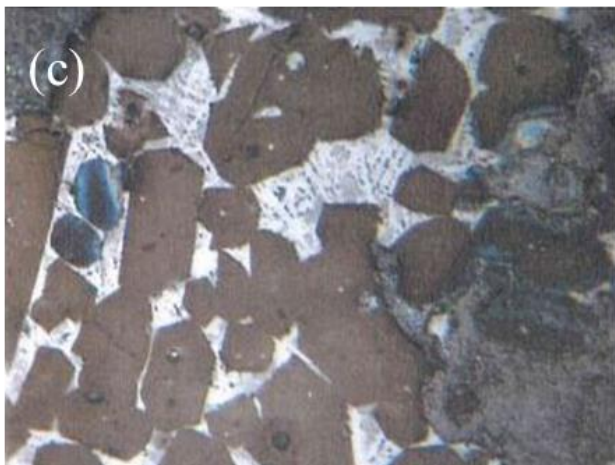
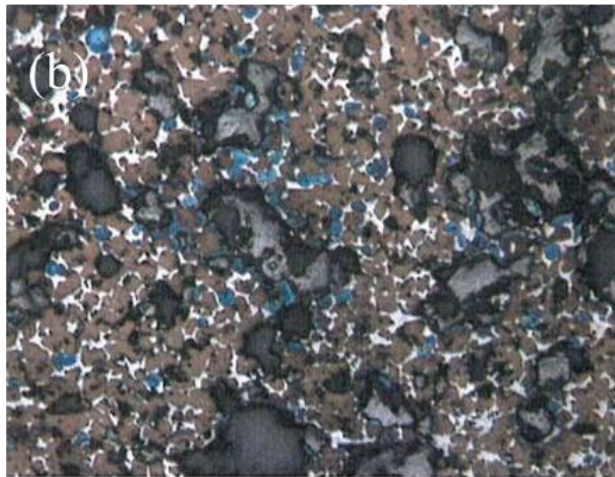
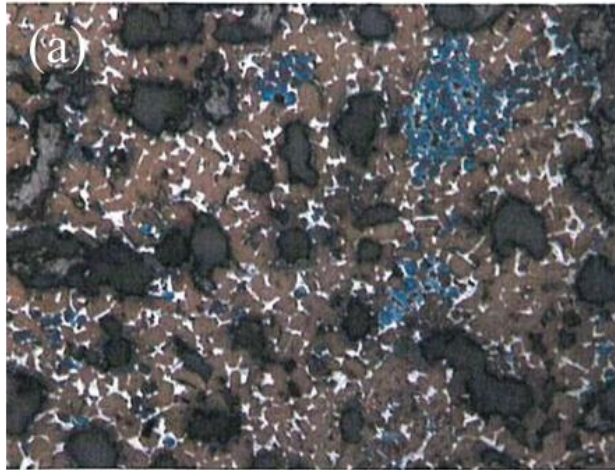


Figure 4-35 (a) and (b) Crystals of C₃S (brown) and C₂S (blue) under light microscope with 100x magnification, (c) Crystals of C₃A, gray crystals on a cream background under 500x magnification

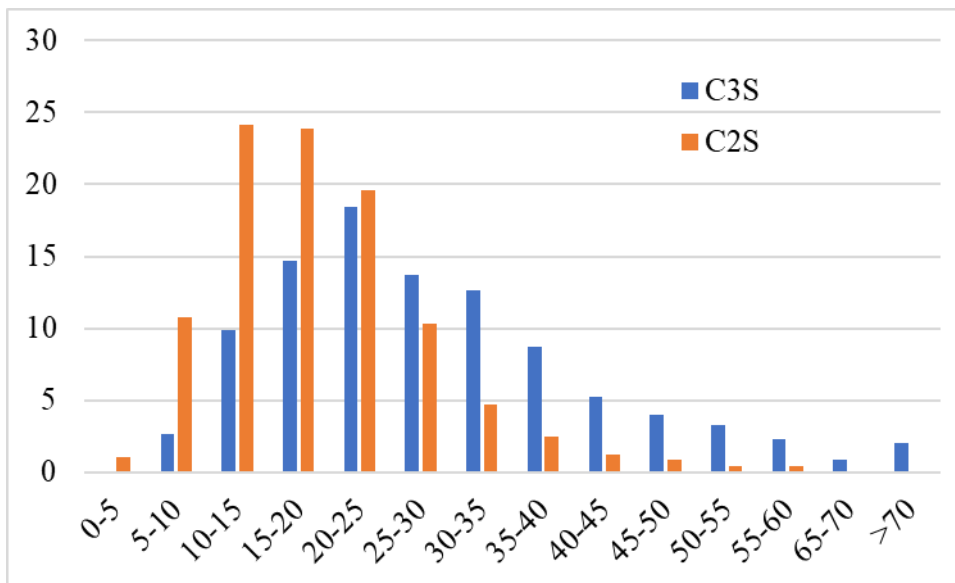


Figure 4-36 Crystal size distribution for C₃S and C₂S

In accordance with the findings, the ratios of each compound are documented in Table 4-15. As per these outcomes, the determined ratios for individual compounds based on light microscopic phase detection are as follows: 63.38% for C₃S, 22.15% for C₂S, and 14.47% for the combined content of C₃A + C₄AF. It is noteworthy to mention that the discrete quantification of the total amounts of C₃A and C₄AF was not feasible using this method.

Table 4-15 Results of optical polarized light microscope phase detection

Cement compound	Percentage
C ₃ S	63.38 %
C ₂ S	22.15 %
C ₃ A+C ₄ AF	14.47 %

4.3.3.4 Hyperspectral results of industrial clinker

The function generated in Matlab for classifying the cement compound is applied for the industrial clinker. The Kernel Logistic Regression model was used for this purpose. The same sample was classified using the HSI test setup. The classification was performed on a dataset taken from the Hyperspectral Cube, which contains 65044 readings. The results obtained from the hyperspectral camera categorization are presented in Figure 4-37. Based on the analysis and the provided data, the red areas in the image are associated with C_3S , while the dark blue regions represent C_2S . The green areas correspond to C_3A , and the light blue parts indicate the presence of pores, which were filled with aluminum paste during the polishing process.

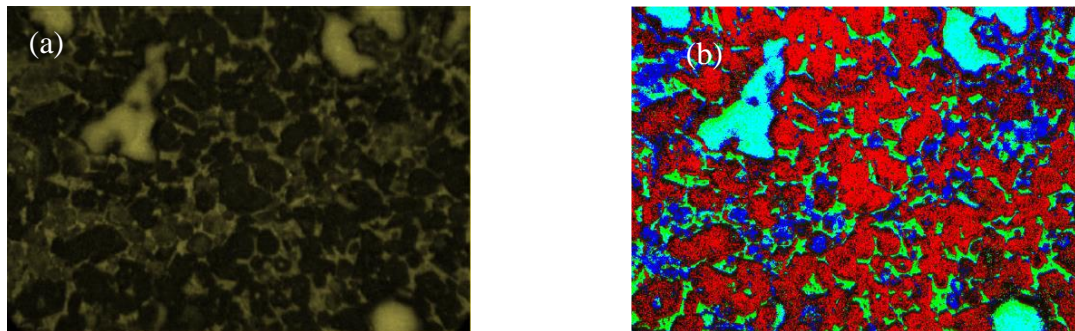


Figure 4-37 (a) Hyperspectral image of cement, (b) categorized cement clinker

The classification results of the generated model and the quantitative results taken from the HSI setup are presented in Table 4-16.

Table 4-16 Classification results of the generated model and the quantitative results taken from the HSI setup.

Cement compound	Analysis Result (%)	
	Matlab model	HSI
C ₃ S	58.6%	59.9%
C ₂ S	23.0%	22.1%
C ₃ A	8.8%	9.3%
Other	9.6%	8.7%

4.3.3.5 Comparison of classifications with different methods

The categorization of industrial clinker involved employing various methodologies, and this section presents a comparative analysis of the outcomes obtained through each method in relation to hyperspectral imaging. The results are delineated in Table 4-17 for comprehensive examination.

Table 4-17 Comparison of classification results for different methods of testing

Cement Compound	Conventional Methods			Matlab Model	HSI
	Rietveld	Optical Polarized Light Microscope	Bogue Equations		
C ₃ S (%)	64.0	63.4	67.13	58.6	59.9
C ₂ S (%)	17.4	22.2	8.84	23.0	22.1
C ₃ A (%)	6.3	-	7.81	8.8	9.3
Other (%)	12.3	14.5	9.74	9.6	8.7

In light of the obtained findings, the hyperspectral imaging method demonstrated an accuracy of 72.98% with Rietveld method. Conversely, the light microscope method exhibited a notably higher accuracy rate of 97.14%, while the application of Bogue equations yielded an accuracy of 85.07%. Additionally, the developed Matlab functions showcased a commendable accuracy of 96.06%.

4.3.4 Hyperspectral Imaging Results of Hydrated Cement Clinker Compounds

Hyperspectral images of hydrated cement compounds were obtained from their polished surfaces. The average of 130 readings are gathered for each compound.

4.3.4.1 Hydrated C₃S

As can be seen from Figure 4-38, When the absorbance of the hydrated C₃S clinker is compared with the 1-day hydrated compound it is evident that there is a reduction in the reflectance below 750 nm, and after that a general increase is observed with the formation of some peaks and valleys. As the hydration continues to 7 days the the reflectance further decreases. At 28 days however, there is a remarkable increase in the reflectance ratio.

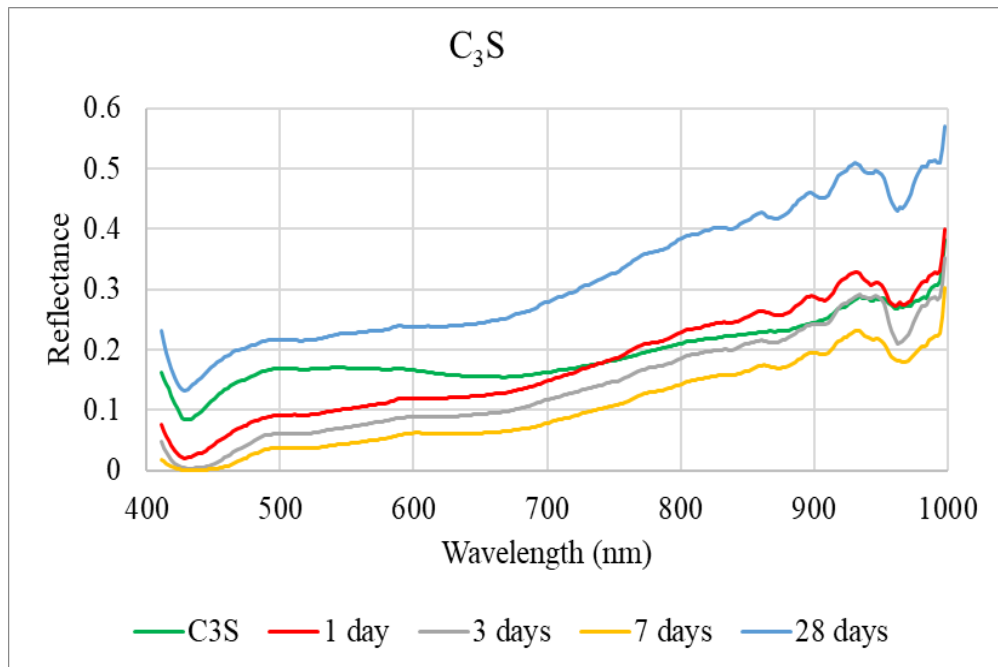


Figure 4-38 Average of hyperspectral data recordings from hydrated C₃S after 1, 3, 7, 28 days

4.3.4.2 Hydrated C₂S

Figure 4-39 illustrates the mean hyperspectral readings for both C₂S and its hydrated form. The findings indicate that, following a single day of hydration, there is an elevation in the reflectance ratio beyond the 600 nm wavelength, coupled with a reduction preceding the 600 nm as compared to the unhydrated C₂S. After a span of seven days, the reflectance ratio demonstrates a considerable resemblance to that of the unhydrated C₂S. However, the data obtained at the 28-day mark reveals a significant increase in the reflectance ratio.

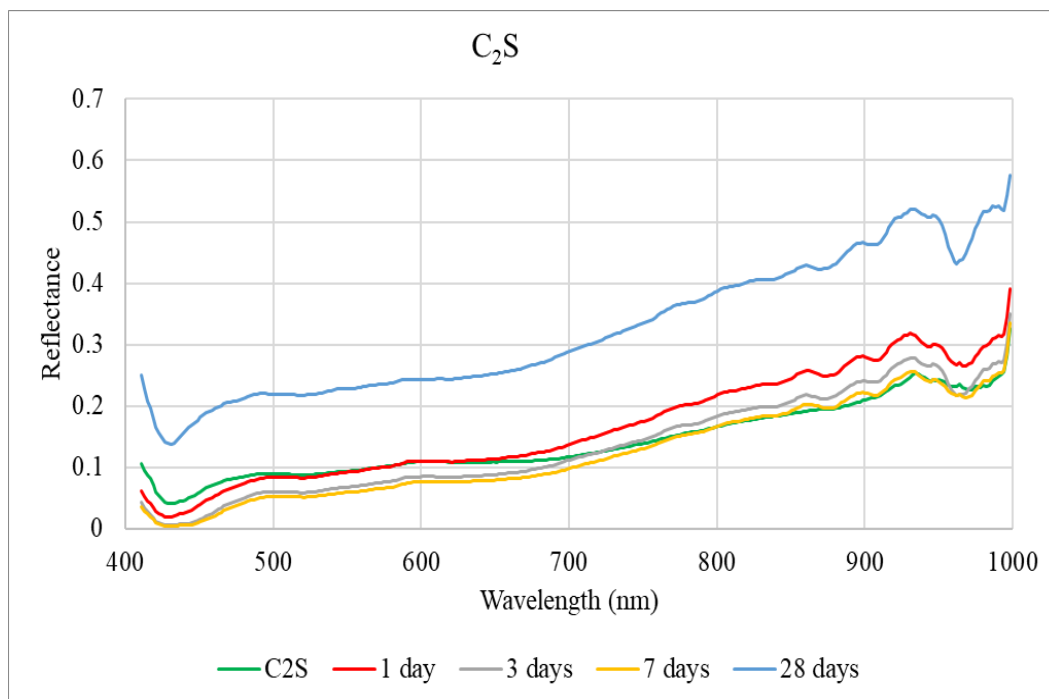


Figure 4-39 Average of hyperspectral data recordings from hydrated C₂S after 1, 3, 7, 28 days

4.3.4.3 Hydrated C₃A

In the case of C₃A, the evolution of absorbance follows a pattern analogous to that of C₂S as it is shown in Figure 4-40. Subsequent to a single day of hydration, there is a decline in the reflectance ratio preceding 700 nm, coupled with an elevation beyond 700 nm. Following three days, a further reduction in absorbance ratio is observed before 700 nm in comparison to the compound hydrated for one day, and before 870 nm when contrasted with the unhydrated C₃A; however, an increase is discernible beyond these wavelengths. After seven days of hydration, the reflectance pattern closely aligns with that observed after one day of hydration. Similar to other cement compounds, a conspicuous escalation in the reflectance ratio is noted after 28 days of hydration.

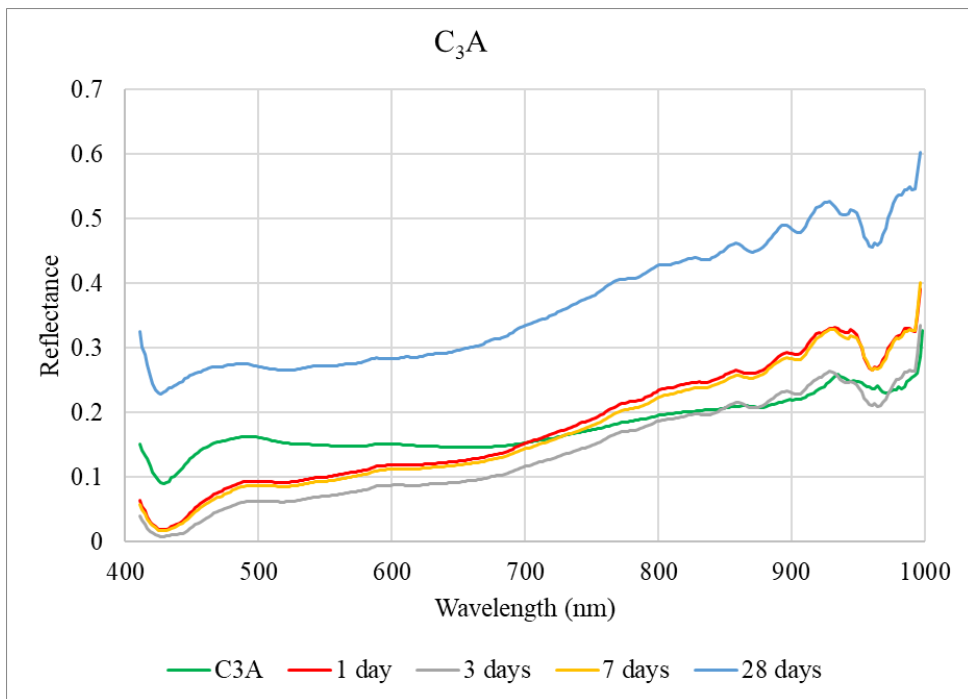


Figure 4-40 Average of hyperspectral data recordings from hydrated C₃A after 1, 3, 7, 28 days

4.3.4.4 Pre-Processed hyperspectral data for hydrated compounds

The results of Savitzky-Golay preprocessed are shown in Figure 4-41. According to this preprocessing the data gets smoother and the noise from light scattering is eliminated from the results. In all cases the reflectance ratio decreases in first 7 days of hydration, and then increase in 28 day measurements in pre-processed data.

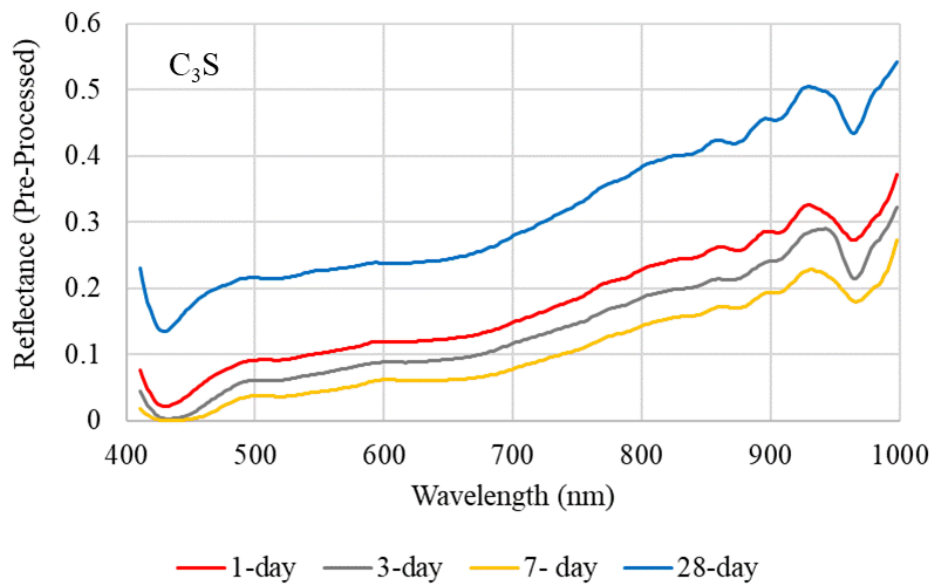


Figure 4-41 Preprocessed hyperspectral data for (a) C₃S, (b) C₂S and (c) C₃A

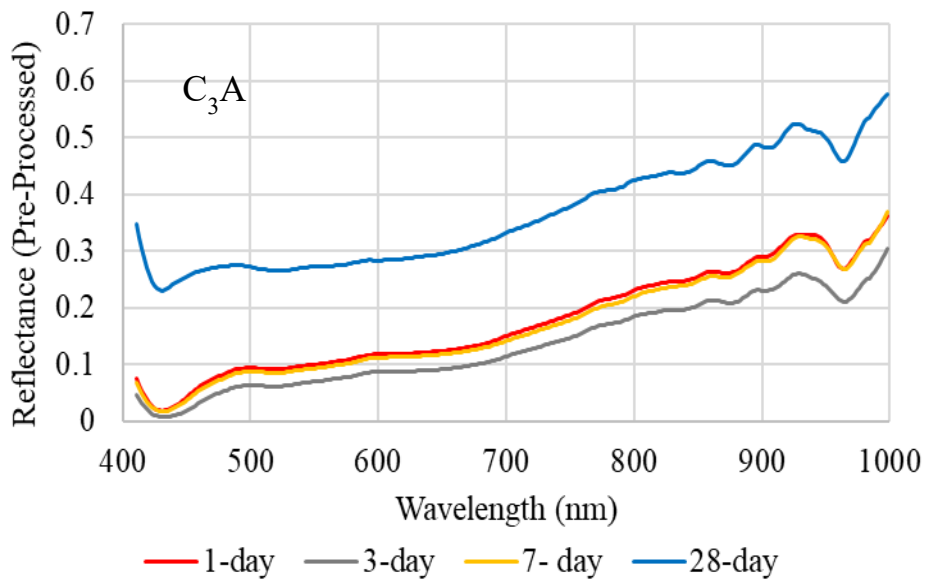
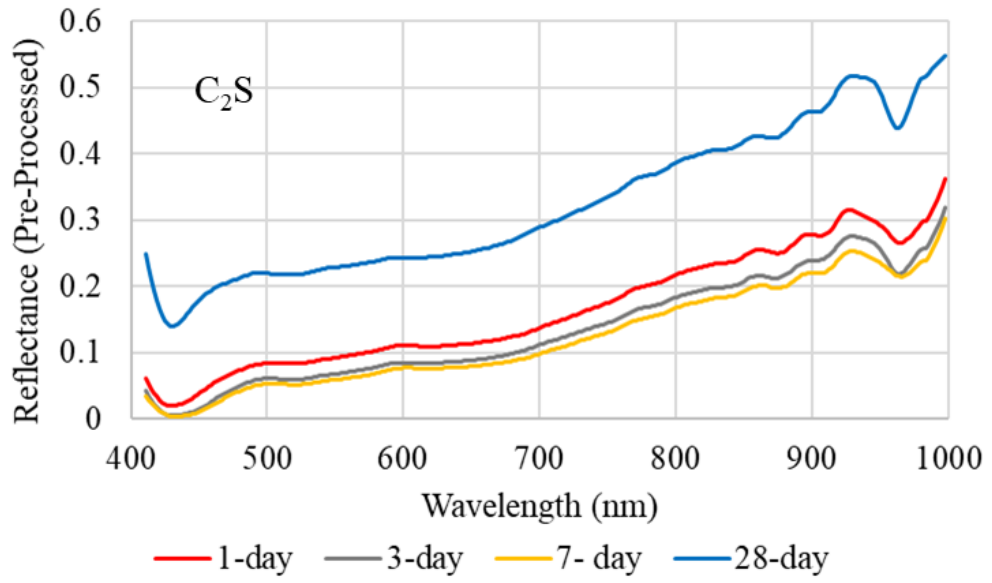


Figure 4- 41 Continued

CHAPTER 5

SUMMARY, CONCLUSIONS AND RECOMMENDATIONS

The main objective of this study is to investigate the technical feasibility of utilizing hyperspectral imaging (HSI) to characterize features of Portland cement. To achieve this, a comprehensive experimental program is designed, commencing with the successful synthesis of Portland cement compounds. Following synthesis, these compounds undergo characterization using well-established traditional methods such as XRD and SEM. The acquisition of hyperspectral images for these compounds and the use of various pre-processing techniques for identification marks the completion of the first phase of the experimental program.

In the second phase, the synthesized compounds are ground and blended to produce typical ordinary Portland cement. The compounds within this blend are identified using previously generated hyperspectral images of each individual compound. As part of this phase the compound composition of an industrially produced clinker sample is also analyzed through conventional techniques as well as HIS, and the developed mathematical model was applied to identify the compound composition for this clinker.

In the third and final phase of the experimental program, the hydration characteristics of the Portland cement compounds are investigated using HSI in conjunction with traditional characterization methods, including isothermal calorimetry, XRD, FTIR, and microstructural characterization through SEM. Additionally, the mechanical properties of each compound, specifically compressive strength, and modulus of elasticity, are determined.

According to the experimental test results, the following conclusions could be drawn:

- The synthesis of pure Portland cement compounds and their identification by XRD analysis is a difficult process. The use of XRD analysis alone could lead to the misidentification of the two calcium silicate phases. Therefore, the required phase formation depends on rapid quenching and the selection of appropriate chemical stabilizers. In addition to XRD analysis, isothermal analysis and microstructural characterization are essential for the identification of these phases. According to these analyses, the heat generation in cement comes mainly from C_3A in the presence of gypsum, followed by C_3S . During hydration, C_3S is responsible for early age strength, contributing to a 40 MPa increase in strength, while C_2S becomes more influential in the 90 to 180 day period, achieving a 70 MPa gain. In addition, microstructural analysis indicates that C_3A has a more crystalline structure, while C_2S is denser than C_3S , which is denser than C_3A .
- At the microscopic scale, hyperspectral imaging appears to be an affordable and promising tool for the identification of Portland cement compounds. This experimental thesis program marks the initial phase in the development of such an identification tool.
- Among the two investigation modes, the reflectance mode seems to be more preferable over the transmittance mode, and among the various preprocessing analysis methods of the hyperspectral image data, the Savitzky-Golay preprocessing method yielded the most effective results for the classification of the Portland cement compounds.
- When the Savitzky-Golay pre-processing method is used for extracting the wavelengths corresponding to local minima and maxima of each hyperspectral image data, the results indicate that C_3S exhibits 21 peaks, C_2S has 16, and C_3A has 19 local peaks, each contributing to the characterization of the hyperspectral signature for the respective compound.
- In the context of ground and blended clinker compounds, when the developed mathematical model was used for the classification of each compound, an average accuracy of 95% was obtained. Therefore, it can be concluded that

the local maxima and local minima obtained can be successfully used to identify the cement compounds within a blend.

- It should be mentioned that the classification of the cement compounds for the industrial clinker, using the conventional techniques brings some discrepancy in the results. This is attributed first of all to the underlying assumptions used in applying these methods such as the use of Bogue's equations and the Rietveld method, and to the heterogeneity of the clinker sample in the microscopic range. When the compound classification is performed by the hyperspectral image acquisition process developed in this thesis, the overall accuracy was about 73% with respect to the Rietveld method and 85% with respect to the use of Bogue's equations. On the other hand, when compared to the polarized optical light microscopy the accuracy increased to 97%, as the same polished section was used in the analysis.
- Finally, for the hydrated phases of the Portland cement compounds the addition of water reduces the reflectance of all compounds at the visible part of the electromagnetic spectrum and increases the reflectance in the near infrared part, as observed from the 1-day through 7-day hyperspectral data. On the other hand when the measurements are made on the 28-days, a significant increase in the reflectance at all wavelengths was observed for all of the cement compounds, which requires further investigation.

This thesis is a first step in the use of HSI analysis in characterizing Portland cement characterization and the following recommendations will be helpful for future studies:

- The use of hyperspectral imaging on a microscopic scale requires some extra work on the side of specimen preparation. The main reason for that is the high surface flatness needed to allow the microscope to focus on the specimen. Therefore, expertise in specimen preparation is needed for successful utilization.

- The hyperspectral camera that was available in our laboratory covered a wavelength range of 400 nm to 1000 nm across the visible to near-infrared spectrum. As future research endeavors unfold, employing hyperspectral cameras equipped with broader wavelength coverage could prove to be beneficial for further cement compound classification and identification. This enhanced spectral range would likely facilitate even more comprehensive and accurate assessments, paving the way for advancements in the field of cement characterization and opening new avenues for exploring the unique properties of cementitious materials.
- Large scale cameras, without using the microscope could be used to investigate its accuracy in checking cement compounds categorization, to overcome the polish sample preparation for microscope. A dynamic focus area scanning system can provide a solution for this, hence reduce the time needed to prepare the specimen, which can allow for online scanning.

REFERENCES

- Adão, T., Hruška, J., Pádua, L., Bessa, J., Peres, E., Morais, R., & Sousa, J. J. (2017). Hyperspectral imaging: A review on UAV-based sensors, data processing and applications for agriculture and forestry. *Remote Sensing*, 9(11), 1110.
- Albani, J. R. (2008). *Principles and applications of fluorescence spectroscopy*. John Wiley & Sons.
- Amigo, J. M., Martí, I., & Gowen, A. (2013). Hyperspectral Imaging and Chemometrics. A Perfect Combination for the Analysis of Food Structure, Composition and Quality. In *Data Handling in Science and Technology* (Vol. 28, pp. 343–370). Elsevier Ltd. <https://doi.org/10.1016/B978-0-444-59528-7.00009-0>
- Amigo, J. M., & Santos, C. (2019). Preprocessing of hyperspectral and multispectral images. In *Data handling in science and technology* (Vol. 32, pp. 37–53). Elsevier.
- An, D., Zhang, L., Liu, Z., Liu, J., & Wei, Y. (2022). Advances in infrared spectroscopy and hyperspectral imaging combined with artificial intelligence for the detection of cereals quality. *Critical Reviews in Food Science and Nutrition*. <https://doi.org/10.1080/10408398.2022.2066062>
- Anghel, G. (2021). Possible Mistakes in Forensic Photography. *Proceedings of the 23rd International RAIS Conference on Social Sciences and Humanities*, 83–86.
- Anthony Seibert, J. (1995). One hundred years of medical diagnostic imaging technology. *Health Physics*, 69(5), 695–720. <https://doi.org/10.1097/00004032-199511000-00006>

- Arce, G. R., Brady, D. J., Carin, L., Arguello, H., & Kittle, D. S. (2014). Compressive Coded Aperture Spectral Imaging: An Introduction. *IEEE Signal Processing Magazine*, 31(1), 105–115.
<https://doi.org/10.1109/MSP.2013.2278763>
- Ariana, D. P., & Lu, R. (2008a). Quality evaluation of pickling cucumbers using hyperspectral reflectance and transmittance imaging - Part II. Performance of a prototype. *Sensing and Instrumentation for Food Quality and Safety*, 2(3), 152–160. <https://doi.org/10.1007/S11694-008-9058-9>
- Ariana, D. P., & Lu, R. (2008b). Quality evaluation of pickling cucumbers using hyperspectral reflectance and transmittance imaging: Part I. Development of a prototype. *Sensing and Instrumentation for Food Quality and Safety*, 2(3), 144–151. <https://doi.org/10.1007/S11694-008-9057-X>
- Baek, S., Kim, I., Diego Gutierrez, K., Kim, M. H., Baek, S.-H., & Gutierrez, D. (2017). Compact Single-Shot Hyperspectral Imaging Using a Prism. *ACM Trans. Graph*, 36, 12. <https://doi.org/10.1145/3130800.3130896>
- Balchin, S. (2021). Spectra. *Algebra and Applications*, 179–193.
https://doi.org/10.1007/978-3-030-75035-0_10
- Ball, D. W. (2007). The electromagnetic spectrum: a history. *Spectroscopy*, 22(3), 14.
- Bartczak, P. (2016). *Spectrally tunable light sources for implementing computationally designed illuminations*.
<https://doi.org/10.13140/RG.2.2.20484.22400>
- Bazzoni, A., Ma, S., Wang, Q., Shen, X., Cantoni, M., & Scrivener, K. (2014). The Effect of Magnesium and Zinc Ions on the Hydration Kinetics of C3S. *Journal of the American Ceramic Society*, 97. <https://doi.org/10.1111/jace.13156>

- Beck, R. N. (1990). Overview Of Imaging Science. *IEEE Nuclear Science Symposium Conference Record*, 1057–1057.
<https://doi.org/10.1109/NSSMIC.1990.693507>
- Bian, X. (2022). Spectral Preprocessing Methods. In X. Chu, Y. Huang, Y.-H. Yun, & X. Bian (Eds.), *Chemometric Methods in Analytical Spectroscopy Technology* (pp. 111–168). Springer Nature Singapore.
https://doi.org/10.1007/978-981-19-1625-0_4
- Birchall, J. D., Howard, A. J., & Bailey, J. E. (1978). On the hydration of portland cement. *Proc R Soc London Ser A*, 360(1702), 445–453.
<https://doi.org/10.1098/RSPA.1978.0078>
- Bodkin, A., Sheinis, A., Norton, A., Daly, J., Beaven, S., & Weinheimer, J. (2009). Snapshot hyperspectral imaging: the hyperpixel array camera. *In Algorithms and Technologies for Multispectral, Hyperspectral, and Ultraspectral Imagery XV*, 7334, 164–174. <https://doi.org/10.1117/12.818929>
- Bonifazi, G., Palmieri, R., & Serranti, S. (2018). Evaluation of attached mortar on recycled concrete aggregates by hyperspectral imaging. *Construction and Building Materials*, 169, 835–842.
<https://doi.org/10.1016/J.CONBUILDMAT.2018.03.048>
- Bracco, C., Regge, D., Stasi, M., Gabelloni, M., & Neri, E. (2019). Principles of CT and MR imaging. *Nuclear Medicine Textbook*, 187–198.
https://doi.org/10.1007/978-3-319-95564-3_8
- Brelstaff, G., Párraga, A., Troscianko, T. , & Carr, D. (1995). Hyperspectral camera system: acquisition and analysis. *Photogrammetry, and Geological/Geophysical Remote Sensing, Vol. 2587, Pp. 150-159. SPIE*, 150–159.
- Bruning, B., Berger, B., Lewis, M., H Liu, & Garnett, T. (2020). Approaches, applications, and future directions for hyperspectral vegetation studies: an

- emphasis on yield-limiting factors in wheat. *The Plant Phenome*, 3(1).
<https://doi.org/10.1002/ppj2.20007>
- Bullard, J., Jennings, H., Nonat, A. , Scherer G. W., SchweitzerJ. S., ... &, & Thomas, J. J. (2011). Mechanisms of cement hydration. *Cement and Concrete*.
- Bye, G. (1999). *Portland cement: composition, production and properties*. Thomas Telford.
- Vaiphasa, C. (2006). Consideration of smoothing techniques for hyperspectral remote sensing. *ISPRS Journal of Photogrammetry and Remote Sensing*.
- Calin, M. A., Calin, A. C., & Nicolae, D. N. (2021). Application of airborne and spaceborne hyperspectral imaging techniques for atmospheric research: Past, present, and future. *Applied Spectroscopy Reviews*, 56(4), 289–323.
- Calin, M. A., Parasca, S. V., Savastru, D., & Manea, D. (2014). Hyperspectral imaging in the medical field: Present and future. *Applied Spectroscopy Reviews*, 49(6), 435–447.
- Campbell, P. K. E., Middleton, E. M., McMurtrey, J. E., Corp, L. A., & Chappelle, E. W. (2007). Assessment of Vegetation Stress Using Reflectance or Fluorescence Measurements. *Journal of Environmental Quality*, 36(3), 832–845. <https://doi.org/10.2134/JEQ2005.0396>
- Charles, A. S., Olshausen, B. A., & Rozell, C. J. (2011). Learning Sparse Codes for Hyperspectral Imagery. *IEEE Journal of Selected Topics in Signal Processing*, 5(5), 963–978. <https://doi.org/10.1109/JSTSP.2011.2149497>
- Chatterjee, A. K. (2018). *Cement production technology: Principles and practice*. CRC Press.
- Chein-I Chang. (2003). *Hyperspectral Imaging Techniques for Spectral Detection and Classification*. Springer Science & Business Media.

- Chen, L. J., Xing, L., & Han, L. J. (2010). Influence of Data Preprocessing on the Quantitative Determination of Nutrient Content in Poultry Manure by Near Infrared Spectroscopy. *Journal of Environmental Quality*, 39(5), 1841–1847. <https://doi.org/10.2134/JEQ2009.0449>
- Chen, Y. L., Shih, P. H., Chiang, L. C., Chang, Y. K., Lu, H. C., & Chang, J. E. (2009). The influence of heavy metals on the polymorphs of dicalcium silicate in the belite-rich clinkers produced from electroplating sludge. *Journal of Hazardous Materials*, 170(1), 443–448. <https://doi.org/10.1016/J.JHAZMAT.2009.04.076>
- Clydesdale, G. J., Dandie, G. W., & Muller, H. K. (2001). Ultraviolet light induced injury: immunological and inflammatory effects. *Immunology and Cell Biology*, 79(6), 547–568.
- Cozzolino, D., Williams, P., Journal, L. H.-M., & 2023, undefined. (2023). An overview of pre-processing methods available for hyperspectral imaging applications. *Elsevier*.
- Dai, Q., Sun, D. W., Cheng, J. H., Pu, H., Zeng, X. A., & Xiong, Z. (2014). Recent Advances in De-Noising Methods and Their Applications in Hyperspectral Image Processing for the Food Industry. *Comprehensive Reviews in Food Science and Food Safety*, 13(6), 1207–1218. <https://doi.org/10.1111/1541-4337.12110>
- Dale, L. M., Thewis, A., Boudry, C., Rotar, I., Dardenne, P., Baeten, V., & Pierna, J. A. F. (2013). Hyperspectral imaging applications in agriculture and agro-food product quality and safety control: A review. *Applied Spectroscopy Reviews*, 48(2), 142–159.
- Dawson, T. L. (2005). Beyond the visible: ultraviolet and infrared radiation. *Review of Progress in Coloration and Related Topics*, 35(1), 31–41. <https://doi.org/10.1111/J.1478-4408.2005.TB00158.X>

- De Beule, P. A. A., Dunsby, C., Galletly, N. P., Stamp, G. W., Chu, A. C., Anand, U., Anand, P., Benham, C. D., Naylor, A., & French, P. M. W. (2007). A hyperspectral fluorescence lifetime probe for skin cancer diagnosis. *Review of Scientific Instruments*, 78(12), 123101.
- Diane, A., Saffaj, T., Ihssane, B., Heliyon, R. R., & 2023, undefined. (2023). The synergic approach between machine learning, chemometrics, and NIR hyperspectral imagery for a real-time, reliable, and accurate prediction of mass loss. *Cell.Com*, 9, 15898. <https://doi.org/10.1016/j.heliyon.2023.e15898>
- Double, D. D., Hellawell, A., & Perry, S. J. (1978). Hydration of portland cement. *Proc R Soc London Ser A*, 359(1699), 435–451. <https://doi.org/10.1098/RSPA.1978.0050>
- Edelman, G. J., Gaston, E., Van Leeuwen, T. G., Cullen, P. J., & Aalders, M. C. G. (2012). *Hyperspectral imaging for non-contact analysis of forensic traces*. <https://doi.org/10.1016/j.forsciint.2012.09.012>
- ElMasry, G., Kamruzzaman, M., Sun, D. W., & Allen, P. (2012). Principles and Applications of Hyperspectral Imaging in Quality Evaluation of Agro-Food Products: A Review. *Critical Reviews in Food Science and Nutrition*, 52(11), 999–1023. <https://doi.org/10.1080/10408398.2010.543495>
- Elmasry, G., & Petter Wold, J. (2008). *High-Speed Assessment of Fat and Water Content Distribution in Fish Fillets Using Online Imaging Spectroscopy*. <https://doi.org/10.1021/jf801074s>
- ElMasry, G., & Sun, D.-W. (2010). Principles of hyperspectral imaging technology. In *Hyperspectral imaging for food quality analysis and control* (pp. 3–43). Elsevier.
- Ewald, F., Kölling, T., Baumgartner, A., Zinner, T., & Mayer, B. (2016). Design and characterization of specMACS, a multipurpose hyperspectral cloud and sky imager. *Atmospheric Measurement Techniques*, 9(5), 2015–2042. <https://doi.org/10.5194/AMT-9-2015-2016>

- Fan, L., Fan, M., Alhaj, A., Chen, G., & Ma, H. (2020). Hyperspectral imaging features for mortar classification and compressive strength assessment. *Construction and Building Materials*, 251. <https://doi.org/10.1016/j.conbuildmat.2020.118935>
- Fernández-Carrasco, L., Torrens-Martín, D., Morales, L. M., & Martínez-Ramírez, S. (2012). Infrared Spectroscopy in the Analysis of Building and Construction Materials. *Infrared Spectroscopy - Materials Science, Engineering and Technology*. <https://doi.org/10.5772/36186>
- Fernández-Carrasco, L., & Vázquez, E. (2009). Reactions of fly ash with calcium aluminate cement and calcium sulphate. *Fuel*, 88(9), 1533–1538. <https://doi.org/10.1016/J.FUEL.2009.02.018>
- Fong, A., Simanski, M., & Hsu, M. (2018, August 1). *Hyperspectral Imaging: Hyperspectral microscopy serves biological pathology*.
- Funatomi, T., Ogawa, T., Tanaka, K., Kubo, H., Caron, G., Mouaddib, E. M., Matsushita, Y., & Mukaigawa, Y. (2022). Eliminating temporal illumination variations in whisk-broom hyperspectral imaging. *International Journal of Computer Vision*, 130(5), 1310–1324.
- Gagg, C. R. (2014). Cement and concrete as an engineering material: an historic appraisal and case study analysis. *Engineering Failure Analysis*, 40, 114–140. <https://doi.org/10.1016/J.ENGFAILANAL.2014.02.004>
- Gamez, G., Frey, D., & Michler, J. (2012). Push-broom hyperspectral imaging for elemental mapping with glow discharge optical emission spectrometry. *Journal of Analytical Atomic Spectrometry*, 27(1), 50–55. <https://doi.org/10.1039/C1JA10241A>
- Garini, Y., Young, I., ... G. M.-P. A. T. J. of the, & 2006, undefined. (2006). Spectral imaging: principles and applications. *Wiley Online Library*, 69(8), 735–747. <https://doi.org/10.1002/cyto.a.20311>

- Ghamisi, P., Yokoya, N., Li, J., Liao, W., Liu, S., Plaza, J., Rasti, B., & Plaza, A. (2017). Advances in Hyperspectral Image and Signal Processing: A Comprehensive Overview of the State of the Art. In *IEEE Geoscience and Remote Sensing Magazine* (Vol. 5, Issue 4, pp. 37–78). Institute of Electrical and Electronics Engineers Inc. <https://doi.org/10.1109/MGRS.2017.2762087>
- Ghosh, S. (2014). *Advances in cement technology: critical reviews and case studies on manufacturing, quality control, optimization and use*.
- Ghosh, S., & Pal, S. (2022). MRI, CT, and PETSCAN: Engineer’s Perspective. *Cancer Diagnostics and Therapeutics: Current Trends, Challenges, and Future Perspectives*, 113–143. https://doi.org/10.1007/978-981-16-4752-9_6
- Giardino, M. J. (2012). NASA remote sensing and archaeology. *Remote Sensing and Digital Image Processing*, 16, 157–176. https://doi.org/10.1007/978-90-481-8801-7_7
- Gismera-Diez, S., B Manchobas-Pantoja, Carmona-Quiroga, P. M. , & Blanco-Varela, M. T. (2015). Effect of BaCO₃ on C3A hydration. *Cement and Concrete Research*, 73, 70–75.
- Goetz, A. F. H. (2009). Three decades of hyperspectral remote sensing of the Earth: A personal view. *Remote Sensing of Environment*, 113(SUPPL. 1), S5–S16. <https://doi.org/10.1016/J.RSE.2007.12.014>
- Gowen, A. A., O’Donnell, C. P., Cullen, P. J., Downey, G., & Frias, J. M. (2007). Hyperspectral imaging - an emerging process analytical tool for food quality and safety control. *Trends in Food Science and Technology*, 18(12), 590–598. <https://doi.org/10.1016/j.tifs.2007.06.001>
- Grounds, T., Midgley, H., & Acta, D. N. (1988). Carbonation of ettringite by atmospheric carbon dioxide. *Thermochimica Acta*.
- Gu, Y., Wang, C., & Li, X. (2022). An Intensity-Independent Stereo Registration Method of Push-Broom Hyperspectral Scanner and LiDAR on UAV

Platforms. *IEEE Transactions on Geoscience and Remote Sensing*, 60.

<https://doi.org/10.1109/TGRS.2022.3211202>

Gutiérrez-Gutiérrez, J. A., Pardo, A., Real, E., López-Higuera, J. M., & Conde, O. M. (2019). Custom scanning hyperspectral imaging system for biomedical applications: modeling, benchmarking, and specifications. *Sensors*, 19(7), 1692.

Hagen, N., & Kudenov, M. W. (2013). Review of snapshot spectral imaging technologies. *Optical Engineering*, 52(9), 090901.

<https://doi.org/10.1117/1.oe.52.9.090901>

Halstead, P. E. (1961). The Early History of Portland Cement. *Transactions of the Newcomen Society*, 34(1), 37–54. <https://doi.org/10.1179/TNS.1961.003>

Hartel, R. W., McCarthy, M., Peleg, M., Rahman, S., University, Q., & Rao, O. M. A. (2015). *Hyperspectral imaging technology in food and agriculture*.

Herfort, D., & Macphee, DE. (2019). 3-Components in Portland cement clinker and their phase relationships. *Lea's Chemistry of Cement and Concrete*.

Higl, J., Hinder, D., Rathgeber, C., Ramming, B., & Lindén, M. (2021). Detailed in situ ATR-FTIR spectroscopy study of the early stages of C-S-H formation during hydration of monoclinic C3S. *Cement and Concrete Research*, 142, 106367. <https://doi.org/10.1016/J.CEMCONRES.2021.106367>

Hill, M. A. (2004). The variation in biological effectiveness of X-rays and gamma rays with energy. *Radiation Protection Dosimetry*, 112(4), 471–481.

<https://doi.org/10.1093/RPD/NCH091>

Jia, X. (2010). Effect of CaCO₃ on hydration characteristics of C 3 A. *J. Cent. South Univ. Technol*, 17, 918–923.

<https://doi.org/10.1007/s11771-010-0577-2>

- Joseph, S., Skibsted, J., & Cizer, Ö. (2019). A quantitative study of the C3A hydration. *Cement and Concrete Research*, *115*, 145–159.
<https://doi.org/10.1016/j.cemconres.2018.10.017>
- Jun, S. , Krishnamurthy, K. , Irudayaraj, J. , Demirci, A. , Pan, Z. , & Atungulu, G. G. (2010). Fundamentals and theory of infrared radiation. *Infrared Heating for Food and Agricultural Processing*.
- Jurado, J. M., Padua, L., Hruska, J., Feito, F. R., & Sousa, J. J. (2021). An Efficient Method for Generating UAV-Based Hyperspectral Mosaics Using Push-Broom Sensors. *IEEE Journal of Selected Topics in Applied Earth Observations and Remote Sensing*, *14*, 6515–6531.
<https://doi.org/10.1109/JSTARS.2021.3088945>
- Kakali, G., Tsivilis, S., Aggeli, E., & Bati, M. (2000). Hydration products of C3A, C3S and Portland cement in the presence of CaCO₃. *Cement and Concrete Research*, *30*(7), 1073–1077. [https://doi.org/10.1016/S0008-8846\(00\)00292-1](https://doi.org/10.1016/S0008-8846(00)00292-1)
- Khan, M. J., Khan, H. S., Yousaf, A., Khurshid, K., & Abbas, A. (2018). Modern Trends in Hyperspectral Image Analysis: A Review. In *IEEE Access* (Vol. 6, pp. 14118–14129). Institute of Electrical and Electronics Engineers Inc.
<https://doi.org/10.1109/ACCESS.2018.2812999>
- Khosla, R. P. (1992). From Photons to Bits. *Physics Today*, *45*(12), 42–49.
<https://doi.org/10.1063/1.881326>
- Kim, M. S., Chen, Y. R., & Mehl, P. M. (2001). Hyperspectral reflectance and fluorescence imaging system for food quality and safety. *Transactions of the American Society of Agricultural Engineers*, *44*(3), 721–729.
<https://doi.org/10.13031/2013.6099>
- Klein, M. E., Aalderink, B. J., Padoan, R., De Bruin, G., & Steemers, T. A. G. (2008). Quantitative Hyperspectral Reflectance Imaging. *Italian National Conference on Sensors*, *8*(9), 5576–5618. <https://doi.org/10.3390/S8095576>

- Koonen, T. (2006). Fabry-Perot Interferometer Filters. In H. Venghaus (Ed.), *Wavelength Filters in Fibre Optics* (pp. 271–287). Springer Berlin Heidelberg. https://doi.org/10.1007/3-540-31770-8_7
- Krupnik, D., & Khan, S. (2019). Close-range, ground-based hyperspectral imaging for mining applications at various scales: Review and case studies. *Earth-Science Reviews*, 198, 102952.
- Kumar Mehta, P., & M Monteiro, P. J. (2014). *Concrete: microstructure, properties, and materials*. McGraw-Hill Education.
- Li, Q., He, X., Wang, Y., Liu, H., Xu, D., & Guo, F. (2013). Review of spectral imaging technology in biomedical engineering: achievements and challenges. *Journal of Biomedical Optics*, 18(10), 100901. <https://doi.org/10.1117/1.jbo.18.10.100901>
- Li, X., Li, R., Wang, M., Liu, Y., Zhang, B., & Zhou, J. (2018). *Hyperspectral Imaging and Their Applications in the Nondestructive Quality Assessment of Fruits and Vegetables*. <https://doi.org/10.5772/intechopen.72250>
- Li, X., Ouzia, A., & Scrivener, K. (2018). Laboratory synthesis of C3S on the kilogram scale. *Cement and Concrete Research*, 108, 201–207. <https://doi.org/10.1016/j.cemconres.2018.03.019>
- Li, Z., Zhou, X., Ma, H., & Hou, D. (2022). *Advanced concrete technology*.
- Liu, X., Zhou, M., Qiu, S., -, al, Li, Q., Wang, Y., Ma, X., Ebner, M., & Nabavi, E. (2009). Snapshot hyperspectral imaging and practical applications. *Journal of Physics: Conference Series*, 178(1), 012048. <https://doi.org/10.1088/1742-6596/178/1/012048>
- Liu, Y., Pu, H., & Sun, D. W. (2017). Hyperspectral imaging technique for evaluating food quality and safety during various processes: A review of recent applications. In *Trends in Food Science and Technology* (Vol. 69, pp. 25–35). Elsevier Ltd. <https://doi.org/10.1016/j.tifs.2017.08.013>

- Lodhi, V., Chakravarty, D., & Mitra, P. (2019). Hyperspectral Imaging System: Development Aspects and Recent Trends. *Sensing and Imaging*, 20(1). <https://doi.org/10.1007/s11220-019-0257-8>
- Lu, B., Dao, P. D., Liu, J., He, Y., & Shang, J. (2020). Recent advances of hyperspectral imaging technology and applications in agriculture. *Remote Sensing*, 12(16), 2659.
- Lu, G., & Fei, B. (2014). Medical hyperspectral imaging: a review. *Journal of Biomedical Optics*, 19(1), 10901.
- Lu, R., & Chen, Y.-R. (1999). Hyperspectral imaging for safety inspection of food and agricultural products. *In Pathogen Detection and Remediation for Safe Eating*, 3544(12), 121–133. <https://doi.org/10.1117/12.335771>
- Lü, Y., Li, X., Ma, B., & De Schutter, G. (2016). Polymorph transformation of tricalcium silicate doped with heavy metal. *Journal Wuhan University of Technology, Materials Science Edition*, 31(4), 883–890. <https://doi.org/10.1007/s11595-016-1463-z>
- Lu, Y., Saeys, W., Kim, M., Peng, Y., & Lu, R. (2020). Hyperspectral imaging technology for quality and safety evaluation of horticultural products: A review and celebration of the past 20-year progress. *Postharvest Biology and Technology*, 170(111318).
- Luyypaert, Heuerding, S. , Vander Heyden, Y. , & Massart, D. L. (2004). The effect of preprocessing methods in reducing interfering variability from near-infrared measurements of creams. *Journal of Pharmaceutical and Biomedical Analysis*, 36(3), 495–503. <https://doi.org/10.1016/j.jpba.2004.06.023>
- Ma, J., Sun, D. W., Pu, H., Cheng, J. H., & Wei, Q. (2019). Advanced Techniques for Hyperspectral Imaging in the Food Industry: Principles and Recent Applications. *Annual Review of Food Science and Technology*, 10, 197–220. <https://doi.org/10.1146/ANNUREV-FOOD-032818-121155>

- Maheswaran, S., Kalaiselvam, S., Arunbalaji, S., Palani, G. S., & Iyer, N. R. (2015). Low-temperature preparation of belite from lime sludge and nanosilica through solid-state reaction. *Journal of Thermal Analysis and Calorimetry*, *119*(3), 1845–1852. <https://doi.org/10.1007/s10973-014-4371-5>
- Maheswaran, S., Kalaiselvam, S., Saravana Karthikeyan, S. K. S., Kokila, C., & Palani, G. S. (2016). β -Belite cements (β -dicalcium silicate) obtained from calcined lime sludge and silica fume. *Cement and Concrete Composites*, *66*, 57–65. <https://doi.org/10.1016/J.CEMCONCOMP.2015.11.008>
- Maleki, M. R., Mouazen, A. M., Ramon, H., & De Baerdemaeker, J. (2007). Multiplicative scatter correction during on-line measurement with near infrared spectroscopy. *Biosystems Engineering*, *96*(3), 427–433.
- Mandal, S. M., & Paul, D. (2022). Spectroscopy: Principle, Types and Microbiological Applications. *Automation and Basic Techniques in Medical Microbiology*, 49–75. https://doi.org/10.1007/978-1-0716-2372-5_5
- Manley, M. (2014a). Near-infrared spectroscopy and hyperspectral imaging: non-destructive analysis of biological materials. *Chem. Soc. Rev*, *8200*, 8200. <https://doi.org/10.1039/c4cs00062e>
- Manley, M. (2014b). Near-infrared spectroscopy and hyperspectral imaging: Non-destructive analysis of biological materials. *Chemical Society Reviews*, *43*(24), 8200–8214. <https://doi.org/10.1039/C4CS00062E>
- Manolakis, D., & Shaw, G. (2002). Detection algorithms for hyperspectral imaging applications. *IEEE Signal Processing Magazine*, *19*(1), 29–43. <https://doi.org/10.1109/79.974724>
- Martin, M. E., Wabuyele, M. B., Chen, K., Kasili, P., Panjehpour, M., Phan, M., Overholt, B., Cunningham, G., Wilson, D., & DeNovo, R. C. (2006). Development of an advanced hyperspectral imaging (HSI) system with applications for cancer detection. *Annals of Biomedical Engineering*, *34*, 1061–1068.

- Mateen, M., Wen, J., & Azeem Akbar, M. (2018). The Role of Hyperspectral Imaging: A Literature Review. *IJACSA) International Journal of Advanced Computer Science and Applications*, 9(8).
- Milne, J. S., Dell, J. M., Keating, A. J., & Faraone, L. (2009). Widely tunable MEMS-based Fabry–Perot filter. *Journal of Microelectromechanical Systems*, 18(4), 905–913.
- Mindess, S., Young, F. J., & Darwin, D. (2003). Concrete 2nd editio. *Technical Documents*, 644.
- Mirabella, F. (1998). *Modern techniques in applied molecular spectroscopy* (Vol. 14). John Wiley & Sons.
- Mollah, Yu, W. , Schennach, R. , & Cocke, D. L. (2000). A Fourier transform infrared spectroscopic investigation of the early hydration of Portland cement and the influence of sodium lignosulfonate. *Cement and Concrete Research*, 30(2), 267–273.
- Munera, S., Blasco, J., Amigo, J. M. , Cubero, S. , Talens, P. , & Aleixos, N. (2019). Use of hyperspectral transmittance imaging to evaluate the internal quality of nectarines. *Biosystems Engineering*, 182, 54–64.
- Nakamura, J. (2017). *Image sensors and signal processing for digital still cameras*. CRC press.
- Nasrabadi, N. M. (2014). Hyperspectral target detection : An overview of current and future challenges. *IEEE Signal Processing Magazine*, 31(1), 34–44.
<https://doi.org/10.1109/MSP.2013.2278992>
- Neville, A., & Brooks, J. (1987). *Concrete technology* (Vol. 438). England: Longman Scientific & Technical.
- Choo, B. S., & Newman, J. (2003). *Advanced concrete technology : constituent materials*. Elsevier Ltd.

- Nicolai, B. M., Beullens, K., Bobelyn, E., Peirs, A., Saeys, W., Theron, K. I., & Lammertyn, J. (2007). Nondestructive measurement of fruit and vegetable quality by means of NIR spectroscopy: A review. *Postharvest Biology and Technology*, *46*(2), 99–118.
<https://doi.org/10.1016/J.POSTHARVBIO.2007.06.024>
- Omotosoa, O. E., Ivey, D. G., & Mikulab, R. (1995). Characterization of chromium doped tricalcium silicate using SEM/EDS, XRD and FTIR. In *Journal of Hazardous Materials* (Vol. 42).
- Ortaç, G., Bilgi, A., Taşdemir, K., & Kalkan, H. (2016). A hyperspectral imaging based control system for quality assessment of dried figs. *Computers and Electronics in Agriculture*, *130*, 38–47.
- Ortega, S., Guerra, R., Diaz, M., Fabelo, H., Lopez, S., Callico, G. M., & Sarmiento, R. (2019). Hyperspectral Push-Broom Microscope Development and Characterization. *IEEE Access*, *7*, 122473–122491.
<https://doi.org/10.1109/ACCESS.2019.2937729>
- Osepchuk, J. M. (1984). A history of microwave heating applications. *IEEE Transactions on Microwave Theory and Techniques*, *32*(9), 1200–1224.
- Padoan, R., Steemers, T. A. G., Klein, M. E., Aalderink, B. J., & De Bruin, G. (2008). *Quantitative hyperspectral imaging of historical documents: Technique and applications*.
- Panasyuk, S. V, Yang, S., Faller, D. V, Ngo, D., Lew, R. A., Freeman, J. E., & Rogers, A. E. (2007). Medical hyperspectral imaging to facilitate residual tumor identification during surgery. *Cancer Biology & Therapy*, *6*(3), 439–446.
- Pavia, D. L., Lampman, G. M., Kriz, G. S., & Vyvyan, J. A. (2008). *Introduction to Spectroscopy*. Cengage Learning.

- Peiris, K. H. S., Dull, G. G., Leffler, R. G., & Kays, S. J. (1999). Spatial Variability of Soluble Solids or Dry-matter Content within Individual Fruits, Bulbs, or Tubers: Implications for the Development and Use of NIR Spectrometric Techniques. *HortScience HortSci*, 34(1), 114–118.
<https://doi.org/10.21273/HORTSCI.34.1.114>
- Penner, M. H. (2017). *Ultraviolet, Visible, and Fluorescence Spectroscopy*. 89–106. https://doi.org/10.1007/978-3-319-45776-5_7
- Ping, Y., Kirkpatrick, R. J., Brent, P., McMillan, P. F., & Cong, X. (1999). Structure of calcium silicate hydrate (C-S-H): Near-, mid-, and far-infrared spectroscopy. *Journal of the American Ceramic Society*, 82(3), 742–748.
<https://doi.org/10.1111/J.1151-2916.1999.TB01826.X>
- Pitak, L., Sirisomboon, P., Saengprachatanarug, K., Wongpichet, S., & Posom, J. (2021). Rapid elemental composition measurement of commercial pellets using line-scan hyperspectral imaging analysis. *Energy*, 220, 119698.
<https://doi.org/10.1016/J.ENERGY.2020.119698>
- Pizarro, C., Esteban-Díez, I., Nistal, A. J., & González-Sáiz, J. M. (2004). Influence of data pre-processing on the quantitative determination of the ash content and lipids in roasted coffee by near infrared spectroscopy. *Analytica Chimica Acta*, 509(2), 217–227. <https://doi.org/10.1016/j.aca.2003.11.008>
- Pourchet, S., Regnaud, L., Perez, J. P., & Nonat, A. (2009). Early C3A hydration in the presence of different kinds of calcium sulfate. *Cement and Concrete Research*, 39(11), 989–996.
<https://doi.org/10.1016/J.CEMCONRES.2009.07.019>
- Qin, J. (2010). Hyperspectral Imaging Instruments. *Hyperspectral Imaging for Food Quality Analysis and Control*, 129–172. <https://doi.org/10.1016/B978-0-12-374753-2.10005-X>

- Qin, J., Kim, M. S., Chao, K., Chan, D. E., Delwiche, S. R., & Cho, B.-K. (2017). *Line-Scan Hyperspectral Imaging Techniques for Food Safety and Quality Applications*. <https://doi.org/10.3390/app7020125>
- Quennoz, A. (2011). *Hydration of C3A with calcium sulfate alone and in the presence of calcium silicate*. EPFL.
- Quennoz, A., & Scrivener, K. L. (2012). Hydration of C 3A-gypsum systems. *Cement and Concrete Research*, 42(7), 1032–1041. <https://doi.org/10.1016/j.cemconres.2012.04.005>
- Ramer, G., Aksyuk, V. A., Centrone, A., & Nanocenter, M. (2017). *Quantitative Chemical Analysis at the Nanoscale Using the Photothermal Induced Resonance Technique*. <https://doi.org/10.1021/acs.analchem.7b03878>
- Rasti, B., Hong, D., Hang, R., Ghamisi, P., Kang, X., Chanussot, J., & Benediktsson, J. A. (2020). Feature extraction for hyperspectral imagery: The evolution from shallow to deep: Overview and toolbox. *IEEE Geoscience and Remote Sensing Magazine*, 8(4), 60–88.
- Rheinheimer, V., Chae, S. R., Rodríguez, E. D., Geng, G., Kirchheim, A. P., & Monteiro, P. J. M. (2016). *materials A Scanning Transmission X-ray Microscopy Study of Cubic and Orthorhombic C 3 A and Their Hydration Products in the Presence of Gypsum*. <https://doi.org/10.3390/ma9090745>
- Rinnan, Å., Berg, F. van den, & Engelsen, S. B. (2009). Review of the most common pre-processing techniques for near-infrared spectra. In *TrAC - Trends in Analytical Chemistry* (Vol. 28, Issue 10, pp. 1201–1222). <https://doi.org/10.1016/j.trac.2009.07.007>
- Rodrigues, F. A. (2003a). Synthesis of chemically and structurally modified dicalcium silicate. *Cement and Concrete Research*, 33(6), 823–827. [https://doi.org/10.1016/S0008-8846\(02\)01065-7](https://doi.org/10.1016/S0008-8846(02)01065-7)

- Rodrigues, F. A. (2003b). Synthesis of chemically and structurally modified dicalcium silicate. *Cement and Concrete Research*, 33(6), 823–827.
- Ruffin, C., King, R., Sensing, N. Y.-Gis. & R., & 2008, undefined. (2013). A combined derivative spectroscopy and Savitzky-Golay filtering method for the analysis of hyperspectral data. *Taylor & Francis*, 45(1), 1–15.
<https://doi.org/10.2747/1548-1603.45.1.1>
- Sáez Del Bosque, I. F., Martínez-Ramírez, S., & Blanco-Varela, M. T. (2014). FTIR study of the effect of temperature and nanosilica on the nano structure of C-S-H gel formed by hydrating tricalcium silicate. *Construction and Building Materials*, 52, 314–323. <https://doi.org/10.1016/j.conbuildmat.2013.10.056>
- Saikia, N., Kato, S., & Kojima, T. (2012). Influence of Sn on the hydration of tricalcium aluminate, Ca₃Al₂O₆. *Journal of Thermal Analysis and Calorimetry*, 109(1), 273–286. <https://doi.org/10.1007/s10973-011-1750-z>
- Schaare, P. N., & Fraser, D. G. (2000). Comparison of reflectance, interactance and transmission modes of visible-near infrared spectroscopy for measuring internal properties of kiwifruit (*Actinidia chinensis*). *Postharvest Biology and Technology*, 20(2), 175–184. [https://doi.org/10.1016/S0925-5214\(00\)00130-7](https://doi.org/10.1016/S0925-5214(00)00130-7)
- Scrivener, K., Ouzia, A., Juilland, P., & Mohamed, A. K. (2019). Advances in understanding cement hydration mechanisms. *Cement and Concrete*.
- Selci, S. (2019). The Future of Hyperspectral Imaging. *The Future of Hyperspectral Imaging*, 220. <https://doi.org/10.3390/BOOKS978-3-03921-823-3>
- Sharma, B. K. (1981). *Instrumental methods of chemical analysis*. Krishna Prakashan Media.
- Shetty, M., & Jain, A. (2019). *Concrete Technology (Theory and Practice)*,. Chand Publishing.

- Shippert, P. (2021). Introduction to Hyperspectral Image Analysis. *Online Journal of Space Communication*, 2(3).
- Sikdar, D., & Kornyshev, A. A. (2019). An electro-tunable Fabry–Perot interferometer based on dual mirror-on-mirror nanoplasmonic metamaterials. *Nanophotonics*, 8(12), 2279–2290.
- Singh, N. B. (2006). Hydrothermal synthesis of β -dicalcium silicate (β -Ca₂SiO₄). *Progress in Crystal Growth and Characterization of Materials*, 52(1–2), 77–83.
- Solanki, A., Singh, L. P., Karade, S. R., & Sharma, U. (2021). Functionality of silica nanoparticles on hydration mechanism and microstructure of tricalcium aluminate. *Construction and Building Materials*, 299, 124238.
<https://doi.org/10.1016/J.CONBUILDMAT.2021.124238>
- Song, M., Li, F., Yu, C., & Chang, C. (2021). Sequential band fusion for hyperspectral anomaly detection. *IEEE Transactions on Geoscience and Remote Sensing*, 60, 1–16.
- Sonobe, R., Yamashita, H., Mihara, H., Morita, A., & Ikka, T. (2020). Hyperspectral reflectance sensing for quantifying leaf chlorophyll content in wasabi leaves using spectral pre-processing techniques and machine learning algorithms. *Taylor & Francis*, 42(4), 1311–1329.
<https://doi.org/10.1080/01431161.2020.1826065>
- Stuart, M. B., McGonigle, A. J. S., & Willmott, J. R. (2019). Hyperspectral imaging in environmental monitoring: A review of recent developments and technological advances in compact field deployable systems. *Sensors*, 19(14), 3071.
- Stuart, M., McGonigle, A., & Willmott, J. (2019). Hyperspectral imaging in environmental monitoring: A review of recent developments and technological advances in compact field deployable systems. *Sensors*, 22(5).
<https://doi.org/10.3390/s19143071>

- Sun, D. W. (2010). Hyperspectral Imaging for Food Quality Analysis and Control. *Hyperspectral Imaging for Food Quality Analysis and Control*.
<https://doi.org/10.1016/C2009-0-01853-4>
- Sun, J., Yang, W., Zhang, M., Feng, M., & Xiao, L. (2021). Estimation of water content in corn leaves using hyperspectral data based on fractional order Savitzky-Golay derivation coupled with wavelength selection. *Computers and Electronics in Agriculture*, 182(105989).
- Szantoi, Z. (2013). *Review of the use of remotely-sensed data for monitoring biodiversity change and tracking progress towards the aichi biodiversity targets*.
- Tan, S.-Y. (2016). Developments in Hyperspectral Sensing. In *Handbook of Satellite Applications* (pp. 1–21). Springer New York.
https://doi.org/10.1007/978-1-4614-6423-5_101-1
- Tarrant, J. (2003). *Digital camera techniques*. Routledge.
- Tatsuno, K. (2006). Current trends in digital cameras and camera-phones. *NISTEP Science & Technology Foresight Center*.
- Taylor, H. F. W. (1963). The chemistry of cement hydration. *Progress in Ceramic Science*, 1, 89–145.
- Taylor, H. F. W. (1997). *Cement chemistry 2nd edition* (Vol. 2). London: Thomas Telford.
- Thomas, N. C. (1991). The early history of spectroscopy. *Journal of Chemical Education*, 68(8), 631–634. <https://doi.org/10.1021/ED068P631>
- Tian, Y., Pan, X., Yu, H., & Tu, G. (2016). Formation mechanism of calcium aluminate compounds based on high-temperature solid-state reaction. *Journal of Alloys and Compounds*, 670, 96–104.

- Tokyay, M. (2016). Cement and concrete mineral admixtures. In *Cement and Concrete Mineral Admixtures*. CRC Press.
<https://doi.org/10.1201/B20093/CEMENT-CONCRETE-MINERAL-ADMIXTURES-MUSTAFA-TOKYAY>
- Trezza, M. A., & Lavat, A. E. (2001). Analysis of the system $3\text{CaO}\cdot\text{Al}_2\text{O}_3\text{-CaSO}_4\cdot 2\text{H}_2\text{O}\text{-CaCO}_3\text{-H}_2\text{O}$ by FT-IR spectroscopy. *Cement and Concrete Research*, *31*(6), 869–872. [https://doi.org/10.1016/S0008-8846\(01\)00502-6](https://doi.org/10.1016/S0008-8846(01)00502-6)
- Tripathi, M. K., & Govil, H. (2019). Evaluation of AVIRIS-NG hyperspectral images for mineral identification and mapping. *Heliyon*, *5*(11), e02931.
- Trussell, H. J., & Vrhel, M. J. (2008). *Fundamentals of digital imaging*. Cambridge University Press.
- Tsai, F., environment, W. P.-R. sensing of, & 1998, undefined. (1998). Derivative analysis of hyperspectral data. *Elsevier*.
- Vidal, M., & Amigo, J. M. (2012). Pre-processing of hyperspectral images. Essential steps before image analysis. *Chemometrics and Intelligent Laboratory Systems*, *117*, 138–148.
<https://doi.org/10.1016/j.chemolab.2012.05.009>
- Wadoux, A. M. J.-C., Malone, B., Minasny, B., Fajardo, M., & McBratney, A. B. (2021). Pre-processing of Spectra. In A. M. J.-C. Wadoux, B. Malone, B. Minasny, M. Fajardo, & A. B. McBratney (Eds.), *Soil Spectral Inference with R: Analysing Digital Soil Spectra using the R Programming Environment* (pp. 49–79). Springer International Publishing. https://doi.org/10.1007/978-3-030-64896-1_5
- Wang, B., Sun, J., Xia, L., Liu, J., Wang, Z., Li, P., Guo, Y., & Sun, X. (2021). The Applications of Hyperspectral Imaging Technology for Agricultural Products Quality Analysis: A Review. *Food Reviews International*.
<https://doi.org/10.1080/87559129.2021.1929297>

- Wang, Y. W., Reder, N. P., Kang, S., Glaser, A. K., & Liu, J. T. C. (2017). Multiplexed optical imaging of tumor-directed nanoparticles: A review of imaging systems and approaches. *Nanotheranostics*, *1*(4), 369–388. <https://doi.org/10.7150/NTNO.21136>
- Wesselsky, A., & Jensen, O. M. (2009). Synthesis of pure Portland cement phases. *Cement and Concrete Research*, *39*(11), 973–980. <https://doi.org/10.1016/j.cemconres.2009.07.013>
- Windig, W., Shaver, J., & Bro, R. (2008). Loopy MSC: a simple way to improve multiplicative scatter correction. *Applied Spectroscopy*, *62*(10), 1153–1159.
- Witteveen, M., Sterenborg, H. J. C. M., Van Leeuwen, T. G., Aalders, M. C. G., Ruers, T. J. M., & Post, A. L. (2022). Comparison of preprocessing techniques to reduce nontissue-related variations in hyperspectral reflectance imaging. *Spiedigitallibrary.Org*, *27*(10). <https://doi.org/10.1117/1.JBO.27.10.106003>
- Wolbarst, A. (1999). *Looking within: how X-ray, CT, MRI, ultrasound, and other medical images are created, and how they help physicians save lives*. Univ of California Press.
- Wold, S., Antti, H., Lindgren, F., Ohman, J., & Sweden°, S. (1998). Orthogonal signal correction of near-infrared spectra. In *Chemometrics and Intelligent Laboratory Systems* (Vol. 44).
- Wu, D., & Sun, D. W. (2013a). Advanced applications of hyperspectral imaging technology for food quality and safety analysis and assessment: A review - Part I: Fundamentals. *Innovative Food Science and Emerging Technologies*, *19*, 1–14. <https://doi.org/10.1016/J.IFSET.2013.04.014>
- Wu, D., & Sun, D. W. (2013b). Advanced applications of hyperspectral imaging technology for food quality and safety analysis and assessment: A review - Part II: Applications. *Innovative Food Science and Emerging Technologies*, *19*, 15–28. <https://doi.org/10.1016/J.IFSET.2013.04.016>

- Xing, H., Feng, H., Fu, J., Xu, X., & Yang, G. (2019). Development and application of hyperspectral remote sensing. *Computer and Computing Technologies in Agriculture XI: 11th IFIP WG 5.14 International Conference, CCTA 2017, Jilin, China, August 12-15, 2017, Proceedings, Part II 11*, 271–282.
- Xu, X., Chen, S., Xu, Z., Yu, Y., Zhang, S., & Sensing, R. (2020). Exploring appropriate preprocessing techniques for hyperspectral soil organic matter content estimation in black soil area. *Remote Sensing*, *12*(22)(3765). <https://doi.org/10.3390/rs12223765>
- Yao, H., & D Lewis. (2010). Spectral preprocessing and calibration techniques. *Hyperspectral Imaging for Food Quality Analysis*, 45–78.
- Yoon, J. (2022). Hyperspectral Imaging for Clinical Applications. *Biochip Journal*, *16*(1). <https://doi.org/10.1007/S13206-021-00041-0>
- Yuen, P. W. T., & Richardson, M. (2010). An introduction to hyperspectral imaging and its application for security, surveillance and target acquisition. *Imaging Science Journal*, *58*(5), 241–253. <https://doi.org/10.1179/174313110X12771950995716>
- Zahiri, Z., Laefer, D., & Gowen, A. (2018). The feasibility of short-wave infrared spectrometry in assessing water-to-cement ratio and density of hardened concrete. *Construction and Building Materials*, *185*, 661–687.
- Zamanian, A., & Hardiman, C. (2005). Electromagnetic radiation and human health: A review of sources and effects. *High Frequency Electronics*, *4*(3), 16–26.
- Zhang, D., & Zhang F. (2014). Application of fractional differential in preprocessing hyperspectral data of saline soil. *Transactions of the Chinese Society of Agricultural Engineering*, *30*(24), 151–160. <https://doi.org/10.3969/j.issn.1002-6819.2014.24.018>

- Zhang, H., Hou, Q., Luo, B., Tu, K., Zhao, C., & Sun, Q. (2022). Detection of seed purity of hybrid wheat using reflectance and transmittance hyperspectral imaging technology. *Frontiers in Plant Science, 13*.
<https://doi.org/10.3389/FPLS.2022.1015891/FULL>
- Zhao, M. (2012). Quantitative control of C2S crystal transformation. *Applied Mechanics and Materials, 121*, 311–315.
- Zhong, Y., Wang, X., Xu, Y., Wang, S., Jia, T., Hu, X., Zhao, J., Wei, L., & Zhang, L. (2018). Mini-UAV-borne hyperspectral remote sensing: From observation and processing to applications. *IEEE Geoscience and Remote Sensing Magazine, 6*(4), 46–62.

CURRICULUM VITAE (ONLY FOR DOCTORAL THESIS)

Surname, Name: Shakouri, Sahra

EDUCATION

Degree	Institution	Year of Graduation
MS	METU Civil Engineering	2017
BS	Tabriz University Civil Engineering	2015
High School	Farzanegan, Ankara	2010

FOREIGN LANGUAGES

Advanced English, Fluent Turkish, Persian and Azerbaijani

PUBLICATIONS

1. Shakouri, S., Bayer, Ö., & Erdoğan, S. T. (2020). Development of silica fume-based geopolymer foams. *Construction and Building Materials*, 260, 120442.
2. Canbek, O., Shakouri, S., & Erdoğan, S. T. (2020). Laboratory production of calcium sulfoaluminate cements with high industrial waste content. *Cement and Concrete Composites*, 106, 103475.